Systematic Studies of Low- and Intermediate-p_T Correlated Angular Distributions in Au+Au Collisions at $\sqrt{s_{NN}} = 200$ GeV from the STAR Experiment

Mark J. Horner

Thesis presented for the Degree of

DOCTOR OF PHILOSOPHY

in the Department of Physics
Faculty of Science
UNIVERSITY OF CAPE TOWN

· February 2007 ·

Abstract

In ultra-relativistic nucleus-nucleus collisions, partons in the nucleons of the incoming nuclei can undergo hard scatterings, resulting in azimuthally correlated partons with high transverse momentum. These partons traverse the hot and dense medium created in the collision, losing energy as they interact. Once they emerge from the medium, with reduced energy, they fragment. Measurements of correlated azimuthal angular di-hadron distributions allow the remnants of jets from the fragmentation of hard scattered partons to be studied. The medium responds to the deposited energy and and this response can also be studied using di-hadron distributions. We present a systematic study of low- and intermediate-p$_T$ correlated angular di-hadron distributions in Au+Au collisions at $\sqrt{s_{NN}} = 200$ GeV from the STAR experiment at RHIC.

We show that there is a significant centrality dependent modification, relative to a d+Au reference, with increased yield on the near- and away-sides. We show that the excess yield at low p_T on the near-side extends to larger $\Delta\eta$ than expected from jet fragmentation, confirming what is seen at higher p_T. In treating this excess yield as a constant ridge we show that the remaining yield is indeed very similar to that observed in d+Au collisions, suggesting a scenario in which a parton loses energy, which forms the ridge, before fragmenting in vacuum.

We systematically study the evolution of the shape of the away-side. We find that it becomes dipped at $\Delta\phi = \pi$. This effect is localised in the space of ($p_T^{assoc.} \times p_T^{trig.}$) with it being most significant at lowest $p_T^{trig.}$ and intermediate $p_T^{assoc.}$. In a phenomenological multi-component decomposition of the away-side shape we find that the location of the peaks is inconsistent with a simple Čerenkov picture but is consistent with a prediction from linearised hydrodynamics.

The suppression of particles at $\Delta\phi = \pi$ is reflected in the measurements of $\langle p_T \rangle$; in the case of raw azimuthal $\langle p_T \rangle$ we see a clear trigger hierarchy on the near-side with the away-side dominated by the bulk. The correlated $\langle p_T \rangle$ shows that the centrality dependence is more prominent for softer $p_T^{trig.}$ and that the dipped away-side shape manifests itself in increased $\langle p_T \rangle$ away from $\Delta\phi = \pi$.

The results presented in this thesis have been presented in:

Papers

Systematic studies of low- and intermediate-pT di-hadron correlations in 200 GeV Au+Au collisions measured at STAR
By STAR Collaboration (J. Adams et al.)
In preparation.

Low- and intermediate-p_T di-hadron distributions in Au+Au collisions at $\sqrt{s_{NN}}$ = 200 GeV from STAR
Mark J. Horner (for the STAR Collaboration) submitted for Proceedings of Quark Matter 2006, Shanghai, China

Azimuthal di-hadron correlations in Au+Au collisions at $\sqrt{s_{NN}}$ = 200 GeV from STAR
Mark J. Horner (for the STAR Collaboration)
AIP Conf. Proc. **842**:125-127,2006

Talks

Low- and intermediate-p_T azimuthal di-hadron correlations from $\sqrt{s_{NN}}$ = 200 GeV Au+Au collisions measured in STAR
Mark J. Horner (for the STAR Collaboration)
Parallel Talk, Quark Matter 2006, Shanghai, China

Angular Particle Correlations from STAR
Mark J. Horner
Heavy-Ion Tea, 2006, Lawrence Berkeley National Laboratory, CA, USA

Intermediate p_T Di-hadron Correlations in 200 GeV Au+Au Collisions
Mark J. Horner (for the STAR Collaboration)
Parallel Talk, PANIC 2005, Sante Fe, NM, USA

Identified Particle Correlations from STAR
Mark J. Horner (for the STAR Collaboration)
Parallel Talk, RHIC/AGS Users Meeting 2005, Brookhaven National Laboratory, NY, USA

Azimuthal Di-hadron Correlations at STAR
Mark J. Horner (for the STAR Collaboration)
Parallel Talk, APS Meeting 2005, Tampa, FL, USA

Posters

Study of Azimuthal Dependence of Low-p_T $h^{+/-}$ Correlated with High-p_T $h^{+/-}$ from STAR
Mark J. Horner (for the STAR Collaboration)
Hard Probes 2006, Asilomar, CA, USA

Study of Azimuthal Dependence of Low-p_T $h^{+/-}$ Correlated with High-p_T $h^{+/-}$ from STAR

Mark J. Horner (for the STAR Collaboration)

Quark Matter 2005, Budapest, Hungary

Not all who wander are lost. . . .

J. R. R. Tolkien

Contents

Chapter 1

Introduction

> *Remember what Bilbo used to say: It's a dangerous business, Frodo, going out your door. You step onto the road, and if you don't keep your feet, there's no knowing where you might be swept off to.*
>
> J. R. R. Tolkien

This thesis presents work done in the field of nuclear physics. The study of nuclear physics is the quest to understand the origins, structure and properties of the visible matter of the universe. Understanding the constituents of matter has been the quest of scientists from the earliest times and has evolved into a picture where the visible matter of the universe is made up of 6 quarks and 6 leptons combined with four interactions, strong, weak, electromagnetism and gravity. The 12 particles combined with the strong, weak and electromagnetic interactions form the standard model and describes a small fraction of the total matter/energy budget of the universe.

1.1 Quantum Chromodynamics (QCD)

The standard model applies to the wedge of non-dark, non-supersymmetric, baryonic matter that makes up a relatively small fraction of all the matter in the universe and describes, with great success, the world we observe.

The interactions, or forces, are all mediated by an exchange boson which has a characteristic coupling to the charge of the respective interaction.

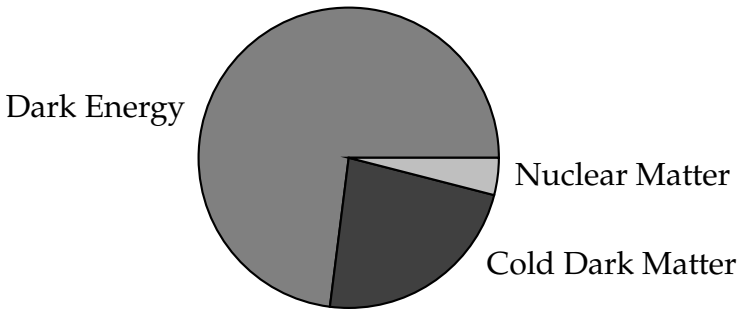

Figure 1.1 — The broad breakdown of our current understanding of the constituents of the universe.

The couplings and masses of the exchange particles dictate the scales over which the various forces are applicable and the properties of the interaction. The weakest of the forces is gravitation, for which there is, as yet, no quantum theory and whose mediating boson remains undiscovered. The charge of gravitation being mass. The weak force is next on the scale of strength and couples to flavour charges, while being mediated by the very massive Z^0 and $W^{\pm}$ bosons. Electromagnetism follows with the massless, charge-less photon as the exchange boson which couples to electric charge. Electromagnetism and the weak interaction have been unified into electroweak theory.

The final interaction, and the one of primary interest in this work, is the strong interaction, described by quantum chromodynamics. It is mediated by the gluon which carries colour charge, the charge of the interaction, and is the key feature which makes this theory different from electroweak theory. The constituents of the standard model are summarised in figure 1.2.

The foundation on which our understanding of nuclear physics is based is the theory of the strong interaction, Quantum Chromodynamics (QCD), a non-abelian gauge theory. QCD coupling constant also runs, being large at low energies and weak at higher energies.

The running coupling and charged mediators give QCD two properties that make it particularly interesting:

confinement [1] which means that the force between quarks does not diminish as they are separated because of the anti-screening of the polarised vacuum. It would take an infinite amount of energy to sepa-

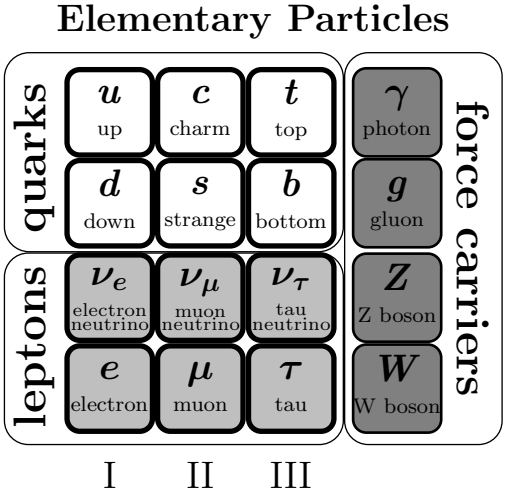

Figure 1.2 — The standard graphic representation of the Standard Model of particle physics. It contains three families each with 2 quarks and 2 leptons as well as the gauge bosons for the interactions.

rate two quarks. Quarks are bound into colour-charge-less hadrons.

asymptotic freedom [2–5] at very large momentum transfer quarks and gluons interact very weakly. That QCD predicts this behaviour was first discovered in the early 1970s by David Politzer and by Frank Wilczek and David Gross. For this work they were awarded the 2004 Nobel Prize in Physics.

Analytically, QCD is very hard to solve but computational methods for solving the path integral formalism using discretisation on a lattice and Monte-Carlo integration techniques has allowed numerical solutions to QCD under certain approximation schemes. This is known as lattice QCD (lQCD). While confinement cannot be proven analytically it can be demonstrated in lQCD [6].

QCD predicts a rich and varied spectroscopy of hadrons and a variety of interesting systems. For example see figure 1.3 which shows a comparison of the measured and lQCD mass spectra from [7].

1.2 QCD Phase Diagram

One state of matter predicted by QCD is a plasma of quarks and gluons [8] called the quark gluon plasma (QGP). In this state the density of coloured

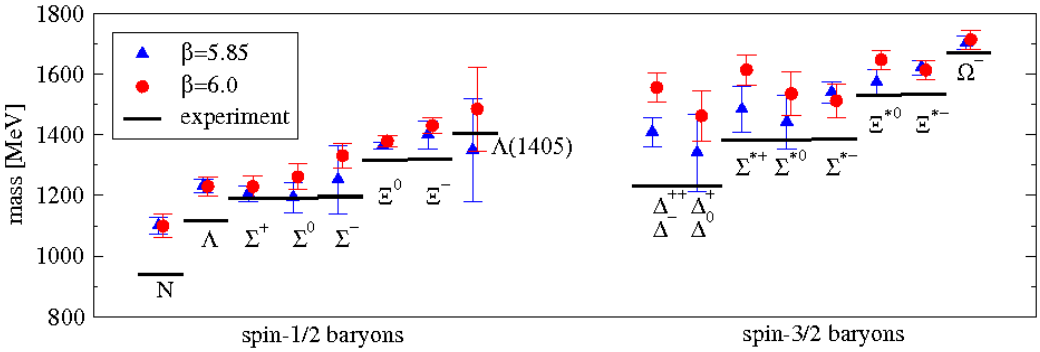

Figure 1.3 — An example of quenched lattice QCD predictions for the spectrum of baryon masses in the specific case of two twisted masses and incorporating a strange quark [7].

objects is high enough that all hadron boundaries are screened away and quarks are free to move over distances larger than those of a typical nucleon. In the limit of high temperature this plasma would be a Stefan-Boltzmann gas of quarks and gluons.

The early universe is thought to have entered this state as it expanded and cooled, eventually undergoing a phase transition as hadrons formed. Lattice QCD results predict that at zero chemical potential ($\mu_B = 0$) the critical temperature at which the phase transition from a QGP to hadron gas occurs is $T_c = 160 - 170$ MeV [9].In figure 1.5 we show the energy as a function of the temperature of the system across the phase transition at T_c from lattice calculations. When the temperature, T, reaches the critical temperature T_c, the number of degrees of freedom rapidly rises indicating that quarks and gluons become relevant degrees of freedom. The arrows represent the Stefan-Boltzmann values for asymptotically high temperature.

In figure 1.4 we show the QCD phase diagram. The region of the diagram that we are interested in is at high temperature and low μ_B. The region at very low temperature and high μ_B is also of interest to many physicists as it is relevant in the study of extremely heavy astrophysical bodies. This region is not accessible in the laboratory, however, the region at low μ_B and high temperature is and will be pursued further in this work.

The only theoretical predictions for the precise location of the phase transition have been from lattice QCD which, up until recently, has been restricted to the asymptotic limit of $\mu_B = 0$. Techniques have been developed

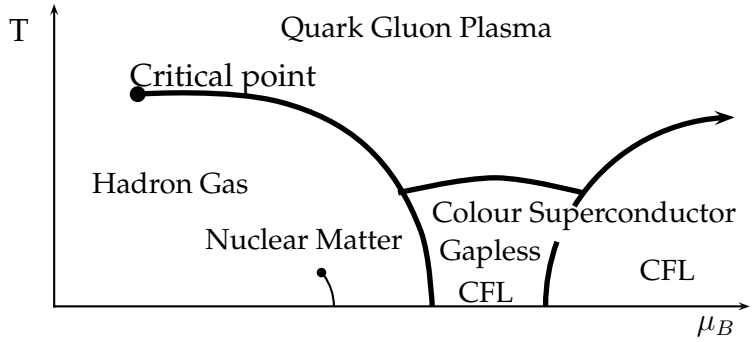

Figure 1.4 — A cartoon of the QCD phase diagram illustrating some of the predicted complexity of the theory.

to make lQCD predictions at non-zero μ_B, which has enabled predictions about the location of the critical point. For μ_B lower than that of the critical point a cross-over is expect between the QGP phase and the hadron phase. The critical point describes the centre of a small region where a second order transition is expected. It also marks the beginning of a line where a first order transition is expected to take place and which is believed to extend to $T = 0$ at some finite μ_B.

For the ultra-dense and cold matter we must look to the universe to provide the experiments for us as such densities and temperatures cannot be created in the laboratory. Fortunately, we are able to conduct experiments to probe the low μ_B and high temperature region of the phase diagram. To do this we turn to ultra-relativistic heavy-ion collisions.

1.3 Heavy-ion Collisions

Ultra-relativistic heavy-ion collisions were thought of as a way of constructing a system at high enough temperature and density that it would achieve forming a system consisting of the QGP [11]. The collisions themselves are not in equilibrium but the system should equilibrate, ideally at a temperature well above the hadronic phase transition and then, as it expands and cools, the system should map out a trajectory in the phase diagram to lower temperature which crosses the phase transition to hadrons.

The collisions are a massive and complex undertaking requiring large ma-

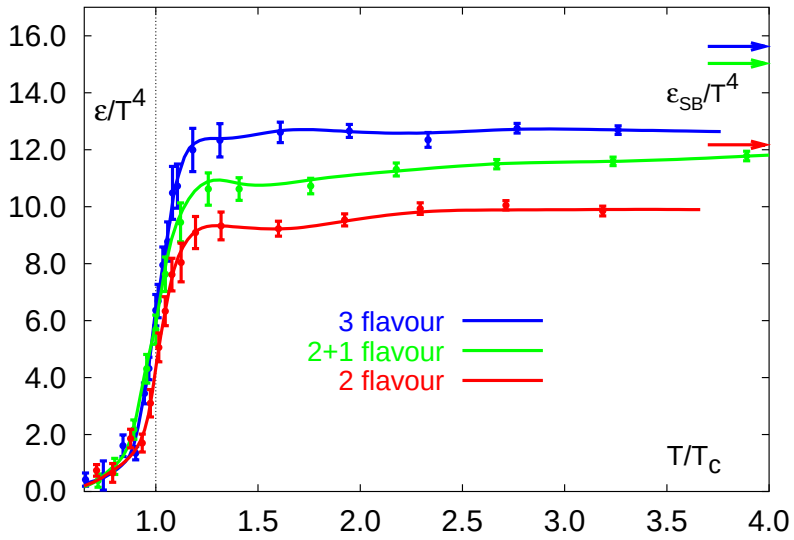

Figure 1.5 — Taken from [10]. Energy as a function of temperature. When the temperature T reaches the critical temperature T_c, the number of degrees of freedom rapidly rises indicating that quarks and gluons become relevant degrees of freedom. The arrows represent the Stefan-Boltzmann values for asymptotically high temperature.

chines capable of accelerating ions to extremely high energies and colliding them, giving rise to complex dynamical systems with a rich variety of observables. A number of facilities for conducting these experiments have been built over the years, with ever increasing energy (table 3.1 details the facilities, their operating periods and energies).

Statistical model fits of the temperature and μ_B to the particle spectra from the various facilities are shown in figure 1.6 [12]. The fit results describe a trajectory of freeze-out points on the T-μ_B plane which evolves to higher temperature and lower μ_B with increasing collision energy. This shows that as $\sqrt{s_{NN}}$ increases the system tends towards baryon- anti-baryon equilibrium, and is hotter.

We will be studying the properties of Au+Au collisions taken at the highest energy available at RHIC. We will provide data that can be used to characterise the density of the system as well as other bulk properties like the speed of sound, prevalence of bound states as well as constrain certain hadronisation scenarios. To fully explain the contribution of this work we must first introduce the field of heavy-ion collisions in more detail. The

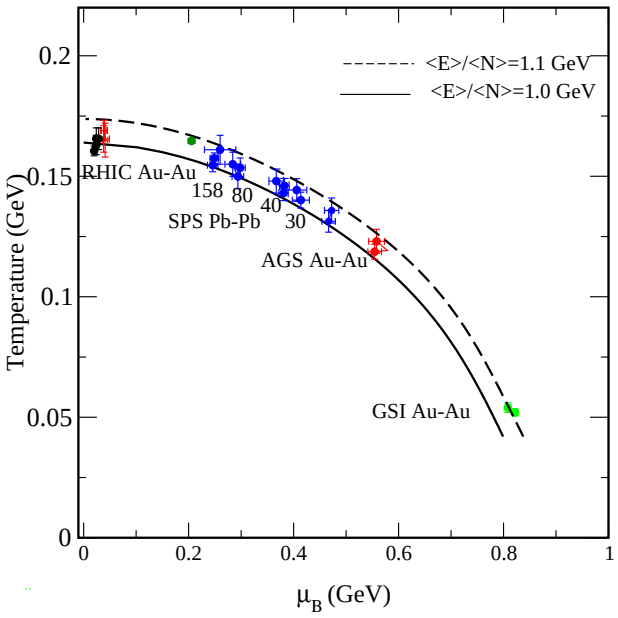

Figure 1.6 — Taken from [12]. Extracted μ_B and temperatures from statistical model fits to particle spectra from various facilities.

scope of this work will be detailed once this introduction has been completed and can be found in section 2.8.

Chapter 2

Heavy-Ion Collisions and Di-hadron Distributions

Go not to the elves for counsel, for they will say both yes and no.

J. R. R. Tolkien

2.1 Overview

We require a well-defined, calculable and calibrated probe which can be used to determine properties of the medium. Ideally this probe will be available from the earliest times of the collision, to ensure it can interact with the hot and dense medium when it is at its most extreme. The interaction of the probe with the medium must have measurable effects.

One such probe is provided, *in situ*, in the form of high-p_T partons from hard scatterings between partons in the incoming nuclei. The hard scattering take place at very early times, before any medium has formed. Before the partons can travel the length of the collision area to fragment in vacuum, a , possibly thermalised, medium of quarks and gluons forms. As the partons traverse this system they interact strongly with the medium, losing energy. By measuring the fragmentation remnants of the hard partons and studying correlated particle production we are able to infer properties of the medium like the gluon density.

We will begin our discussion with the collision system and its bulk proper-

ties, system size, density and thermalisation. This is followed by a discussion of the probes we will use, their interactions with the system created and the current experimental results that are available.

2.2 Bulk Anatomy of the Collision

In Au+Au collisions at RHIC the Au nuclei approach each other with a γ-factor of 108 at $\sqrt{s_{NN}} = 200$ GeV and are highly Lorentz contracted discs. The collision of two of these nuclei, at these energies, is one in which they are largely transparent to each other, though still depositing a large amount of energy in a very small volume. This energy results in a high temperature excitation of the QCD vacuum which liberates thousands of gluons, the precise mechanism by which this happens is not yet well understood.

There are two main groups of models for this mechanism to liberate gluons, coherent and incoherent. An example of an incoherent mechanism is the production of many mini-jets which interact with each other to form an equilibrated plasma. A coherent model is the formation of colour strings and ropes after the impact which subsequently decay into real partons through the Schwinger mechanism [13].

In some way a small, hot and extremely dense system is created.

2.2.1 Centrality

When the two nuclei collide it may not be head-on with complete overlap, in fact, a full range of collisions can occur, from perfectly head-on with complete overlap, to cases where the discs only just graze each other. The degree to which there is overlap is referred to as the centrality of the collision and is measured by the impact parameter, b, the perpendicular distance between the trajectories of the centres of the two colliding nuclei. A perfectly central collision, therefore, corresponds to an impact parameter of $b = 0$ while ultra-peripheral collisions occur when two nuclei have an impact parameter larger than twice their radii so that only the electric fields interact. The schematic below shows the cross-sectional view of a

intermediate centrality event seen down the beamline. The overlap region is the collision region and the impact parameter is shown as the vector b.

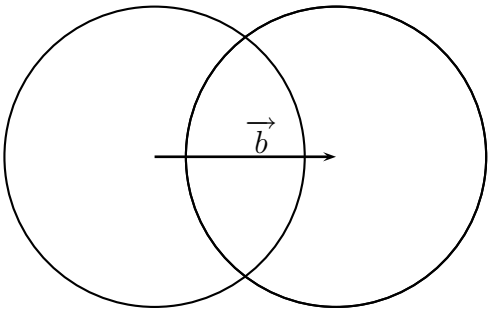

The centrality of a collision determines its size, shape and energy density with more central collisions being larger and more dense. The variation in the shape will be discussed later.

Each nucleus contains many nucleons which may or may not participate directly in the collision depending on the centrality and whether or not they fall in the overlap region. The number of nucleons which participate in the collision can be estimated using a Monte-Carlo Glauber model and we include a brief description in appendix A and for more detailed discussion see [14–17].

Participant nucleons

In the wounded nucleon model [18,19] the number of participating nucleons in the overlap region is on average given by

$$N_{part} = N_{\mathrm{AB}}^{\mathrm{part}}(b) = 2A \int \mathrm{d}\vec{s}\, T_{\mathrm{A}}(\vec{s}-\vec{b}) \left(1-(1-\sigma_{\mathrm{NN}} T_{\mathrm{A}}(\vec{b}))^{A}\right) \tag{2.1}$$

where T_{A} is the thickness function and σ_{NN} is the nucleon-nucleon cross-section (see appendix A). For symmetric collisions $A = B$. Its average value over a given centrality class is calculated in the same way as it is done for the nuclear overlap in A.9.

2.2.2 Energy Deposition

When the nuclei collide they are mostly transparent at RHIC energies. A large amount of energy is liberated in the centre-of-mass frame but most of incident the nucleons are not transported to mid-rapidity as can be seen in figure 2.1 where we show the rapidity distributions for protons as a function of $\sqrt{s_{NN}}$ [20]. It shows that as the collision energy increases so does the degree of transparency with incident protons being transported to mid-rapidity much less.

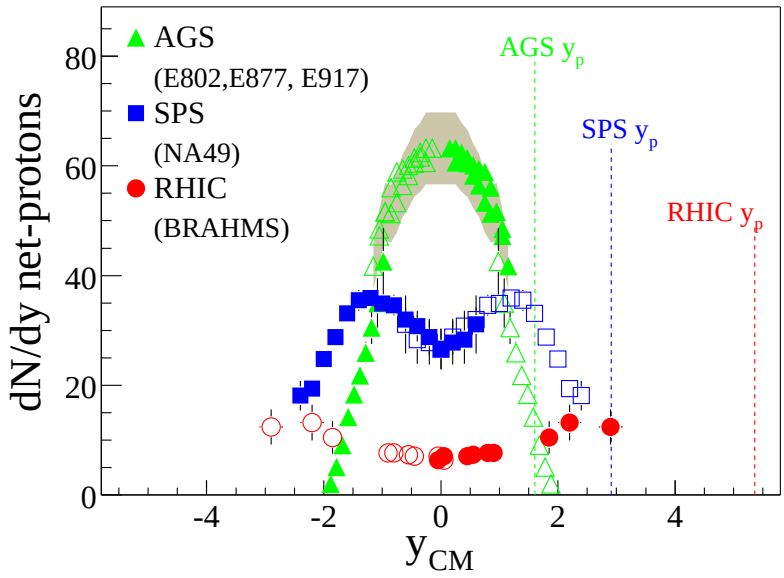

Figure 2.1 — Taken from [20]. The net–proton rapidity distribution at AGS (Au+Au at $\sqrt{s_{NN}}$=5 GeV), SPS (^{208}Pb+^{208}Pb at $\sqrt{s_{NN}}$=17 GeV) and RHIC $\sqrt{s_{NN}}$=200GeV. The data are all from the top 5% most central collisions and the errors are both statistical and systematic. The data have been reflected about $y_{CM} = 0$.. For RHIC data black points are measured and grey points are symmeterised, while the opposite is true for AGS and SPS data (for clarity). At AGS weak decay corrections are negligible and at SPS they have been applied. See references in [20] for data references.

Despite the degree of transparency at RHIC, a significant amount of energy is deposited in the collision region. The Bjorken energy density [21] can be calculated using

$$\epsilon_{Bj} = \frac{1}{A_\perp \tau} \frac{dE_T}{dy}, \tag{2.2}$$

where τ is the formation time and $A_\perp$ is the nuclei transverse overlap area. This is an estimate of the total energy deposited in the collision volume.

Results have been published by the PHENIX collaboration [22] for a systematic study of ϵ_{Bj} as a function of collision energy and centrality. In figure 2.2 (taken from [22]) we present these results, ϵ_{Bj} increases with both increasing centrality (larger, more dense collision) and increasing $\sqrt{s_{NN}}$ (more energetic collision). This along with other results presented in [22] support the creation of a system with energies above the critical 1 GeV/fm and thus above the phase transition to hadronic matter.

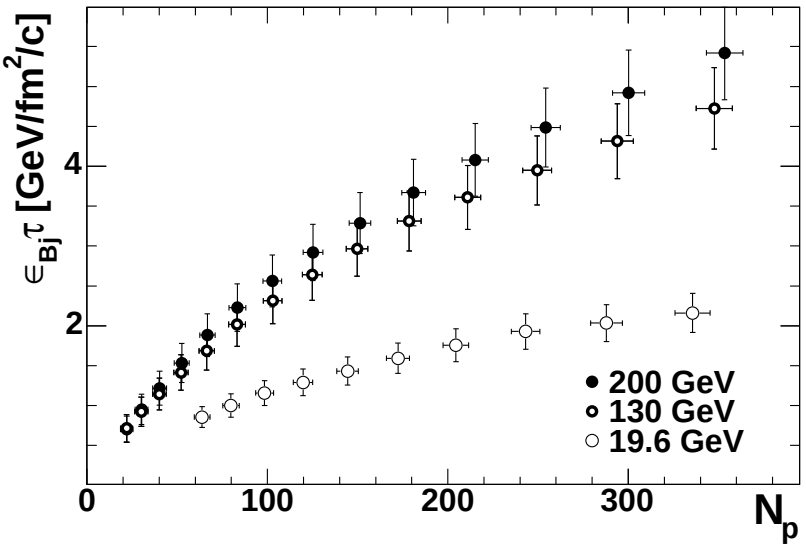

Figure 2.2 — $\epsilon_{Bj} \cdot \tau$ deduced from the PHENIX data at three RHIC energies as a function of number of participating nucleons. Taken from [22].

2.2.3 Hydrodynamics

As we mentioned previously, copious partons are produced which interact strongly and we assume that they become thermalised at some early time, τ_0. This assumption is supported by the success of models based on thermalisation, statistical models for particle yields and specifically hydrodynamics for a number of more differential measurements.

The expansion of the system after τ_0 is then modelled using hydrodynamics. In an ideal case the equations for hydrodynamics are simply the conservation of the energy momentum tensor and the baryon number:

$$\partial_\mu \langle T^{\mu\nu} \rangle = 0, \quad \partial_\mu \langle j_B^\mu \rangle = 0 \tag{2.3}$$

In non-ideal hydrodynamics (see [23] for detailed discussion) one must introduce extra information, for example the viscosity and heat flow. An equation of state $\epsilon = \epsilon(P)$ is required, and for ideal hydrodynamics is obtained from lQCD.

Using hydrodynamics one models the evolution of the fireball until the density decreases and the partonic fluid undergoes a phase transition to hadrons. The temperature at which the phase transition or freeze-out takes place is τ_f. It must be mentioned that there are two distinct freeze-outs although their temperatures may be the same. The chemical freeze-out occurs when the energy density has dropped to the point where the relative species abundances can no longer change (inelastic scatterings cease). The thermal freeze-out occurs when the density is low enough that all scatterings cease.

For a comprehensive overview of hydrodynamic results compared to data see [24]. The extent to which ideal hydrodynamics has been able to reproduce results from RHIC has lead to the general acceptance that the viscosity is very small [24–27].

2.2.4 Radial Flow

The system formed at RHIC exhibits very strong radial expansion. This is supported by the fact that a variety of identified particle spectra can be fitted with a common temperature if a common radial velocity boost is included [28].

2.2.5 Elliptic Flow

In a non-central collision the overlap region is asymmetric in the plane transverse to the beam direction. Any interactions in the system created can convert this spatial anisotropy into a momentum space anisotropy, due to asymmetric pressure gradients resulting in larger accelerations of particle or fluid cells along the short axis rather the long axis.

The shape of the system can be characterised by the eccentricity (ε),

$$\varepsilon = \frac{\langle y^2 \rangle - \langle x^2 \rangle}{\langle y^2 \rangle + \langle x^2 \rangle}. \tag{2.4}$$

The eccentricity can be analytically calculated for a given density profile or calculated using Monte Carlo techniques, where the positions of those nucleons that participate in the reaction are used to calculate the averages in equation 2.4.

The azimuthal anisotropy of the spectra, resulting from the asymmetric pressure gradients, can be characterised in terms of Fourier coefficients, which at RHIC are dominated by the elliptic flow [29], the second Fourier coefficient, $v_2(p_T)$, where

$$E\frac{d^3N}{d^3p} = \frac{1}{2\pi}\frac{d^2N}{p_T dp_T dy}(1 + \sum_{n=1}^{\infty} 2v_n \cos(n(\phi - \Psi_r))), \tag{2.5}$$

where Ψ_r denotes the reaction plane angle, and the sine terms vanish due to the reflection symmetry with respect to the reaction plane. The reaction plane is the plane defined by the vector between the centres of the colliding nuclei and the beam axis. Detailed discussion of the determination of $v_2(p_T)$ using different methods with different sensitivities to the various event constituents can be found in [30]. We adopt the terminology and notation from [30] and will use the bounding results, $v_2\{RP\}$ and $v_2\{4\}$ as our systematic uncertainty in $v_2(p_T)$ and use the mean as the nominal result.

If hydrodynamic flow is taken as the mechanism for generating elliptic flow, then the observation of substantial amount of elliptic flow can be taken as evidence for local thermal equilibrium. The thermal equilibrium must occur early in the system evolution because the anisotropy is self-quenching. Any measurement of elliptic flow must have developed at early times as the asymmetry in pressure gradients will be reduced with time specifically due to the asymmetric pressures gradients.

All hydrodynamic models require quite short thermalisation times, from 0.6–1.0 fm/c, in order to reproduce the magnitude of elliptic flow observed at RHIC [24]. The eccentricity and thermalisation time are sensitive to the exact initial conditions. The observables at RHIC can be well reproduced using relativistic ideal hydrodynamics which has lead to the conclusion

that the viscosity in the medium created in RHIC collisions is very small.

The most direct evidence that v_2 is related to spatial asymmetries present early in the reaction is that v_2 at low p_T approximately scales with the initial eccentricity (ε) of the reaction zone.

In figure 2.3 we show the measured v_2 normalised by ε as a function of centrality for different p_T ranges taken from [31]. At low momentum v_2/ε is independent of centrality to within 20%. This scaling is increasingly broken at higher p_T.

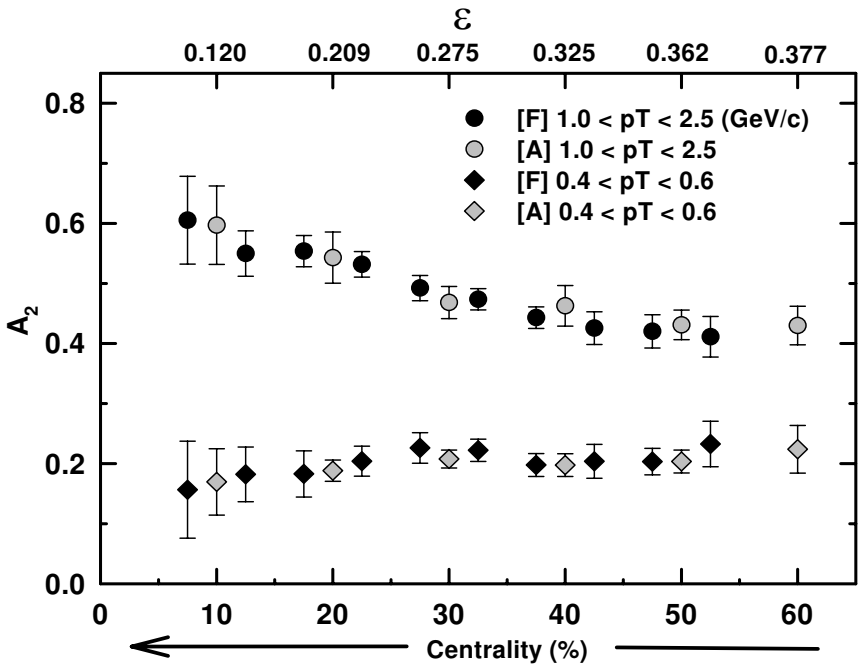

Figure 2.3 — $A_2 = v_2/\varepsilon$ vs. centrality for Au+Au collisions at $\sqrt{s_{NN}}$ = 130 GeV [31]. The data points come from two different types of two-particle correlations: "fixed" p_T correlations when both particles are at the same p_T (points are labelled as "F"), and "assorted" p_T correlations when the two particles have different p_T (points are labelled as "A"). In this case the labelled p_T range is for the higher-momentum particle of the pair.

The correlation of all particles with the reaction plane, through elliptic flow, is important in this work because this correlation will affect the backgrounds that need to be taken into account.

Elliptic flow has been studied extensively and a number of interesting results have appeared, in particular the constituent quark scaling of v_2. In

figure 2.4, taken from [32], the measured v_2 values for identified particles, $\pi^{\pm}$, Ks, protons, Λs and charged hadrons, from PHENIX and STAR, are shown. At low p_T the particle types follow a hydrodynamic mass ordering but above ~ 1.5 GeV/c there is a flattening and switchover of the ordering and the results no longer follow hydrodynamic curves.

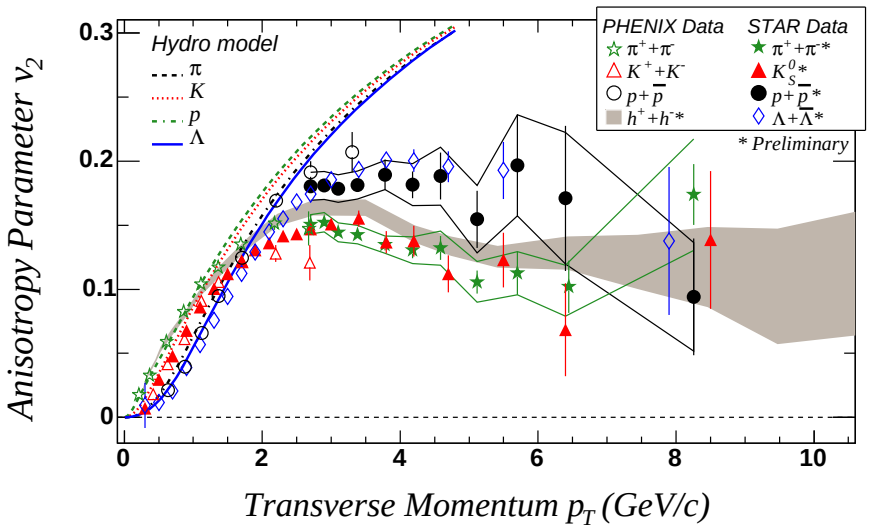

Figure 2.4 — Taken from [32]. Elliptic flow measurements at mid-rapidity from minimum-bias Au+Au collisions at $\sqrt{s_{NN}} = 200$ GeV as function of p_T for identified particles and charge hadrons. The bands around the STAR preliminary measurements of pions and protons represent systematic uncertainties mostly from non-flow correlations. The PHENIX measurements are made by correlating hadrons at middle rapidity with an event-plane measured using hadrons at $3.1 < |\eta| < 4.0$.

It has been noted that the particles fall in two bands about the charged hadron band in figure 2.4. All the mesons fall below the charged hadron band and all the baryons fall above it. This is in stark contradiction to lower p_Ts where there is a distinct mass ordering. Recent results for ϕ-meson v_2 [33], which is of similar mass to protons and Λs have shown that this effect is indeed related to the number of valence quarks and not the mass.

In figure 2.5 the constituent quark hypothesis is tested by dividing the v_2 and the p_T by the number of valence quarks in the particle under study. At first glance in the top panel of figure 2.5, a universal scaling is observed, implying that the v_2 is carried by the quarks forming the hadrons. We will

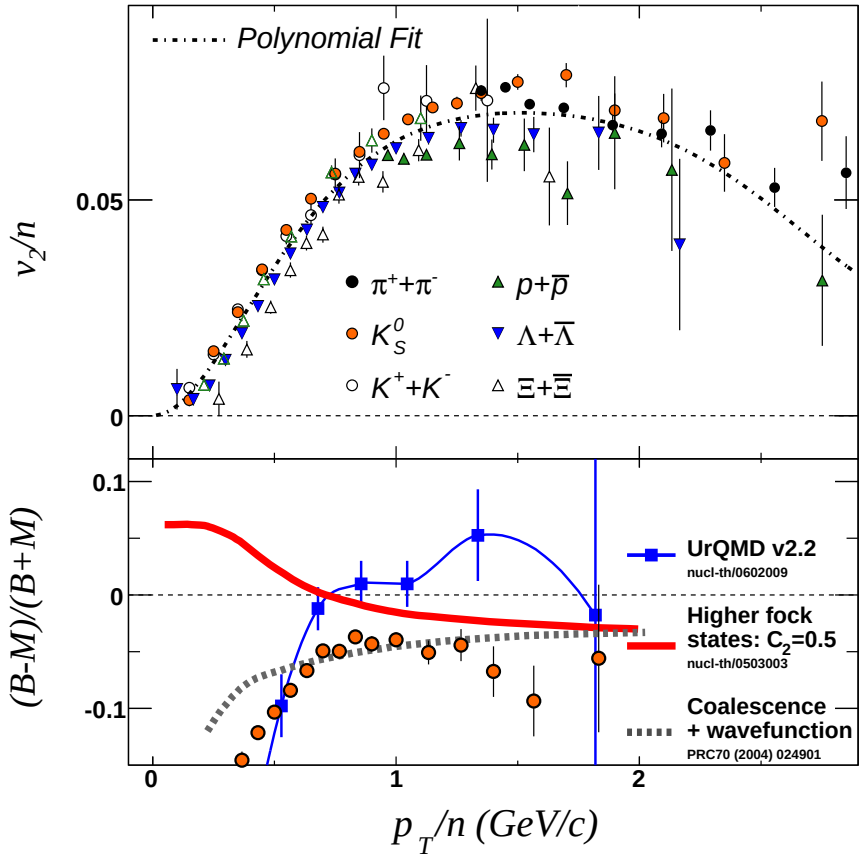

Figure 2.5 — Taken from [32]. Top panel: Quark number scaled elliptic flow for identified hadrons (Preliminary) [34, 35]. A polynomial is fit to all data points. Bottom panel. The difference between quark number scaled baryon v_2 and quark number scaled meson v_2 divided by the sum: $(B-M)/(B+M)$. Here the ratio is taken using $\Lambda + \overline{\Lambda}$ and K^0_S. Model predictions are also shown on the lower panel. The model that provides the best description of the data is the recombination model that takes the wave-function of the hadron into account. Kaon and Λ data were used for the UrQMD model comparison.

discuss this result in section 2.6.

An extremely dense medium, the bulk of which can be modelled well using relativistic ideal hydrodynamics, is formed in Au+Au collisions at RHIC.

2.3 *In Situ* Probes

The partons in the incoming nuclei can undergo hard scatterings resulting in azimuthally back-to-back correlated pairs of partons. These partons could be treated just as in nucleon-nucleon collisions were it not for them having to traverse and interact with the medium. The calculation of the rate of production of these probes is done using perturbative QCD.

2.3.1 Perturbative QCD

The foundation of the application of pQCD to the theory of high-energy inclusive processes is the concept of factorisation [36].

Applications include the inclusive production of new, heavy particles, such as the Higgs boson or the super-symmetric partners of the currently known particles. These theorems apply to inclusive cross sections for the production of a set F of heavy particles or of a system of hard partons with a total mass Q,

$$A + B \to F(Q) + X\,. \tag{2.6}$$

Q must be large, for the purposes of expansion, typically one assumes Q is of the order of the AB invariant mass $\sqrt{s}$.

Factorisation relies on being able to write the cross-section for (2.6) as a convolution of parton distributions and perturbative hard scattering functions which are independent of each other,

$$\begin{aligned}\sigma_{AB} \;=\; & \sum_{ab} \int dx_a dx_b\, \phi_{a/A}(x_a,\mu^2)\, \phi_{b/B}(x_b,\mu^2) \\ & \hat{\sigma}_{ab}\left(\frac{Q^2}{x_a x_b s}, \frac{Q}{\mu}, \alpha_s(\mu)\right)\left(1+\mathcal{O}\left(\frac{1}{Q^P}\right)\right)\,. \end{aligned} \tag{2.7}$$

Where the functions $\phi_{c/C}(x_c,\mu^2)$ give the parton, c, distribution functions, C, as a function of the longitudinal momentum fraction x_c, evolved to factorisation scale μ. The hard-scattering cross-section $\hat{\sigma}_{ab}$ is computed in perturbation theory up to order α_s^N requiring corrections of order α_s^{N+1}. Corrections are suppressed by a positive power, P, of the large mass.

To determine the distributions of final state hadrons (jets) in the case where the resulting system is one of hard partons, 2.7 must be convoluted with fragmentation functions. The fragmentation function, $D_q^h(z, \mu^2)$, describes the probability for a parton q created at the scale $1/\mu$ to fragment into hadron, h, which carries the fraction of qs momentum z. It is not possible to determine fragmentation functions from first principles [37].

The analysis of any piece of distribution functions [38–42], cross-sections and fragmentation functions requires simultaneous fits of all these to data. The quark distribution functions are well constrained from deep inelastic scattering (DIS) experiments while the gluon distributions are much less constrained. A vast quantity of literature exists on the topics of fragmentation functions (see for example [43–50]).

Binary scaling

From the last two equations of appendix A we get binary collision scaling of hard processes, in the collision of A with B,

$$\left\langle N_{\mathrm{AB}}^{\mathrm{hard}} \right\rangle (b_1, b_2) = \left\langle N_{\mathrm{AB}}^{\mathrm{coll}} \right\rangle (b_1, b_2)\, \sigma_{\mathrm{NN}}^{\mathrm{hard}} / \sigma_{\mathrm{NN}} \tag{2.8}$$

and using A.4 with A.9 we find for the cross-section

$$\sigma_{\mathrm{AB}}^{\mathrm{hard}}(b_1, b_2) = \langle T_{\mathrm{AB}} \rangle (b_1, b_2)\, f_{\mathrm{AB}}^{\mathrm{geo}}(b_1, b_2)\, \sigma_{\mathrm{AB}}^{\mathrm{geo}} \sigma_{\mathrm{NN}}^{\mathrm{hard}} \tag{2.9}$$

As each incoming nucleon can undergo multiple hard scattering N_{bin} may be significantly larger than N_{part}.

2.3.2 Experimental Verification

pQCD has been tested extensively at RHIC. In figure 2.6 (taken from [51]) we show results from the PHENIX experiment for π^0 measurements p+p collisions at $\sqrt{s_{NN}} = 200$ GeV over a large range in p_T. Also shown are comparisons to pQCD results using different fragmentation functions (for discussion see [51]). pQCD results match the data well over a large range of p_T.

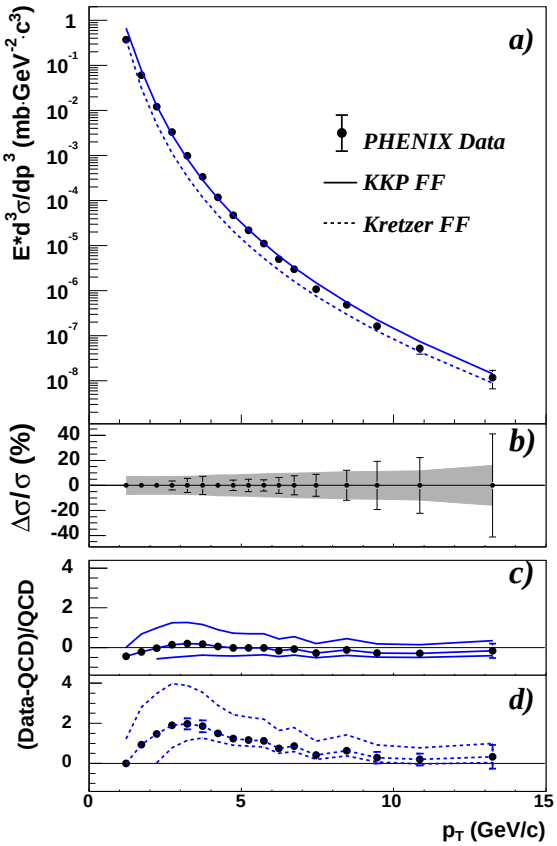

Figure 2.6 — Figure taken from [51]. a) The invariant differential cross-section for inclusive π^0 production (points) and the results from NLO pQCD calculations with equal renormalisation and factorisation scales of p_T using the "Kniehl-Kramer-Pötter" (solid line) and "Kretzer" (dashed line) sets of fragmentation functions. b) The relative statistical (points) and point-to-point systematic (band) errors. c,d) The relative difference between the data and the theory using KKP (c) and Kretzer (d) fragmentation functions with scales of $\frac{1}{2}p_T$ (lower curve), p_T, and $2p_T$ (upper curve). In all figures, a normalisation error of 9.6% is not shown.

2.3.3 Jet Features

The fragmentation of hard partons into jets of hadrons has some specific characteristics which can be used to identify them in heavy-ion collisions. The precise mechanism by which the fragmentation occurs is, as yet, unknown and a number of models exist (see, for example, Lund string fragmentation [52]).

The jets of hadrons fall within a cone of radius $R = \sqrt{(\Delta\eta)^2 + (\Delta\phi)^2} \lesssim 1$. The larger the fraction of energy carried by a hadron the more colli-

mated that hadron is with the original parton axis. The characteristics of hadron species and frequency within jets is characterised by the fragmentation functions, which are approximately exponential for the light partons which dominate this study. Hadron multiplicity in the jet is larger for higher momentum partons.

In hadron collisions the pair of hard-scattered partons are not strongly correlated in pseudo-rapidity due to their internal motion in the incoming nucleons, however they are strongly correlated in azimuthal angle from momentum conservation. This correlation is modified slightly by initial and final state scatterings [53] and radiative effects [54] which introduce some acoplanarity into the system.

In an isolated $2 \rightarrow 2$ hard scattering one should see a di-jet structure of collimated hadrons which are azimuthally back-to-back. This is well known from p+p colliders, see for example [55]. The highest momentum hadron in each jet will be the leading hadron and will give an approximation of the fragmenting parton direction. The shape of the hadron distribution within a jet is well described by a symmetric two-dimensional Gaussian peaked at $\Delta\phi = \Delta\eta = 0$. For detailed discussion of jet shapes and momentum distributions measured at RHIC see [56].

2.4 Partonic Energy Loss

The hard partons that can be calculated using pQCD occur in Au+Au collision and the rate can be deduced by scaling the p+p results by the number of binary collisions for Au+Au centrality under study.

It is a means of coupling the perturbative and calculable hard sector to the non-perturbative soft sector. A lot of work has been done on understanding the effect of hard, coloured partons traversing the dense coloured medium created in the collision since it was predicted as a means for studying the medium [57–59], specifically properties like the gluon density. The p_T-broadening and gluon radiation induced by multiple scatterings can be a significant effect.

There are two main effects; elastic- (collisional) and inelastic-processes (radiative). In the former case the propagating parton participates in many two-body scatterings and for the latter case the energy loss is through Bremsstrahlung during the collisions with the matter. At high energies the radiative loss becomes dominant and is given by the Bethe-Heitler formula. If the matter density is high enough then multiple scatterings can occur before the radiation of a gluon. This can destructively interfere causing a suppression of the Bethe-Heitler radiation. The phenomenon is analogous to the Landau, Pomeranchuk and Migdal effect from QED [60, 61] (reviewed in [62]) where incoherence of the scatterings plays a significant role in suppressing the radiation spectrum.

2.4.1 Gluon Bremsstrahlung or Inelastic Energy Loss

Baier, Dokshitzer, Peigné and Schiff [63] have shown that the dominant mechanism for energy loss of a parton moving through the medium is the diagram shown in figure 2.7, where the gluon undergoes multiple scatterings in the medium after being radiated.

The Bremsstrahlung gluon spectrum radiated by the parton, in the eikonal approximation, and modified by the multiple scatterings is given by:

$$dI^{\text{vac}} = C_{F,A}\frac{\alpha_s}{\pi}\frac{dk_\perp^2}{k_\perp^2}\frac{d\omega}{\omega}\,. \tag{2.10}$$

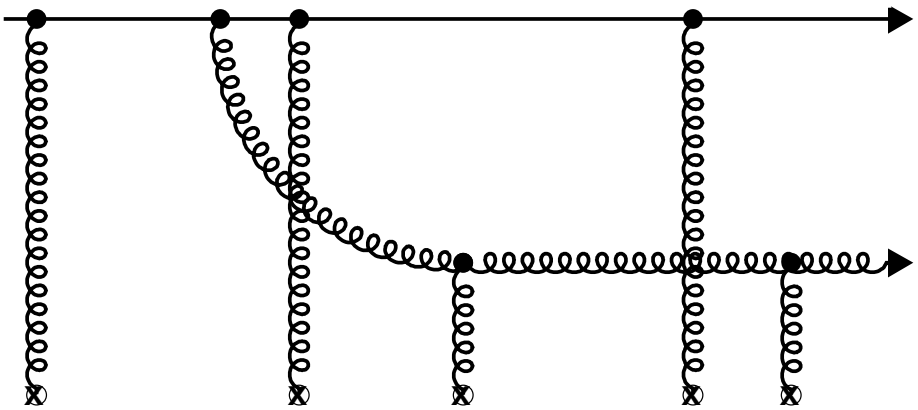

Figure 2.7 — As depicted in [63], the dominant diagram for the energy loss of a hard parton propagating through a hot and dense QCD medium.

The total gluon Bremsstrahlung spectrum is of the form

$$\omega \frac{dI^{\text{tot}}}{d\omega\, d\mathbf{k}_\perp} = \omega \frac{dI^{\text{vac}}}{d\omega\, d\mathbf{k}_\perp} + \omega \frac{dI^{\text{med}}}{d\omega\, d\mathbf{k}_\perp}\,, \tag{2.11}$$

where the medium modifications are power-suppressed, but larger than other power-suppressed corrections due to enhancements proportional to the nuclear size.

To account for the mean free path between scatterings, not present in the vacuum case, the eikonal approximation is no longer valid and transverse Brownian motion of the produced partons, which results in a medium dependence via the path-integral [64, 65]

$$\mathcal{K}(\mathbf{r}_1, z_1; \mathbf{r}_2, z_2) = \int_{\mathbf{r}(z_1)}^{\mathbf{r}(z_2)} \mathcal{D}\mathbf{r} \exp\left[\int_{z_1}^{z_2} d\xi \left[i\frac{\omega}{2}\dot{\mathbf{r}}^2 - \frac{1}{2}n(\xi)\sigma(\mathbf{r})\right]\right], \tag{2.12}$$

where

$$e^{-\frac{1}{2}n(\xi)\sigma(\mathbf{r})} \equiv \left\langle e^{iA_a^+(\mathbf{x},\xi)T^a} e^{-iA_b^+(\mathbf{x}+\mathbf{r},\xi)T^b} \right\rangle. \tag{2.13}$$

In the limit of large gluon energy ω, the path integral (2.12) approaches the eikonal limit. In (2.13), the colour field strength presented to the projectile is parameterised in terms of a longitudinal density $n(\xi)$ times a measure of the transverse field strength per unit path-length, $\sigma(\mathbf{r})$. In terms of this target average, the medium-modification (2.11) of the gluon Bremsstrahlung spectrum to leading order in parton energy and for arbitrarily large target

colour field reads [65, 66]

$$\omega \frac{dI^{\text{med}}}{d\omega\, d\mathbf{k}_\perp} = \frac{\alpha_s\, C_R}{(2\pi)^2\, \omega^2}\, 2\text{Re} \int_{\xi_0}^{\infty} dy_l \int_{y_l}^{\infty} d\bar{y}_l \int d\mathbf{u}\, e^{-i\mathbf{k}_\perp \cdot \mathbf{u}} \times e^{-\frac{1}{2}\int_{\bar{y}_l}^{\infty} d\xi\, n(\xi)\, \sigma(\mathbf{u})}\, \frac{\partial}{\partial \mathbf{y}} \cdot \frac{\partial}{\partial \mathbf{u}}\, \mathcal{K}(\mathbf{y}=0, y_l, \mathbf{u}, \bar{y}_l)\,. \tag{2.14}$$

For numerical applications, one approach is an opacity expansion of 2.14 which amounts to expanding the integrand in powers of the density $n(\xi)$ [65, 67]. Alternatively, one exploits that the main support of the integrand of (2.14) is for small transverse distances which permits the harmonic oscillator approximation of the path integral with [64, 65, 68]

$$n(\xi)\, \sigma(\mathbf{r}) \approx \frac{1}{2} \hat{q}(\xi)\, \mathbf{r}^2\,. \tag{2.15}$$

Here, $\hat{q}$ is the BDMPS transport coefficient and, physically, it characterises the average squared transverse momentum transferred from the medium to a hard gluon per unit path length.

Remarkably, for a static medium without time evolution, the small-distance properties of 2.13 can be shown to determine the main properties of the medium-induced gluon radiation spectrum. Momentum broadening is characterised by $\langle k_\perp^2 \rangle \sim \hat{q} L_{\text{med}}$ [68], the energy distribution is determined by the characteristic energy scale $\omega_c = \frac{1}{2}\hat{q} L_{\text{med}}^2$ [68], and medium effects regulate the additional gluon radiation in the infrared on a scale $\omega \sim \omega_c / \left(\hat{q} L_{\text{med}}^3\right)^{2/3}$ [69].

For an expanding medium, the transport coefficient decreases with time - this translates into a path dependence $\hat{q} = \hat{q}(\xi)$ [70–72]. One finds, however, that the medium-induced gluon radiation spectrum for a dynamically expanding case is the same as that obtained for a static medium of rescaled linear line-averaged transport coefficient [72]

$$\bar{\hat{q}} = \frac{2}{L_{\text{med}}^2} \int_0^{L_{\text{med}}} \tau\, \hat{q}(\tau)\, d\tau\,. \tag{2.16}$$

Data can be analysed in terms of static medium properties and a transport coefficient extracted and then translated back to a realistic dynamical one.

2.4.2 Collisional (Elastic) Energy Loss

Collision energy loss is the energy lost in elastic processes. In the case where the hard parton is represented by Q and constituents of the medium are represented by lower-case characters, the processes of interest are: $Qq \to Qq$ and $Qg \to Qg$.

The energy loss per unit length is dependent on the density of scatterers ρ_p with momentum $\vec{k}$ and on the differential cross-section weighted by the energy transfer $\omega = E - E'$, where E (E') is incoming (outgoing) energy of Q,

$$-\frac{dE}{dz} = \sum_{p=q,g} \int d^3k \rho_p(\vec{k}) \int dq^2 \, J\omega \frac{d\sigma^{Qp\to Qp}}{dq^2}. \tag{2.17}$$

J is a flux factor and q^2 is the square of the four-momentum transfer in the process. The process is dominated by small momentum transfers as [59]

$$\frac{d\sigma^{Qp\to Qp}}{dq^2} \simeq C_p \frac{2\pi\alpha_s^2}{(q^2)^2}, \tag{2.18}$$

with $C_q = \frac{N_c^2-1}{2N_c^2}$, $C_g = 1$ for N_c colors. For a QGP in thermal and chemical equilibrium the densities are given by

$$\rho_q = \frac{4N_cN_f}{(2\pi)^3} n_F(k), \; \rho_g = \frac{2(N_c^2-1)}{(2\pi)^3} n_B(k), \tag{2.19}$$

where $n_F(n_B)$ are the Fermi-Dirac (Bose-Einstein) distributions. This has been shown to be [73,74]

$$-\frac{dE}{dz} = \pi\alpha_s^2 \sum_p C_p \int \frac{d^3k}{k} \rho_p(k) \ln\frac{q^2_{\text{max}}}{q^2_{\text{min}}} \simeq \frac{4\pi\alpha_s^2T^2}{3}\left(1+\frac{N_f}{6}\right)\ln\frac{cE}{\alpha_sT}, \tag{2.20}$$

with c a numerical constant of $O(1)$, and $N_c = 3$. The strong coupling constant may be evaluated at the scale $\alpha_s(T)$ for high temperature T.

As (2.20) is dependent on T^2 it is proportional to $\sqrt{\epsilon}$ [73], where ϵ is the energy density of the QGP and, to leading order in the coupling, is given by [75]:

$$\epsilon = 8\pi^2T^4(1+21N_f/32)/15 \tag{2.21}$$

In thermal field theory, using re-summed perturbation theory at high temperature, it is possible treat the screening effects of the plasma consistently and properly. From this one calculates the hard thermal-loop (HTL) corrections to the propagator of the exchanged gluon in the processes: $Qq \to Qq$ and $Qg \to Qg$. To calculate the energy loss in this field theoretic framework one is required to calculate the discontinuity in the two self energies show in figure 2.8.

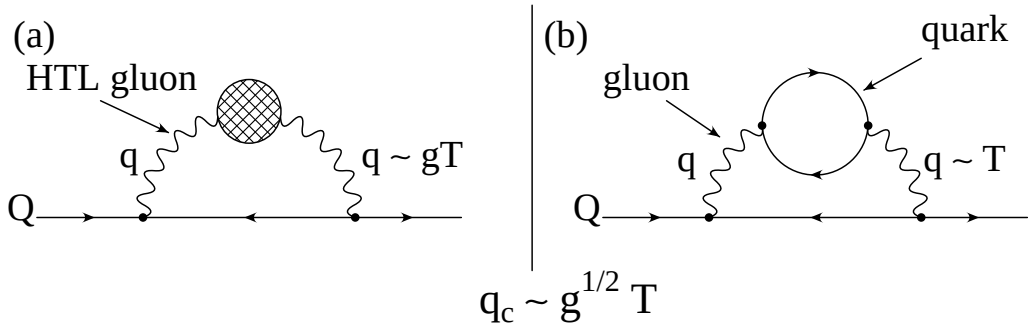

Figure 2.8 — (a) The diagram describing the process for $q < \sqrt{g}T$ where the hard thermal loop corrections contribute to the gluon propagator. (b) The tree level elastic scattering to be calculated when $q \sim T$.

Original expectation for collisional energy loss of light quarks propagating through a medium of temperature, $T = 250$ MeV, were 0.2-0.3 GeV/fm [74, 76]. For gluon jets the energy loss is expected to be a factor $2N_c^2/(N_c^2 - 1) = 9/4$ larger due to the additional colour charge.

Following the treatment in [77–80] the quantum corrections to the tree level diagrams, and the renormalisation required, define the coupling strength. Thus the assumption of a constant coupling is wrong. This implies that although the collisional energy loss may not necessarily dominate it should be taken into account for quantitative comparisons between data and theory and is larger than in [74,76].

2.4.3 Experimental Verification

The experimental support for parton energy loss or jet quenching is based largely on two results; the nuclear modification factor and azimuthal angular di-hadron distributions.

Nuclear Modification Factor

Nuclear effects on hadron production in d+Au and Au+Au collisions are measured through comparison to the p+p spectrum using the ratio

$$R_{AB} = \frac{d^2N/dp_T d\eta}{T_{AB}\, d^2\sigma^{pp}/dp_T d\eta}\,, \tag{2.22}$$

where $d^2N/dp_T d\eta$ is the differential yield per event in the nuclear collision $A+B$, $TAB = \langle N_b^C \rangle / \sigma_{inel}^{pp}$ describes the nuclear geometry, and $d^2\sigma^{pp}/dp_T d\eta$ for p+p inelastic collisions is determined from the measured p+p differential cross section [81]. In the absence of nuclear effects such as shadowing, the Cronin effect, or gluon saturation, hard processes are expected to scale with the number of binary collisions and $R_{AB} = 1$.

Figure 2.9 (left panel) shows R_{AB} for minimum bias and central d+Au collisions. $R_{AB}>1$ for $2<p_T<7$ GeV/c. R_{AB} may be influenced by nuclear shadowing [82] and its centrality dependence [83]. Figure 2.9 (left panel) also shows R_{AB} for central Au+Au collisions [81], exhibiting large suppression in hadron production at high p_T.

This suppression is attributed to medium induced energy loss (jet quenching) because the fragmentation of hard partons is primary source of these high-p_T hadrons. If the partons lose energy in the medium then the number of high-p_T hadrons will be reduced as shown in [51].

Correlated Di-hadron Distributions

Jet modifications are demonstrated through correlated angular di-hadron distributions, consisting of the distributions of relative angles ($\Delta\phi$ or $\Delta\eta$) between a trigger particle, assumed to be the leading particle in a jet, and associated particles in the event, assumed to be both correlated jet fragments and uncorrelated background [84]. Both trigger and associated particles are restricted to specific ranges in p_T, which we call $p_T^{trig.}$ and $p_T^{assoc.}$ respectively.

Figure 2.9 (right panel a) shows the correlated relative azimuthal angular

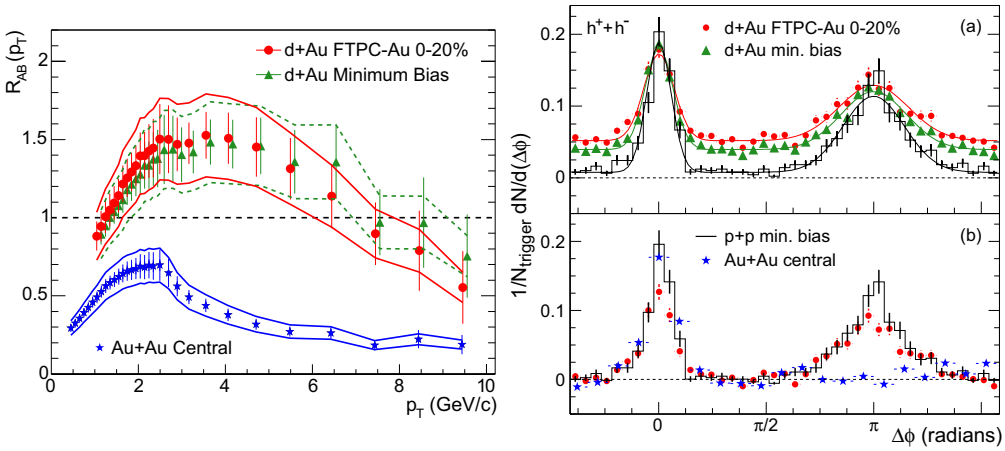

Figure 2.9 — Left panel: R_{AB} from Eq. 2.22 for minimum bias and central d+Au collisions, and central Au+Au collisions [81]. The minimum bias d+Au data are displaced 100 MeV/c to the right for clarity. The bands show the normalisation uncertainties, which are highly correlated point-to-point and between the two d+Au distributions. **Right panel:** (a) Efficiency corrected two-particle azimuthal distributions for minimum bias and central d+Au collisions, and for p+p collisions [84]. Curves are fits for which results can be found in [85]. (b) Comparison of two-particle azimuthal distributions for central d+Au collisions to those seen in p+p and central Au+Au collisions [84]. The respective pedestals have been subtracted.

distribution, normalised per trigger, $D(\Delta\phi)$, defined as

$$D(\Delta\phi) \equiv \frac{1}{N_{trig}} \frac{1}{\epsilon} \frac{dN}{d(\Delta\phi)}, \tag{2.23}$$

for minimum bias and central d+Au collisions, and for p+p collisions [84].

N_{trig} is the number trigger particles within 4.0$< p_T^{trig.} <$6.0 GeV/c. The distribution results from the correlation of each trigger particle with all associated particles in the same event with 2.0$< p_T^{assoc.} <$4.0 GeV/c. and ϵ is the tracking efficiency of the associated particles.

The azimuthal distributions in d+Au collisions include a near-side ($\Delta\phi \sim 0$) peak similar to that seen in p+p and Au+Au collisions [84] that is typical of jet production, and a back-to-back ($\Delta\phi \sim \pi$) peak similar to that seen in p+p and peripheral Au+Au collisions [84] that is typical of di-jet events, the hard probes of interest in this work.

Figure 2.9 (right panel b) shows the pedestal-subtracted azimuthal distributions for p+p and central d+Au collisions. The azimuthal distributions

are shown also for central Au+Au collisions after subtraction of the elliptic flow and pedestal contributions [84]. The near-side peak is similar in all three systems, while the back-to-back peak in central Au+Au shows a dramatic suppression relative to p+p and d+Au.

Measurements have revealed a striking suppression of both the inclusive hadron yield and the back-to-back correlations for central Au+Au collisions. If the suppression is the result of initial-state effects, it also should be observed in d+Au collisions. No suppression in d+Au collisions is observed by any of the RHIC experiments. Rather, the inclusive yield is enhanced and the two-particle azimuthal distributions exhibit little change relative to p+p.

The conclusions reached by all four RHIC experiments is that the suppression is a final state effect [85–88] and is attributed to medium induced energy loss.

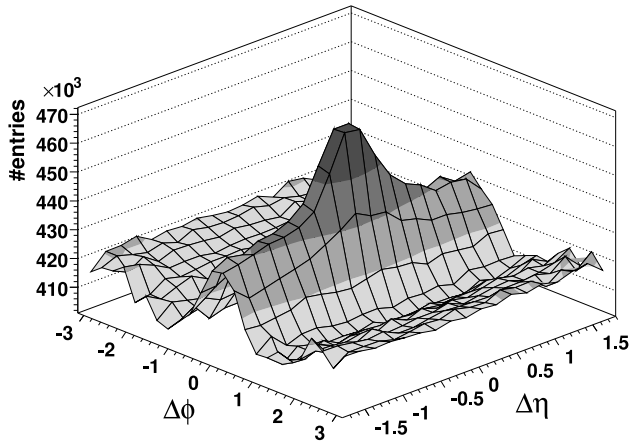

Figure 2.10 — Taken from [89]. Raw $\Delta\eta\times\Delta\phi$ di-hadron correlation function in central Au+Au collisions for 3.0< $p_T^{trig.}$ <4.0 GeV and $p_T^{assoc.} > 2$ GeV.

2.5 Medium Response

Understanding how the energy lost by hard partons is redistributed and how the medium responds can provide significant insight into the system properties. The measurement of Čerenkov radiation would signify the existence of bound states. It may be possible to experimentally determine the speed of sound in the medium.

2.5.1 Near-side $\Delta\eta$ Shape

An enhancement of correlated yield, at $\Delta\eta$ larger than expected from jet fragmentation, has been observed on the near-side. This additional yield is found to extend as far as $\Delta\eta \sim 1.5$ [89] and it persists up to $p_T^{trig.} \sim 9$ GeV/c, indicating that it is, indeed, associated with jet production.

The p_T spectrum of the correlated yield in the ridge has been shown to be only slightly harder than the inclusive spectrum with a spectrum slope difference $\Delta T \approx$ 40-50 MeV [89] and is largely independent of $p_T^{trig.}$.

2.5.2 Energy Redistribution

The significant energy that is lost by the away-side parton must be redistributed. By modifying the $p_T^{assoc.}$ range studied it is possible to as-

sess the response of the bulk to the propagating parton [90]. In figure 2.11, taken from [90], we show the correlated $\Delta\phi$ and $\Delta\eta$ distributions, left and right columns respectively, for 4.0< $p_T^{trig.}$ <6.0 GeV/c for 0.15< $p_T^{assoc.}$ <4.0 GeV/c and 2.0< $p_T^{assoc.}$ <4.0 GeV/c, top and bottom respectively.

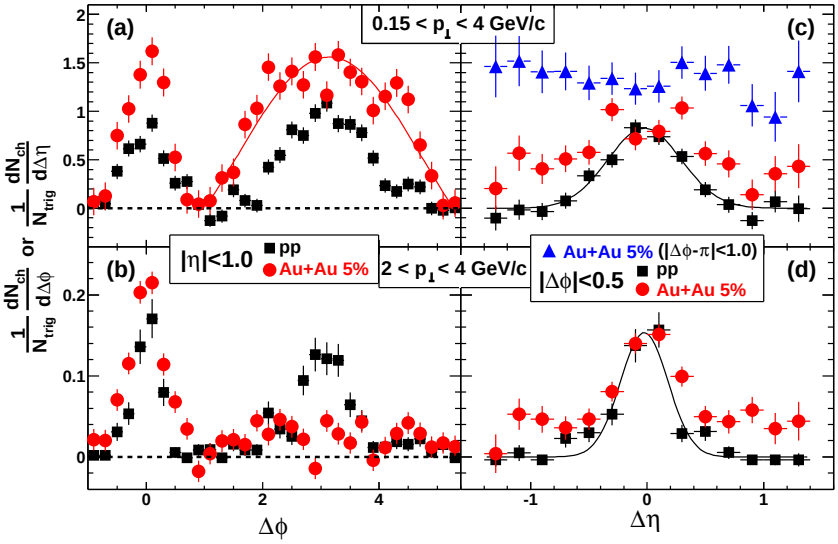

Figure 2.11 — Taken from [90]. Background subtracted (a),(b) $\Delta\phi$ and (c),(d) $\Delta\eta$ distributions for pp and 5-0% central Au+Au for 4<$p_T trig$<6 GeV/c and two associated p_T ranges. The subtracted background level for p_T=0.15-4 GeV/c (2-4 GeV/c) is $\frac{1}{N_{trig}}\frac{dN_{ch}}{d\Delta\phi}$ ≈1.4 (0.007) in pp and ≈211 (2.1) in 5-0% Au+Au. The curve in (a) shows the shape of an $[A - B\cos(\Delta\phi)]$ function. The curves in (c),(d) are Gaussian fits to the pp data.

The away-side yield in panel (a) of figure 2.11 shows that there is a significant enhancement in the yield at low p_T relative to the p+p reference data, indicating that the energy lost has been redistributed to particle production at lower p_T. This does not specify nor constrain the precise mechanism by which the excess particles are produced.

2.5.3 Mach Cones

It has been postulated that the energy deposited in the medium propagate as a collective excitation [91] in response to the shape of the away-side in figure 2.11. As the parton propagates through the medium extremely

rapidly, much faster than the speed of sound, it may excite Mach shock waves or a sonic boom which leads to particle production correlated at certain preferential angles relative to the azimuthal axis of the trigger.

The authors of [91] argue that, in a linearised relativistic hydrodynamic scenario, for RHIC collisions the direction of this flow should make a cone at a specific large angle with the jet, $\sim 70^o$, and thus lead to peaks in particle correlations at the angle $\Delta\phi = \pi \pm 1.2$ rad relative to the trigger particle.

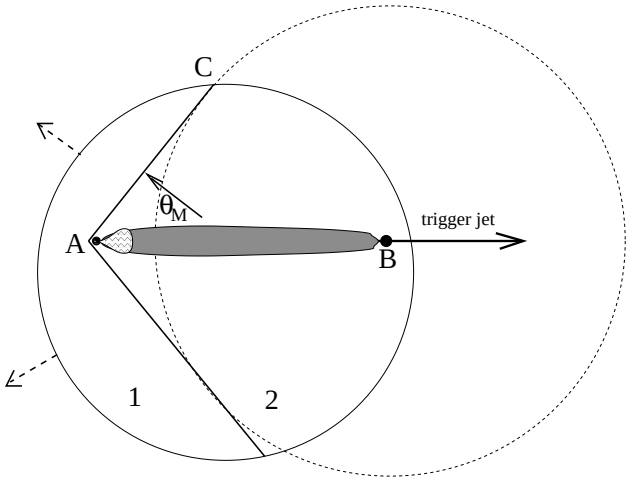

Figure 2.12 — Taken from [91]. A schematic picture of flow created by a jet going through the fireball. The trigger jet is going to the right from the origination point (the black circle at point B) from which sound waves start propagating as spherical waves (the dashed circle). The companion quenched jet is moving to the left, heating the matter and thus creating a cylinder of additional matter (shaded area). The head of the jet is a "non-hydrodynamical core" of the QCD gluonic shower, formed by the original hard parton (black dot A). The solid arrow shows a direction of flow normal to the shock cone at the angle θ_M, the dashed arrows show the direction of the flow after the shocks hit the edge of the fireball.

In the process they do evaluate different possible microscopic thermalisation mechanisms providing two different extreme cases which depend on different terms dominating in the hydrodynamic equations. In one scenario localised heating takes place along the path of the propagating parton, a diffusion mode, which results in no significant shock wave formation while in the other case the majority of the energy is redistributed via second order effects and excites the Mach cone. In this way the discovery of a Mach cone at RHIC may constrain microscopic properties of the medium-parton interaction.

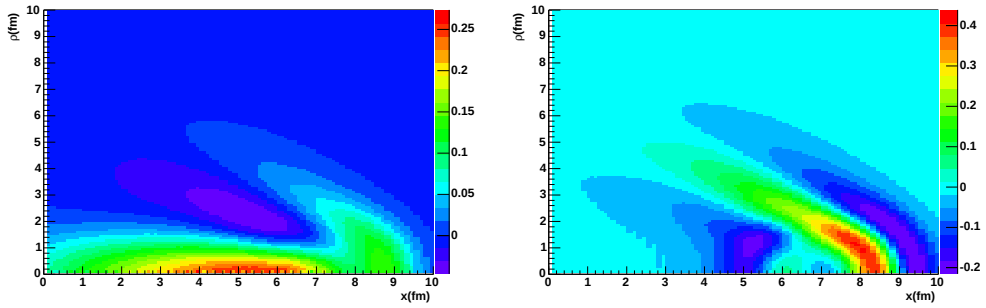

Figure 2.13 — Taken from [91].Velocity field v_x created by a jet moving along the $\hat{x}$ direction. The jet is assumed to disappear at $t = 7$ fm while the spectrum calculated at $t = 10$ fm. The left figure is for the diffusion mode scenario while the right figure is is for the excitation of the Mach cone. The values of the parameters are arbitrary. Note that in (a) matter moves preferentially along the $\hat{x}$ direction, while in (b) it is in the Mach direction

A number of authors have extended the treatment to include medium expansion [92–94] and the distribution of hard scattering centres. In these treatments the Mach cone is distorted (see figure 2.14 for schematic of the distortion due to radial flow) and does not necessarily consist of two peaks but forms a very broad away-side correlation [92, 94, 95].

Experimental data which attempt to probe the away-side shape more differentially using different $p_T^{assoc.}$ and $p_T^{trig.}$ ranges have been presented [96–98]. We include in figure 2.15, for example, the centrality dependence of distributions with 1.0< $p_T^{assoc.}$ <2.5 GeV/c and 2.5< $p_T^{trig.}$ <4.0 GeV/c from [98] where a clear minimum at $\Delta\phi = \pi$ is seen with a peak at ~ 1.2 units away from $\Delta\phi = \pi$, possibly indicative of a Mach cone being formed in the medium.

2.5.4 Deflected Jets

An alternative model for mimicking the Mach cone signal in di-hadron distributions, as they average over events, is to have an event-by-event deflection of the away-side partner through it's interactions with the medium. In this picture it would fragment at some angle away from $\Delta\phi = \pi$ but never favour a particular side and so would form symmetric peaks about $\Delta\phi = \pi$ in di-hadron distributions. This has been studied by the authors of [99] in a Markovian parton scattering model.

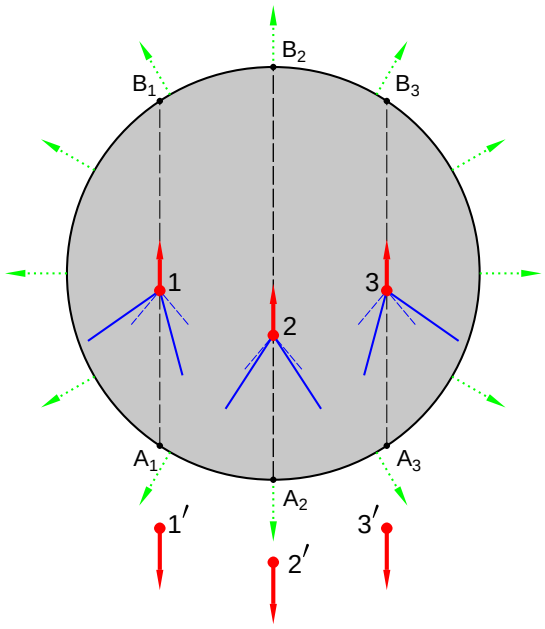

Figure 2.14 — Taken from [92]. Schematic picture of Mach shocks from jets $1, 2, 3$ propagating through the fireball matter (shaded circle) created in a central heavy–ion collision. Dotted arrows represent local velocities of fireball expansion. Thick downward arrows show associated trigger jets. The Mach shock boundaries are shown by solid lines. Short–dashed lines give positions of shock fronts in the case of static fireball.

In figure 2.16 we show in the upper (lower) panel the paths of partons that do (not) fragment in vacuum to form the deflected jet signature. In figure 2.17 we show the resulting comparison to the data from [98]. The authors are also able to reproduce the small away-side peak shown in 2.22, see [99] for details.

2.5.5 Čerenkov Radiation

Although not strictly speaking an effect due to medium response, we include this discussion here as it is intended to explain the features generally attributed to medium response.

The authors of [100, 101] argue that, in the presence of bound states in the medium, Čerenkov radiation of gluons by the hard partons is possible.

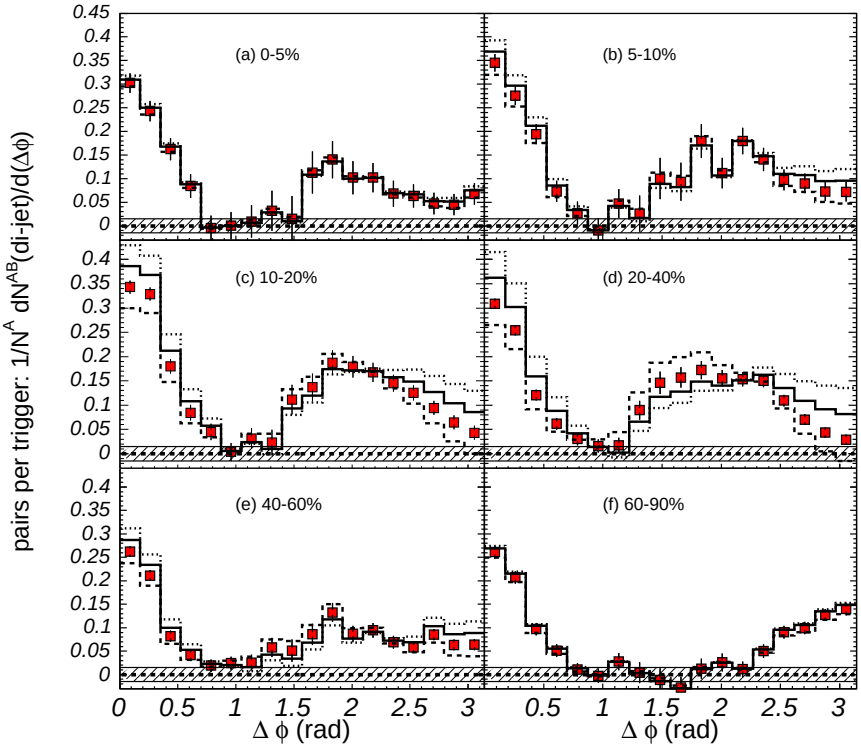

Figure 2.15 — Taken from [98]. Signal di-hadron distributions for 1.0< $p_T^{assoc.}$ <2.5 GeV/c and 2.5< $p_T^{trig.}$ <4.0 GeV/c from Au+Au collisions for various centralities, 0-5%, 5-10%, 10-20%, 20-40%, 40-60%, and 60-80%.

The authors extend the gluon Bremsstrahlung by including further interactions of the radiated gluon with the medium. At high enough temperatures an effective gluon propagator can be used to re-sum all HTLs, where it has been shown in [102] for the case of heavy quarks. This treatment is known to diverge from lQCD results if the temperatures is above, but close to, T_C [103, 104].

In this non-perturbative region, supported by the empirical observation of the strongly coupled medium created in central Au+Au collisions at RHIC, it is argued that a gluon dispersion relation different to at high temperature is reasonable [103, 104]. The RHIC observations have led to the suggestions that the QCD matter could become effectively composed of medium-modified (heavy) quarks and gluons and their screened Coulomb potential could lead to many shallowly bound states [105].

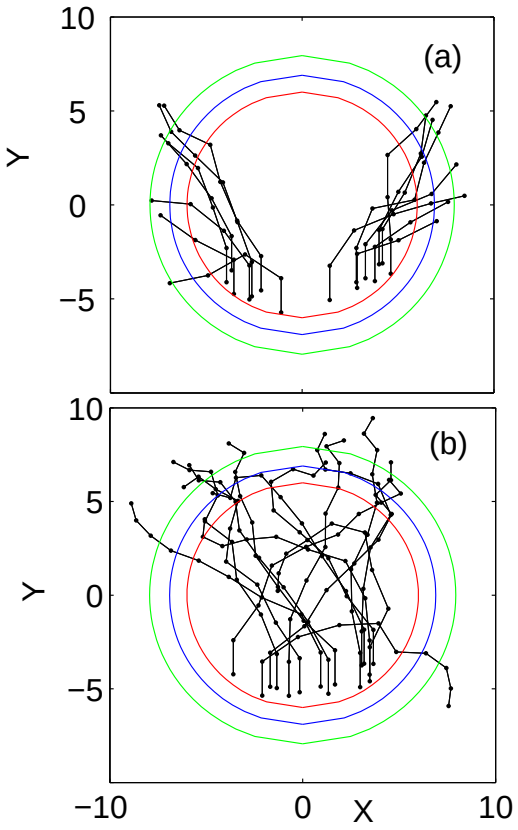

Figure 2.16 — Taken from [99]. Sample tracks of recoil partons that either (a) leave the medium, or (b) are absorbed. The circles represent the cross-sectional area of the medium at three different times as defined in [99],the innermost one being at the initial time, the outermost one at the final time of the expansion.

The gluonic or heavy bound states could lead to a space-like dispersion relation which in turn provides a gluon dielectric constant $\epsilon > 1$.

The authors of [101] have shown that an effective space-like dispersion relation for gluons can lead to Čerenkov-like gluon Bremsstrahlung as a result of complete LPM interference within the forward cone. The characteristic feature is that the cone angle of the produced particles should decrease with increasing p_T as shown in figure 2.18.

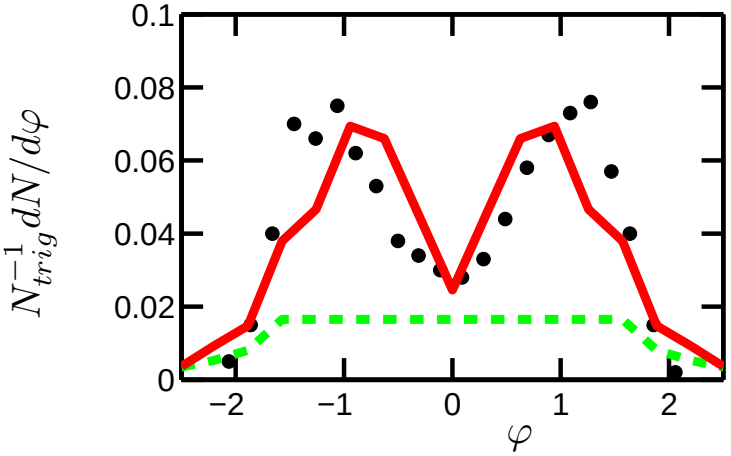

Figure 2.17 — Taken from [99]. Di-hadron distribution on the away side. Data are from [98]. The dashed line is the pedestal calculated from energy deposited in the medium in the last step, and the solid line includes the contribution from the exit tracks that give rise to the deflected jets.

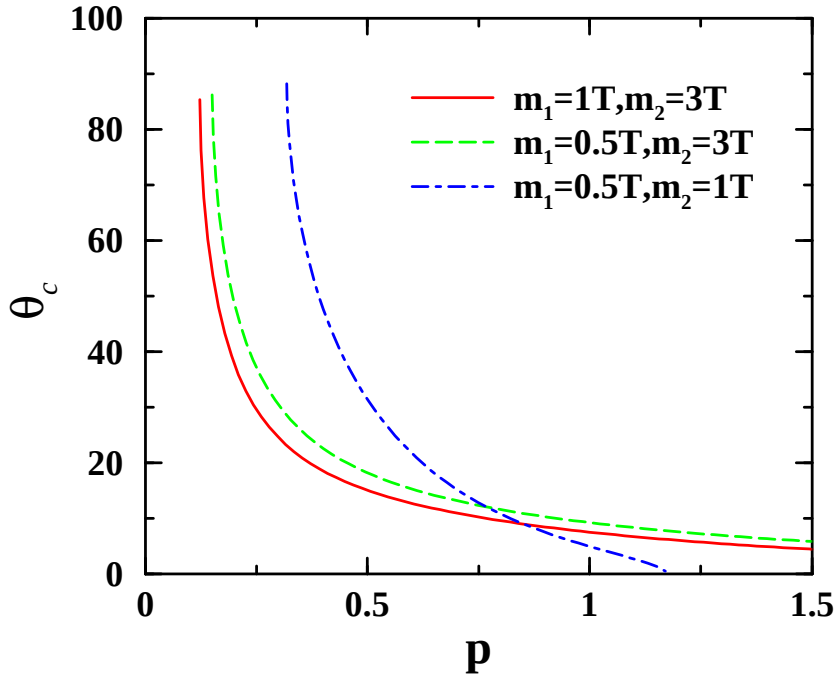

Figure 2.18 — Taken from [101]. Dependence of the Čerenkov angle on momentum of the emitted particle for different parameters for the bound states.

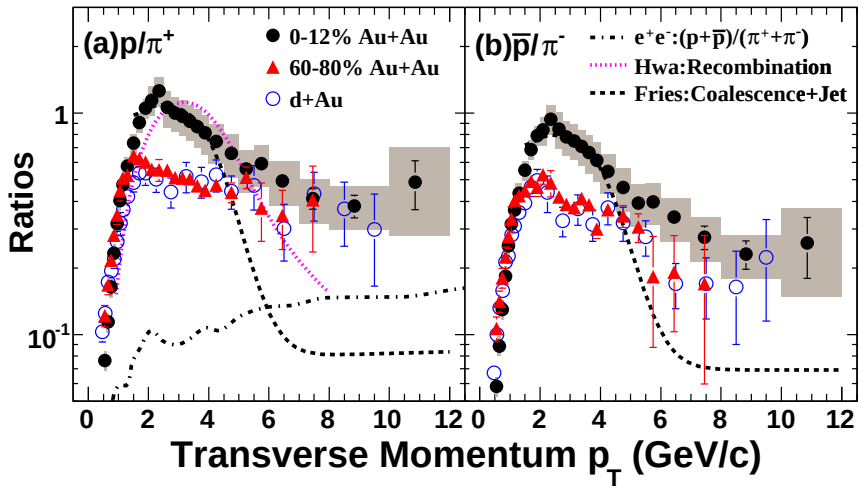

Figure 2.19 — Taken from [106]. The p/π^+ and $\bar{p}/\pi^-$ ratios from d+Au [108,109] and Au+Au collisions at $\sqrt{s_{NN}} = 200$ GeV. The $(p+\bar{p})/(\pi^+ + \pi^-)$ ratio from light quark jets in $e^+ + e^-$ collisions at $\sqrt{s} = 91.2$ GeV are shown as a dotted-dashed line [110]. The shaded boxes represent the systematic uncertainties in the top 12% central Au+Au collisions. The systematic uncertainties for 60-80% Au+Au collisions are similar. The dotted and dashed lines are model calculations in central Au+Au collisions [111,112].

2.6 Recombination and Coalescence Models

2.6.1 Anomalous $\frac{p}{\pi}$ Ratio

The RHIC experiments have measured an anomalously high baryon/meson ratio [33,106,107] for both strange and non-strange particles. In figure 2.19 we show, for example, the results for $\frac{p}{\pi^+}$ in the right hand panel, and $\frac{\bar{p}}{\pi^-}$, in the left hand panel, both as a function of p_T, for d+Au peripheral Au+Au (60-80%), and central Au+Au (0-12%) collisions.

While peripheral Au+Au and d+Au agree well there is a significant enhancement in the ratio in an intermediate p_T-range for both $\frac{p}{\pi^+}$ and $\frac{\bar{p}}{\pi^-}$. Similar results have been observed for the $\frac{\Lambda}{K^0_s}$ [107] and $\frac{\Omega}{\phi}$ [33] ratios.

These results, along with the valence quark scaling observed in figure 2.5, have been used to argue that the there is a collective flow of constituent quarks which is built up before hadronisation [32].

2.6.2 Pure Thermal Particle Production

An underlying spectrum of co-moving thermal quarks is able to produce enhancements in the yields of baryons at intermediate p_T through recombination of those quarks into hadrons.

The enhancements comes about because it more favourable to create a particle with momentum p_T^{ex} from 3 constituents quarks each with $\frac{1}{3}p_T^{ex}$ than with 2 constituents quarks each with $\frac{1}{2}p_T^{ex}$ due to the rapidly falling thermal distribution. In addition, this process is more energetically favourable than fragmentation up to a certain p_T, which depends on the exact details of the particle in question and the particular model being applied, as illustrated in the schematic in figure 2.20.

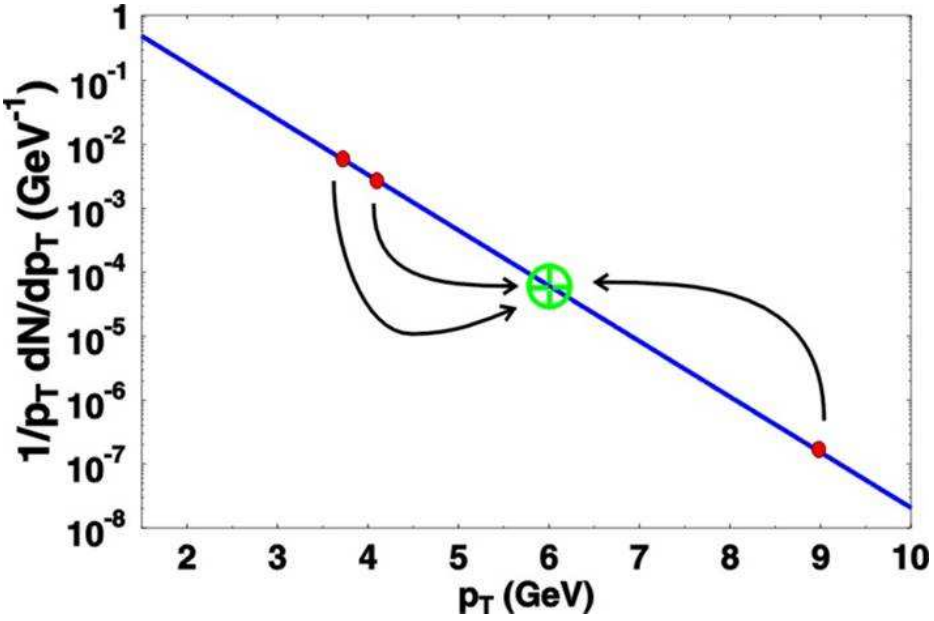

Figure 2.20 — Taken from [113]. A schematic illustrating how it may be more favourable to form a meson at a given p_T from two thermal quarks than the fragmentation of much higher p_T quark.

In figure 2.19 two different recombination models [111,112] are compared to the data presented and both are able to qualitatively describe the enhancement seen in the ratio in the intermediate p_T range. In recombination models a significant fraction of the particles in the region of enhancement are produced by the coalescence of two or three thermal quarks.

In figure 2.21 we present the breakdown of production sources in the recombination model of [114]. Terms consist of combinations of ther-

mal quarks (denoted by "thermal") and quarks from the showering of a hard parton (denoted by "shower") and the various possible combinations. The feature we would like to emphasise is the very significant contribution from purely "thermal" sources, thermal-thermal and thermal-thermal-thermal, in the the left and right panel respectively.

Particles produced from a pure thermal source should not have any associated correlated yield as you would expect with particles within jets. This is particularly relevant as many di-hadron studies have been done with $p_T^{trig.}$ in ranges which overlap significantly, or even entirely, with the region where recombination of pure thermal quarks is the dominant term ($\lesssim 5$ GeV/c).

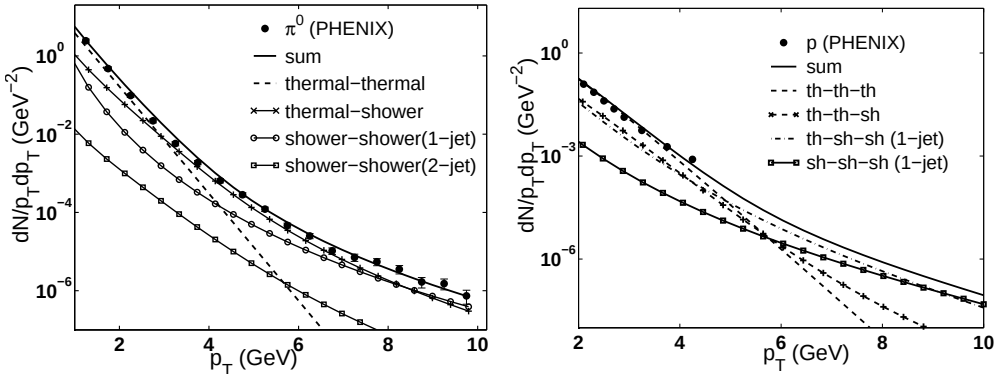

Figure 2.21 — Taken from [114]. (Left Panel) π^0 0-5% central spectra from PHENIX [115] with the contribution breakdown in a particular recombination model [114]. (Right Panel) Proton 0-5% central spectra from PHENIX with the contribution breakdown from the same recombination model.

The $\Delta\eta$-ridge phenomenon mentioned in section 2.5.1 has also been interpreted within a recombination/coalescence framework [116]. The data can be reproduced by assuming a localised increase in temperature in the medium around the near-side jet from in-medium energy loss. This increase in temperature leads to more thermal particle production and is boosted to large $\Delta\eta$ by the strong longitudinal expansion of the system.

2.7 Direct Observation of Away-side Jet

By increasing both the $p_T^{trig.}$ and $p_T^{assoc.}$ thresholds, as done in [117], one can recover the away-side partner fragmenting as in vacuum.

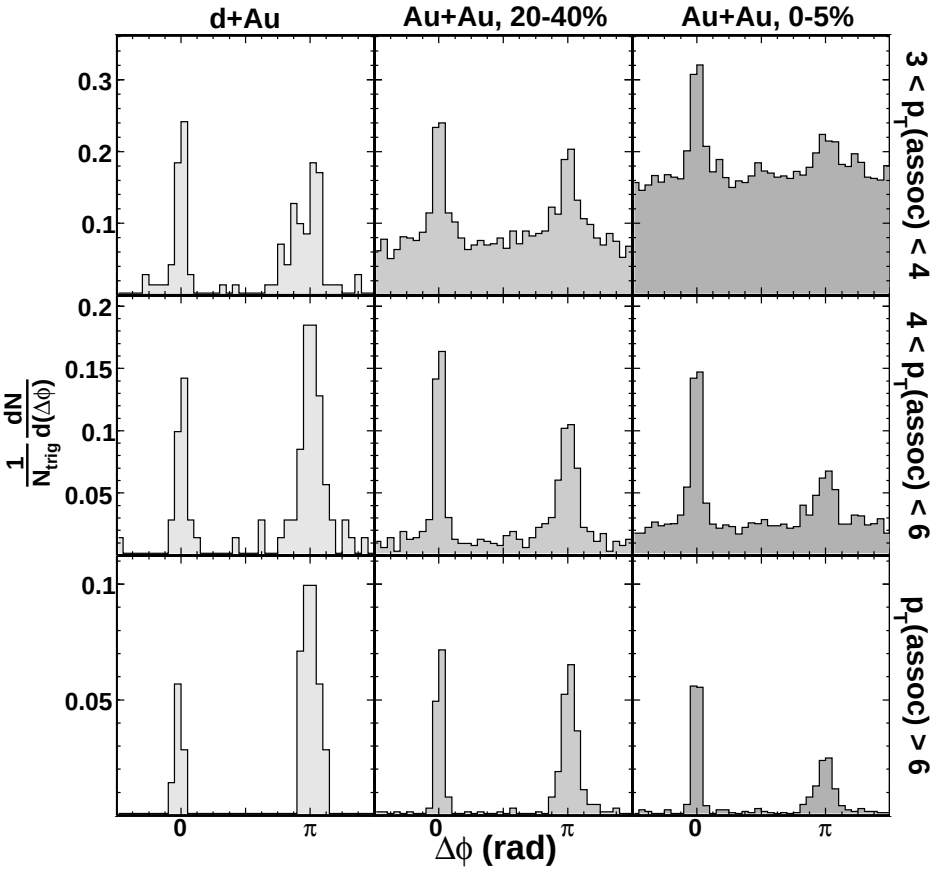

Figure 2.22 — Azimuthal correlation histograms of high p_T charged hadrons for $8 < p_T^{trig.} < 15$ GeV/c, for d+Au 20-40% Au+Au and 0-5% Au+Au events. $p_T^{assoc.}$ increases from top to bottom.

In figure 2.22, taken from [117], the evolution of the raw azimuthally correlated yield with increasing $p_T^{assoc.}$ is shown for 8.0$< p_T^{trig.} <$15.0 GeV/c for d+Au, 20-40% and 0-5% Au+Au data. As $p_T^{assoc.}$ increases the background level decreases and is negligible in the highest bin, 6.0$< p_T^{assoc.} <p_T^{trig.}$. For the central 0-5% results, a narrow away-side jet peak has emerged despite the significant jet quenching at RHIC.

The effect of the medium on di-jet fragmentation can be explored in more detail using the p_T distributions of near- and away-side associated hadrons. In figure 2.23 we show the near- and away-side, right and

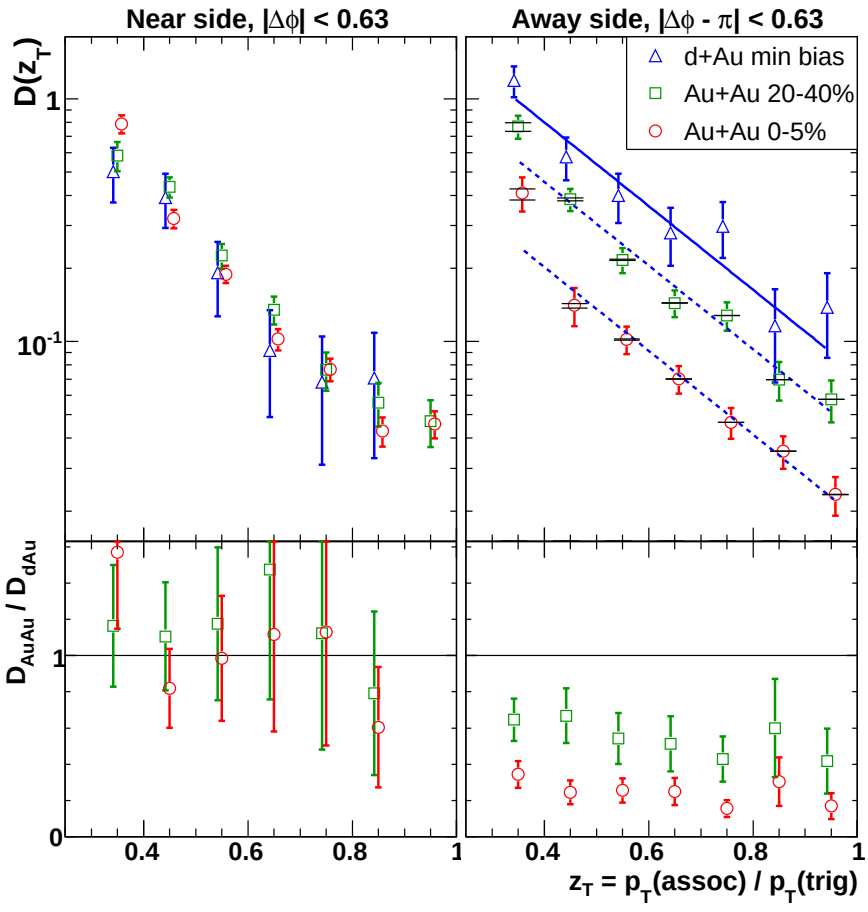

Figure 2.23 — Taken from [117].Upper panels: trigger-normalised charged hadron fragmentation function $D(z_T)$ with $8 < p_T^{trig.} < 15$ GeV/c, for near- (left) and away-side (right) correlations in d+Au and Au+Au collisions at $\sqrt{s_{NN}}$=200 GeV. Dashed and solid lines described in text. Horizontal bars on away-side show systematic uncertainty due to background subtraction. Lower panels: ratio of $D(z_T)$ for Au+Au relative to d+Au. The error bars are statistical in all panels.

left panels respectively, trigger-normalised fragmentation function $D(z_T)$, where $z_T = p_T^{assoc.}/p_T^{trig.}$ [118] for d+Au, 20-40%, and 0-5% Au+Au data.

$D(z_T)$ is measurable without direct knowledge of the parton energy and provides a theoretically calculable alternative to true fragmentation functions. It is not possible to measure jet energies on an event-by-event basis at RHIC as the background multiplicity is too high. The z_T range shown in figure 2.23 corresponds to the $p_T^{assoc.}$ range for which di-jets are observed above background (see figure 2.22). The near-side distributions (left panels) are similar over a broad range of z_T for all three systems, consistent

with fragmentation in vacuum.

It is postulated [117] that the similarity of the near-side fragmentation patterns could arise from small near-side energy loss due to a geometrical bias toward shorter in-medium path lengths ("surface bias"). This interpretation is based on several model calculations [119–122].

Alternatively, this could also result from energy-independent energy loss generating a partonic energy distribution that is suppressed in Au+Au but similar in shape to that in p+p collisions, with the lost energy carried dominantly by low p_T hadrons as shown in [90] .

2.8 Scope of This Work

In this work we will use the most recent Au+Au data-set (Run IV, 2003/4) from STAR, which has much improved statistics over the previous data-set. We will reproduce the "classic" di-hadron results showing the consistency of this analysis with previous published analyses.

Using the improved statistics we will then study the di-hadron distribution shapes and yields, on both near- and away-side, differentially with respect to $p_T^{trig.}$, $p_T^{assoc.}$ and centrality. This has not been done before and no theoretical predictions have yet been made regarding the evolution of the shapes and yields in these systematic studies. We motivate for a phenomenological model for the away-side shape evolution and use it to extract shape information which is comparable to available theory. The azimuthal dependence of $\langle p_T \rangle$ will also be measured.

In addition we will test for the first time whether the $\Delta\eta$-ridge extends to low $p_T^{assoc.}$ and if it can be treated separately from the near-side parton fragmentation products.

The data analysis and results presented in this thesis are solely the work of the author with the guidance and advice of members of the STAR collaboration[1].

[1] http://www.star.bnl.gov/central/collaboration/

Chapter 3

The Collider Facilities

He who breaks a thing to find out what it is, has left the path of wisdom.

J. R. R. Tolkien

The data presented in this thesis are from the Solenoidal Tracker At RHIC (STAR) housed at Brookhaven National Laboratory (BNL) as part of the Relativistic Heavy-Ion Collider (RHIC) facility. Three other experiments have operated as part of the heavy-ion programme, Pioneering High Energy Nuclear Experiment (PHENIX), Broad Range Hadron Magnetic Spectrometers Experiment at RHIC (BRAHMS) and PHOBOS. STAR and PHENIX are large, multi-purpose detectors while BRAHMS and PHOBOS are much smaller systems.

3.1 RHIC

RHIC is an intersecting storage ring (ISR) particle accelerator with the two independent rings being named, by convention, blue and yellow. The choice of two independent rings allows the collision of asymmetric species at RHIC, with some restrictions. The RHIC double storage ring is itself hexagonally shaped and has a circumference of 3834 m. The beam is steered via 1,740 superconducting magnets. Each point where the beams cross is an interaction point. There are six such locations at RHIC, each described by a clock position. Only four of the interaction points are used,

each for one of the aforementioned experiments. The other two collisions points are for possible expansion.

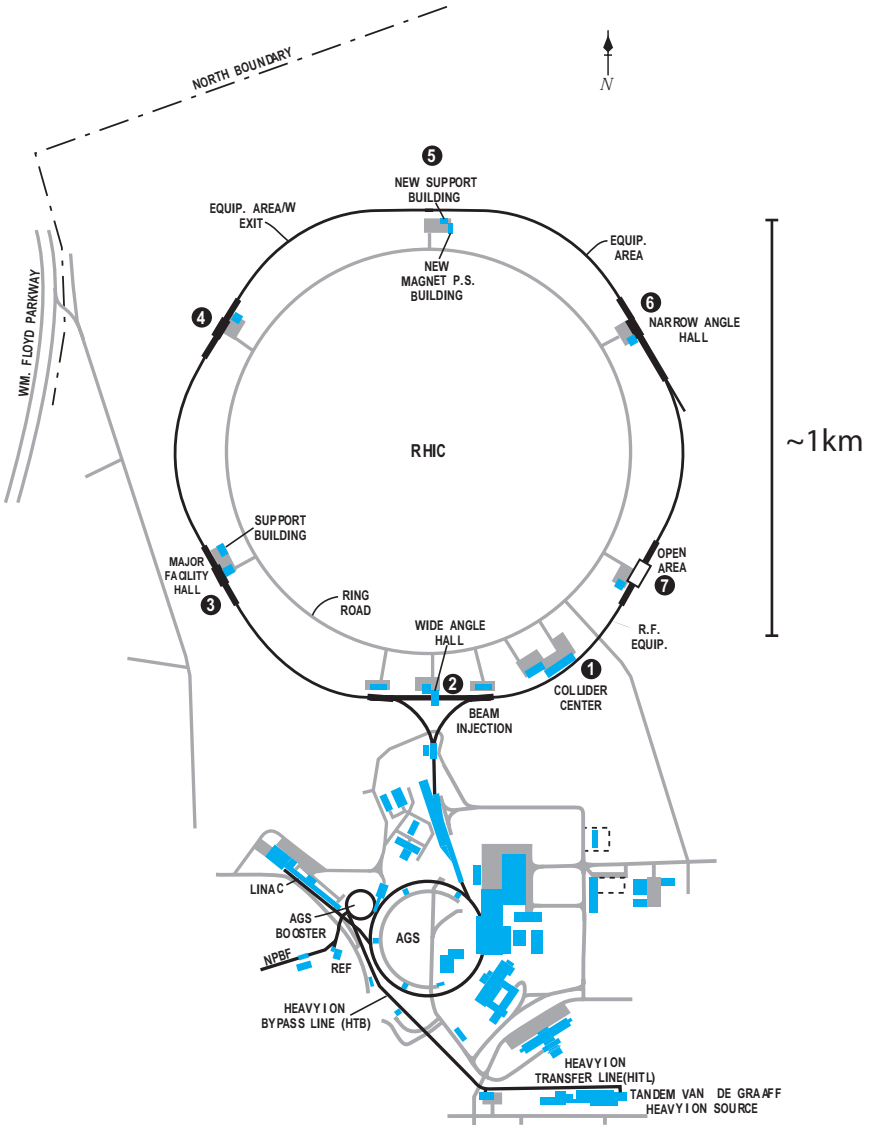

Figure 3.1 — A schematic of the RHIC facility showing the various components used to create and accelerate collision species to the top RHIC energies.

Ions are accelerated through several stages of boosters before reaching the RHIC storage ring. Ions other than protons begin in the Tandem Van de Graaff accelerator, while protons, begin in the 200 MeV linear accelerator (Linac). The second stage is the Booster Synchrotron which injects the accelerated particles into the Alternating Gradient Synchrotron (AGS). From there particles are transferred into the RHIC storage ring via the AGS-To-RHIC Transfer Line (ATR), which enters RHIC at the six o'clock position.

Year	Facility	Location	Species	E_{beam} (E_{CM}) [GeV]
1974 – 1991	BEVALAC	LBNL	Au+Au	2 (2.32)
1994 – present	AGS	BNL	Au+Au	11 (4.86)
1994 – present	SPS	CERN	^{208}Pb+^{208}Pb	158 (17.3)

Table 3.1 — Heaviest beam species and highest collision energies for various heavy-ion accelerators. The facilities are given by a facility acronym and location. Beam energies correspond to the top per nucleon beam energy achievable by the facility.

Start Year	Run	Species	Energies $\sqrt{s_{NN}}$[GeV]
2000	I	Au+Au	56, 130
2001	II	Au+Au	19.6, 200
		p+p	200
2002	III	d+Au	200
		p+p	200
2003	IV	Au+Au	200
		p+p	200
2004	V	^{63}Cu+^{63}Cu	22.4, 62.4, 200
		p+p	200
2005	VI	p+p	200

Table 3.2 — The history of RHIC collision species and energies. p+p runs can further be divided into polarised (longitudinal or transverse) and unpolarised but this is not relevant to this work.

For the specific case of Au nuclei they created using the Pulsed Sputter Ion Source and the Tandem Van de Graaff accelerates them to an energy of approximately 1 MeV per nucleon and stripping foils. This ensures that they enter the Booster Synchrotron with an electric charge Q = +32. They are then accelerated to 95 MeV per nucleon, and stripped to Q = +77 before being injected into the AGS, before they finally reach 8.86 GeV per nucleon and are injected in a Q = +79 state into the RHIC storage ring.

3.1.1 A Brief History

RHIC produced its first collisions on June 12 2000, when Au ions were collided at $\sqrt{s_{NN}} = 56$GeV. Since then RHIC has collided a number of ion species at a variety of energies as a shown in table 3.2. Data were taken by all four of the RHIC experiments up until very recently when PHOBOS was decommissioned in 2006 after the ^{63}Cu+^{63}Cu data was taken.

All the collision systems have been symmetric except for d+Au which is used in place of p+Au because the symmetry in the charge to mass ratio in d+Au is more favourable for the actual practical operation of the collider.

3.2 STAR

The STAR detector was originally designed with the purpose of studying bulk observables placing the requirements of large acceptance and excellent tracking.

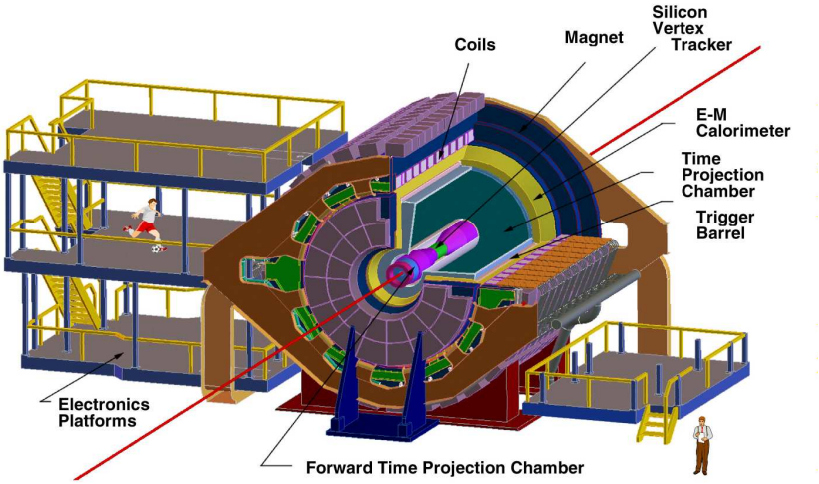

Figure 3.2 — Perspective view of the STAR experimental apparatus showing the location of the detectors sub-systems.

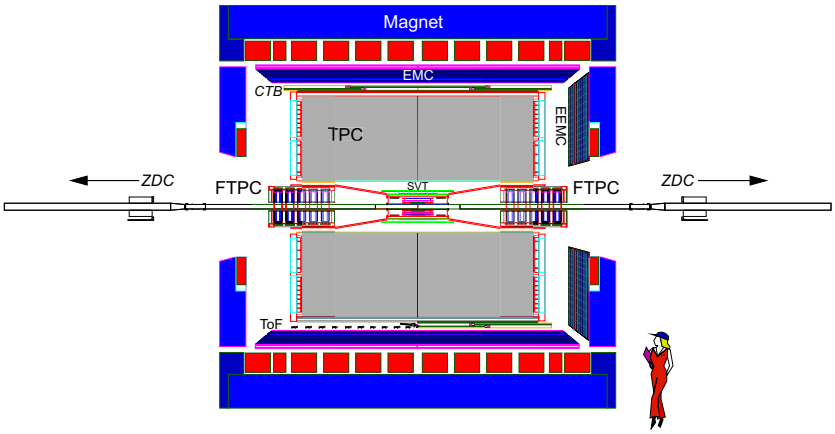

Figure 3.3 — Cross-section of the STAR experimental apparatus showing the location of the detectors sub-systems.

3.2.1 Detector Setup

Magnet

The STAR magnet [123], one of the most important pieces of apparatus, is designed to provide a very uniform field parallel to the beam direction. It is a very large solenoid which houses many of the detector subsystems. Nominally STAR operates with a field strength , B_Z, of 0.5 T, called full-field, which is reversible, called reversed full-field. Configurations of 0.25 T are also used frequently, called half-field. Both full- and reversed full-field results are used in this work.

The uniformity of the magnetic field aids in the tracking of particles. All charged tracks traversing the detectors will follow a helical trajectory to first order. The primary homogeneity specification for the magnetic field was derived by combining the accuracy for high energy electrons (~ 200 μm) with estimates of the accuracy with which the magnetic field could be measured at ~ 0.5 Gauss. These requirements are expressed in the following integrals:

$$|\Im_r| \equiv \left| \int_{z'=210 \text{ cm}}^{z} (B_r/B_{z'})dz' \right| \leq 7.0 \text{ mm} \tag{3.1}$$

$$|\Im_\phi| \equiv \left| \int_{z'=210 \text{ cm}}^{z} (B_\phi/B_{z'})dz' \right| \leq 2.5 \text{ mm} \tag{3.2}$$

Representative mapping results are shown in figure 3.4 which demonstrate a factor of 2 better than specification field quality inside the volume to be occupied by the TPC.

Barrel detectors

STAR is large detector consisting of many concentric layers of detector subsystems at mid-rapidity while including a number of forward detectors. STAR is dominated by a large time project chamber [124] (TPC) which has full azimuthal coverage, $0 < \phi < 2\pi$, and a rapidity coverage of $|\eta| < 1.4$. The TPC provides high precision tracking of charged particles and particle identification.

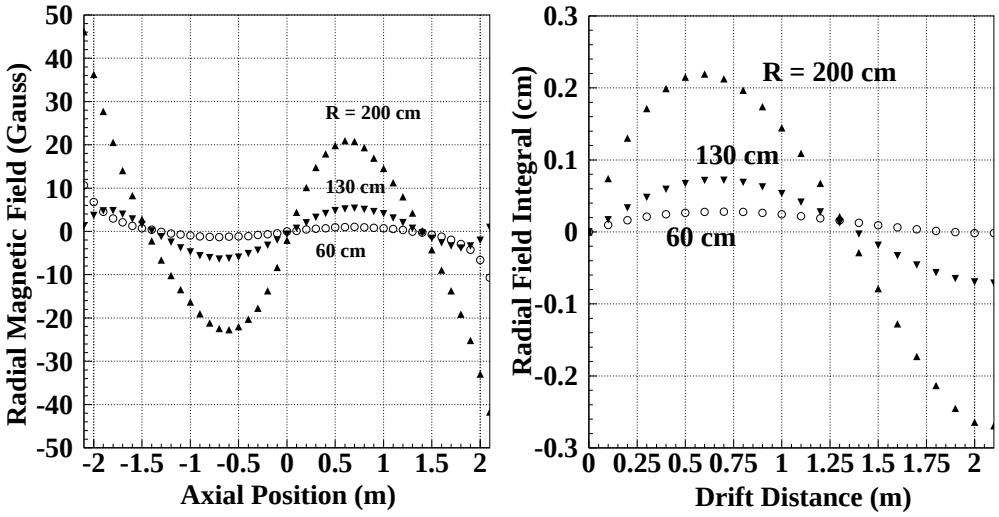

Figure 3.4 — (Left)Measurements of radial component of the STAR magnetic field (Gauss) as a function of axial (z) position for three radii at $\phi = 0^{o}$. The centre of the TPC and the magnet are at $z = 0$. The inner and outer radii of the TPC are 50 cm and 200 cm, respectively. (Right)Values of the field integral ($\Im_r$) of the STAR magnetic field (cm) as a function of drift distance. Representative data are given at three radii in the TPC for $\phi = 0^{o}$ and $z < 0$ (TPC East Half).

Augmenting the tracking of the TPC, and positioned closer to the beam-pipe is a silicon based inner tracking system consisting of two detectors, the silicon vertex tracker [125] (SVT) and the silicon strip detector [126] (SSD). These detectors provide points for tracking purposes which are much closer to the event vertex giving much better pointing resolution when included in tracking. Extremely good pointing resolution can be used to enhance samples of displaced decay vertices which would allow measurements of D or B decays.

The TPC is surrounded by a barrel, lead-sampling, electromagnetic calorimeter [127] (BEMC) for the measurement of electromagnetic particles, primarily photons and electrons. The BEMC consists of 4800 towers which are all projective back to the nominal vertex position. It has full azimuthal coverage and a pseudo-rapidity coverage of $|\eta| < 1$. The BEMC includes a shower maximum detector to further enhance the ability of the detector to discriminate based on shower shape.

Forward detectors

In the forward/backward regions there are two cylindrical TPC detectors [128], the forward TPCs (FTPCS), which have have full azimuthal symmetry and cover a pseudo-rapidity range of $2.5 < |\eta| < 4.0$. To compensate for the high track densities in central Au+Aucollisions at RHIC a radial drift in a low diffusion gas was used as the basic design.

3.2.2 Triggering

The processing of selecting events uses three primary detectors. The data used in this analysis come from the aforementioned TPC and the trigger detectors for event selection.

Zero-Degree Calorimeters

All RHIC experiments are sandwiched between two zero degree calorimeters [129] (ZDCs) which are located at 0^o at 18 m from the nominal interaction point, subtending 2.5 mrad. The ZDCs lie beyond the DX magnets, which are used to bend the beams back into their respective orbits.

When an inelastic heavy-ion collision takes place beam remnant neutrons are emitted at high-energies and small angles (~ 2 mrad) with respect to the beam. It is these beam remnants that the ZDCs are designed to measure.

Central Trigger Barrel

STAR has the addition feature of being able to measure the mid-rapidity, charged-particle multiplicity in real-time and use this for further triggering information. A collection of scintillating tiles surrounded in the TPC (as shown in figure 3.5 called the central trigger barrel [130] (CTB) provides this information. The analogue to digital converter (adc) voltages from the tiles are proportional to the multiplicity of charged particles hitting the tiles. The CTB is a very fast detector (260 ns) allowing for it to be used in conjunction with the ZDC for event selection purposes. The

CTB acceptance in azimuth and pseudo-rapidity is $0 < \phi < 2\pi$ and $|\eta| < 1$ respectively.

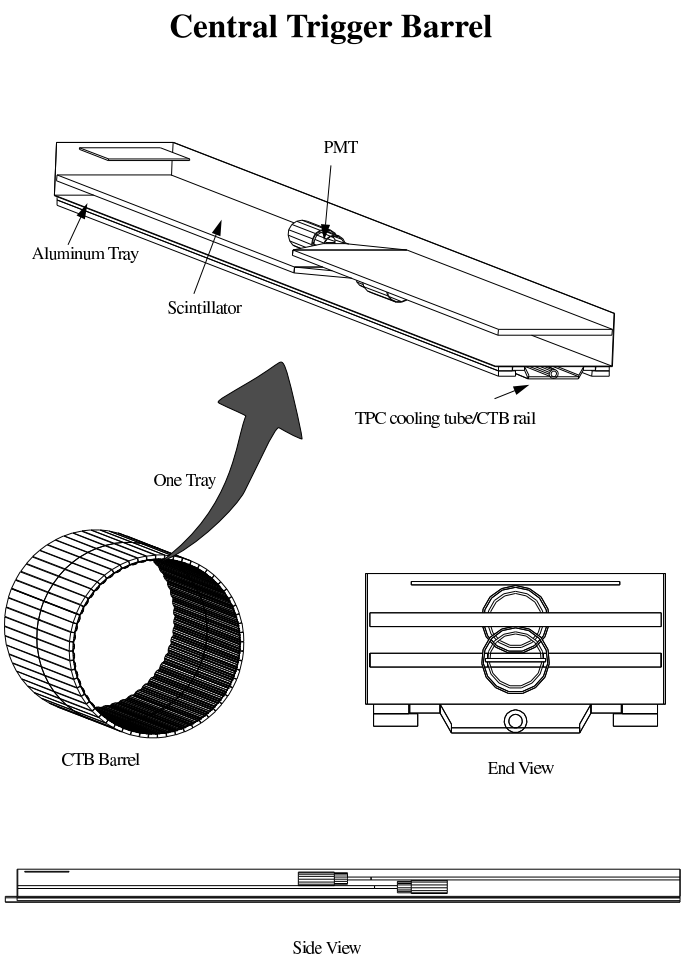

Figure 3.5 — Central trigger barrel schematics, showing the trays and slats.

3.2.3 The TPC

The primary detector used in this analysis is the TPC for the measurement of charged tracks. Its central role warrants a more detailed discussion of the workings of the TPC. The principle behind the TPC is relatively simple, charged particles traverse a large volume of gas leaving a trail ionisation electrons, which is helical in nature due to the uniform magnetic field parallel to the beam direction. By drifting the track in an electric field and

then measuring it it is possible to determine the momentum of the particle and the mean ionisation energy loss.

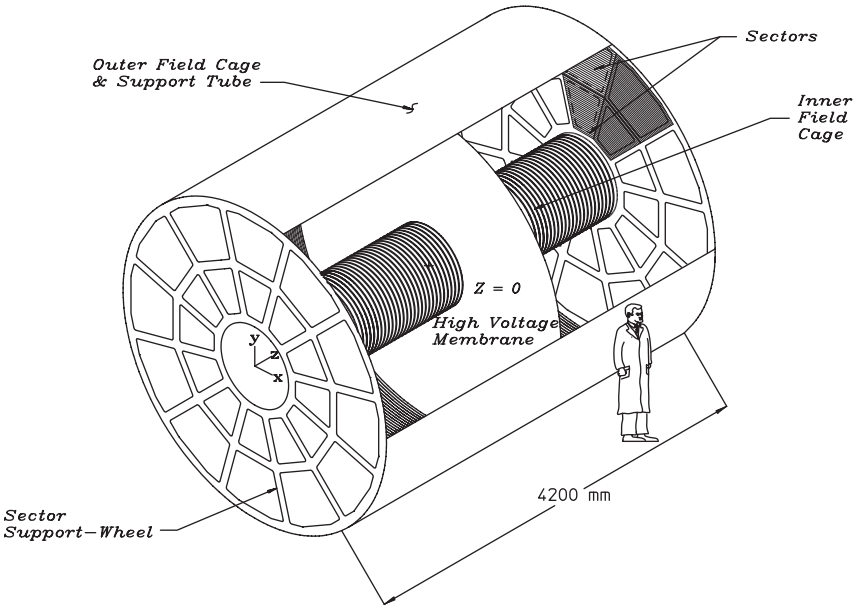

Figure 3.6 — A schematic diagram of the TPC, showing the high voltage central membrane, the inner and outer field cages as well as the TPC sectors.

The TPC (schematic shown in figure 3.6) is 4 m in diameter and 4.2 m long with an inner radius of 50 cm. The outer radius covers a pseudo-rapidity range of $|\eta| < 1$ while the inner radius covers a pseudo-rapidity range of $|\eta| < 2$, giving a useful tracking range of $|\eta| \lesssim 1.5$.

It consists of central high-voltage cathode called the "central membrane" located at $z = 0$ in the laboratory coordinate system which is maintained at 28 kV. The end-caps are maintained at 0 V. The inner and outer radii are imposed by the inner- and outer-field cages. By ensuring the correct boundary conditions on the field cages a uniform electric field is maintained between the central membrane and the end-caps. The uniformity of the electric field is crucial because sub-millimetre track reconstruction is essential and ionisation tracks may drift as far as 2.1 m.

The volume of the TPC is filled with P10 (10% methane, 90% argon) at 2 mbar above atmospheric pressure to minimise any leakage of gasses like O_2 into the TPC. The primary attribute of P10 is a fast drift velocity which

peaks at low electric field (~ 5.45cm/μs in STAR). The drift velocity, when near its peak values, is less sensitive to small variations in temperature and pressure.

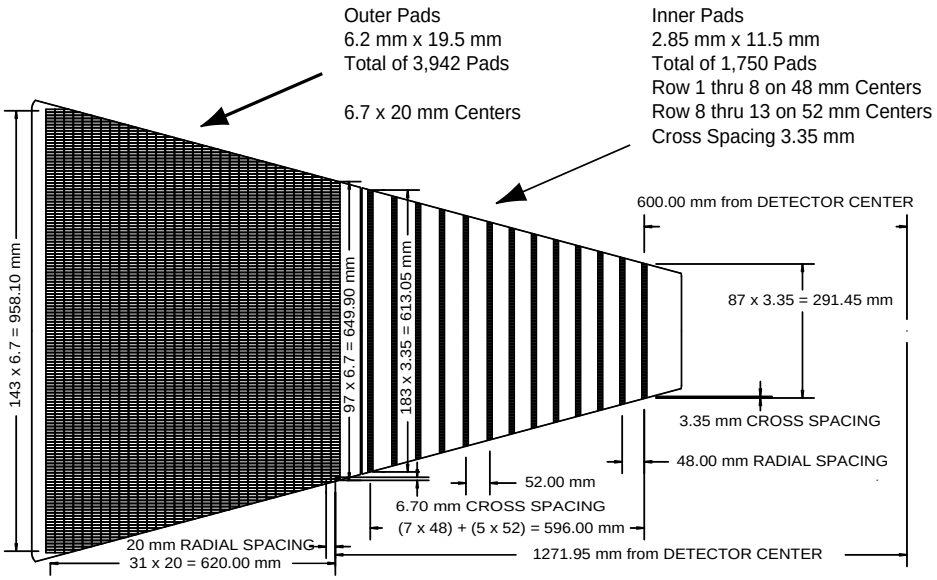

Figure 3.7 — A schematic of one sector of anode pad planes.

When a central collision takes places thousands of curving charged particles will almost instantaneously leave ionisation tracks inside the TPC. The electrons drift through the gas towards the nearest end-cap. These consist of 12 sectors on each side, each having an inner and outer sub-sector as shown in figure 3.7. There is a 3 mm gap between sectors. The sectors contain the readout pads, consisting of multi-wire proportionality chambers (MWPC) with pad readout. The chambers consist of four parts, a pad plane and 3 wire planes as shown in figure 3.8. The amplification/readout layer is composed of 20 μm wires with the pad plane on one side and the ground wire plane on the other. The final layer is a gating grid which is used to maintain the correct boundary conditions on the electric field in the TPC. The orientation of the wires is set to be perpendicular to high-p_T tracks, very stiff tracks, to give the best possible resolution as the position resolution is best along the anode wire direction.

The pad widths are chosen so that the charge induced from the avalanche point is shared between 3 pads at most. A Gaussian fit or weighted mean is then used to determine the position of the avalanche. This resolution is typically better than 20% of the narrow pad dimension. The TPC has a

total of 45 pad-rows in every sector.

The gas gain is controlled by the anode wire voltage and is set independently for the inner and outer sectors to generate a signal to noise ratio of 20:1 for pads intercepting the centre of tracks that drifted the full half-length of the TPC.

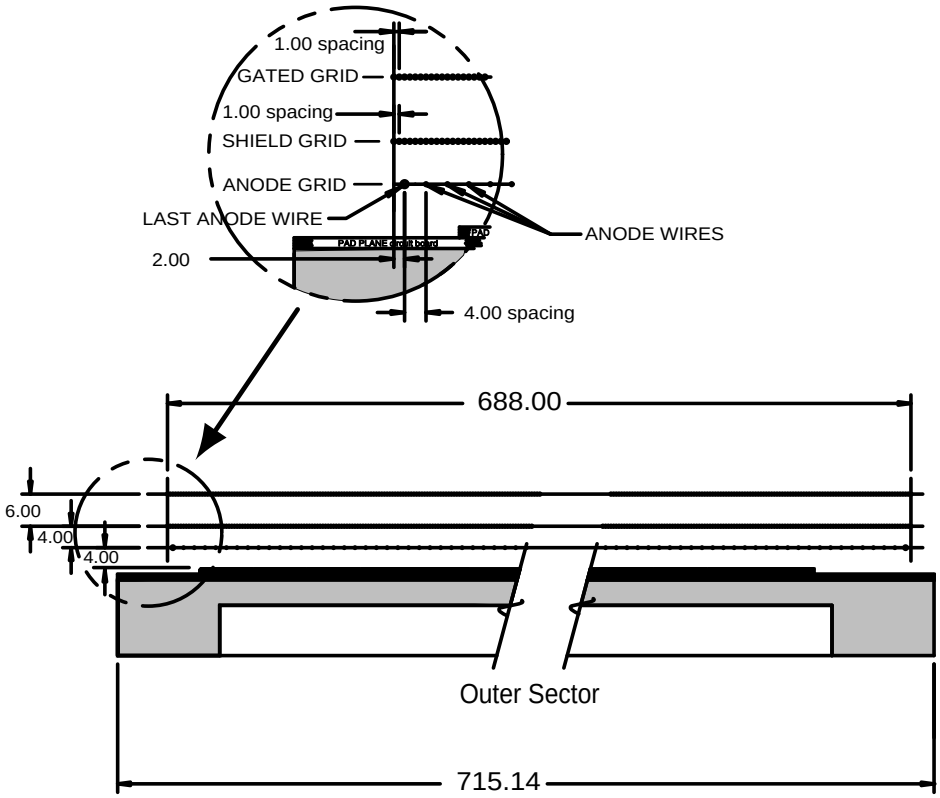

Figure 3.8 — Pad plane cutaway showing structure of the MWPC readout.

The outer sub-sector has continuous pad coverage to optimise dE/dx resolution while the inner sub-sector (the region of highest track density) is optimised for good two-hit resolution with smaller pads (detailed discussion of optimisations can be found in [124, 131]).

Given the time of the collision, the read-out time and location, it is possible to reconstruct the 3D location of any ionisation event in the TPC. This allows the full 3D reconstruction of tracks in the TPC.

Tracking in the TPC

There is effectively a continuous dumping of information into the TPC. The ADC signals from the TPC pad rows are thus grouped into time intervals and then for a given time interval, clustering and tracking is performed. Contiguous regions of ADC signal are clustered and the peak position found, i.e. the position of a hit (ionisation event). These clusters can contain more than one peak and can be deconvoluted into two hits. This happens when two tracks are not spatially distinct at some point on their trajectories.

Once clusters have been turned into hits a 3D volume of distinct hits exists as shown in figure 3.9. From these points tracks need to be reconstructed. A central collision may contain $\sim 10^5$ hits, making tracking a non-trivial task.

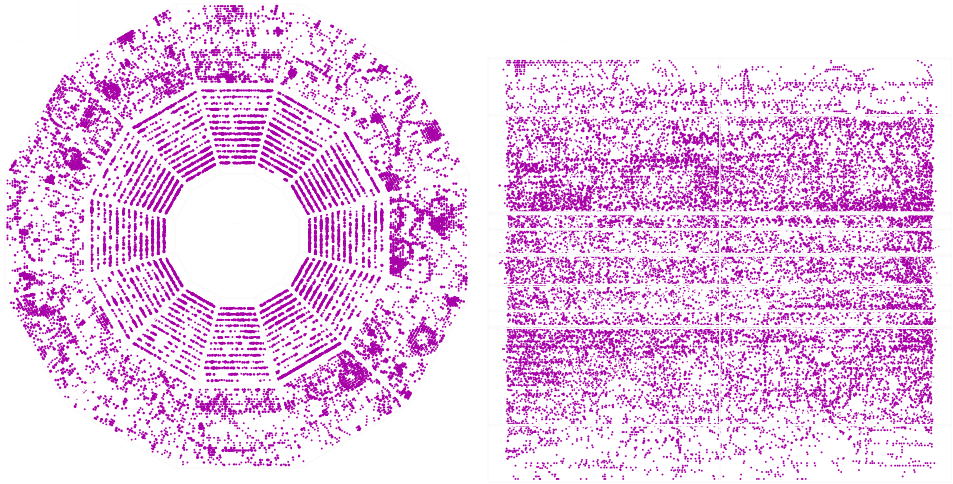

Figure 3.9 — The projection (left) of all the hits in the TPC volume onto a single TPC pad plane. The lateral view (right) of the same hit volume.

Track finding begins in the outermost pad row and proceeds inwards, constructing tracks in a piecemeal fashion. Possible, reasonable permutations of hits in the outer 3 pad rows are constructed. Then these segments are projected back towards the next outermost pad row. If a hit is found within some tolerance it is added to the segment and a new projection is made to the next pad row. The procedure iterates until the innermost pad row is hit or the segment is discarded.

Segments are projected outwards or inwards to investigate the possible merging of segments. This occurs mostly for lower p_T tracks while high-p_T tracks typically consist of one segment. Once this has been done track fitting begins. The trajectory of a charged particle in a uniform magnetic field is well described by a helix. Initially the helix parameters for a given track are determined piecemeal. A circle is fitted to the xy-plane projection of the track and a straight line to the sz-plane projection, where s is the length of the track. A track must have at least 5 hits (points) to determine the 5 helix parameters in a meaningful way.

These results are then passed through a Kalman filter [132] to allow reconstruction of tracks taking into account multiple coulomb scatterings. Detailed Monte-Carlo studies for STAR can be found in [133]. The filtering is done in two stages, firstly, a refit accounting for the multiple coulomb scattering is implemented and then refit to the track is performed. During the refit outlier points can be dropped. This process is repeated twice with more stringent outlier cuts in the second fit.

At this point global tracks, tracks which do not include the event vertex, have been constructed. Global tracks which are with 3 cm of nominal interaction point in the the xy plane are used to construct an initial event vertex. An iterative procedure (3 iterations) of more stringent track cuts and recalculation of the vertex using a least squares approach leads to the final vertex position. At this point all tracks whose global tracks have a distance-of-closest approach (DCA) of less than 3 cm to the vertex are used to create primary tracks.

To do this the global tracks are constrained to go through the event vertex and the track parameters are refit. This may change the track parameters significantly, in some cases the imposition of the event vertex will not allow the track fitting to converge. For this reason every primary track will have an associated global track but the converse is not necessarily true.

From the direction of curvature we are able to determine the charge of the track, from the radius of the curvature it is possible to determine the track momentum and from the mean energy loss of the track it is sometimes possible to determine the particle type, although this depends strongly on the kinematic range being considered (see section 3.2.3).

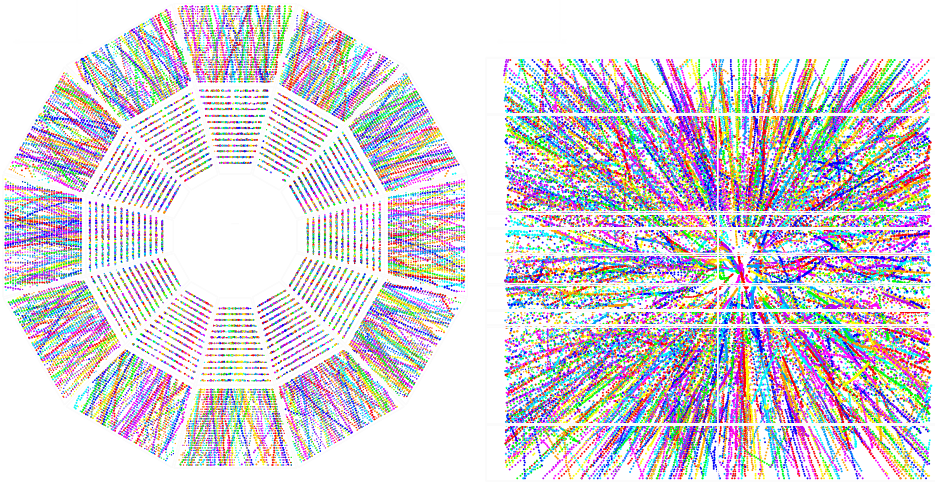

Figure 3.10 — The same data as shown in figure 3.9 but now with the reconstructed tracks superimposed.

Ionisation in the TPC

The magnitude of the energy loss of the charges particles as they traverse the TPC gas volume is characterised by the well known Bethe-Bloch formula given here:

$$-\frac{dE}{dx} = \frac{4\pi}{m_e c^2} \cdot \frac{nz^2}{\beta^2} \cdot \left(\frac{e^2}{4\pi\epsilon_0}\right)^2 \cdot \left[\ln\left(\frac{2m_e c^2\beta^2}{I \cdot (1-\beta^2)}\right) - \beta^2\right], \qquad (3.3)$$

where $\beta = \frac{v}{c}$, z e $I = 16eV \cdot Z^{0.9}$

The mean energy deposited depends on the momentum of the particle, the charge it carries, its mass and the target material. This means that in some kinematic ranges it is possible to determine the type of particle based on the mean energy deposited in the hits that make up the track. A standard plot from STAR is shown in figure 3.11 where the energy loss versus reconstructed p_T has been plotted for all the tracks in a large number of events. The points cluster around the characteristic bands for the various particles whose ideal dE/dx curves have been superimposed.

Note that PID on a track-by-track basis is only possible at low momentum. At higher momenta it is possible to deconvolute the tracks into samples of a selected purity but this also reduces significantly reduces the statistics for correlation studies.

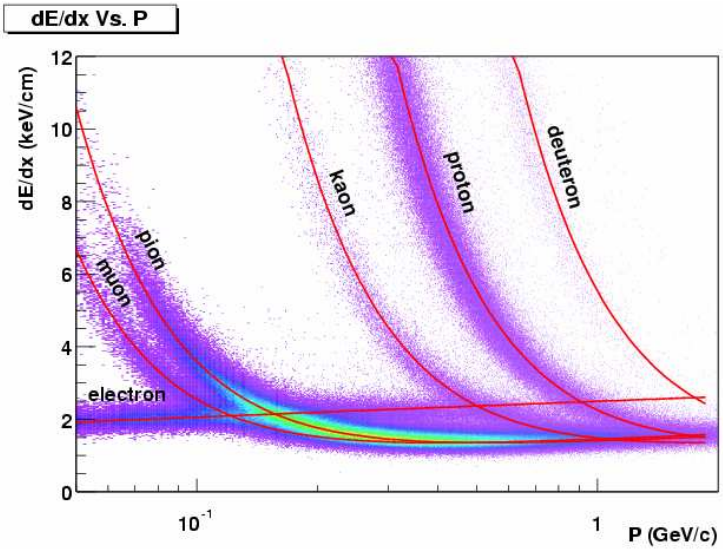

Figure 3.11 — $\frac{dE}{dx}$ bands as measured in the TPC with the overlaid predicted curves for the various particles species.

In this analysis we will only study charged hadron distributions.

3.3 Data Selection

The process of data selection take place both on-line (real-time) through trigger selection and then offline in detailed event selection and quality cuts.

3.3.1 Trigger Selection

The selection of which events to record is known as triggering. Triggering is a process involving information from fast detectors to make a decision that an interesting collision took place, the simplest selection criteria called a minimum bias selection.

There two primary reasons for triggering, the first being for the practical reason of reducing data rate and the other to select rare events. The

practical considerations are the beam bunch crossing frequency versus the readout rate of the TPC. It is not possible to read out every event that takes place in the TPC and so triggering on a set of loose criteria ensures that almost the full hadronic cross-section is sampled. For rare processes very tight and specific cuts can be implemented to ensure that a reasonable selection of these are sampled. By allocating a different time to each trigger in a given data taking period different trigger samples can be collected. It is possible for an event to satisfy the criteria for different triggers and so an event can be labelled as belonging to multiple trigger classes.

Au+Au Triggers

The correlation between the ZDC and CTB detector outputs is shown in the right panel of figure 3.12. The trajectory marked by collisions with increasing centrality moves up along the ZDC axis and then out along the CTB axis while moving down the ZDC axis again. This is because for very peripheral collisions both detectors register small signals, as the centrality increases more and more neutrons reach the calorimeters and the ZDC signal increases. The multiplicity measured in the CTB also increases. At some centrality, the collisions overlap sufficiently to decrease the number of neutrons hitting the ZDC while the CTB multiplicity continues to increase. The characteristic shape is often referred to as the ”boomerang” shape.

By placing cuts in the ZDC-CTB correlation one can select events of a certain centrality.

The minimum bias trigger is a coincidence between the two ZDCs with each ZDC having a summed analog output corresponding to at least 40% of a single neutron energy. The virtue of a minimum bias datasample is that the number of events in each any equally sized selection of the total hadronic cross-section is the same modulo statistical fluctuations. The disadvantage of the minimum bias data-set is that extremely large volumes of data need to be recorded for the analysis of rare events.

To enhance the sample of rare processes, which typically scale with the number of binary collisions and therefore will be more common in central collisions, an on-line trigger is used to select central collisions. The thresh-

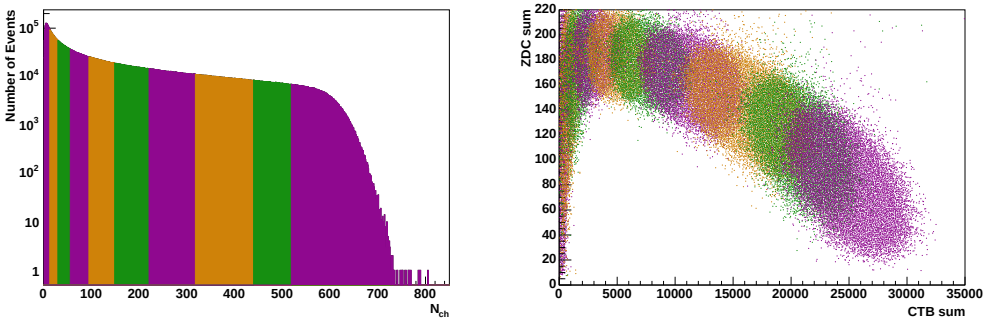

Figure 3.12 — (Left) The uncorrected reference multiplicity (N_{ch} as measured in the TPC) for a subset of the minimum bias data-sample. The divisions show the centrality selections in percentages of the cross-section sampled as a function of impact parameter; 80-100%, 70-80%, 60-70%, 50-60%, 40-50%, 30-40%, 20-30%, 10-20%, 5-10%, and 0-5%. (Right) The ZDC sum vs CTB sum for the same event sample showing the regions of the correlation space corresponding to the reference multiplicity cuts defining the centrality.

olds (see table 3.3) can be seen to select the more central collisions if one considers the minimum bias plots in figure 3.12.

The central triggered data corresponds to the most central 12% of the total hadronic cross-section.

d+Au Triggers

In d+Au collisions the asymmetry of the collision system requires different threshold settings for the trigger detectors to the East and West of the nominal collision vertex. The settings are designed to measure a single neutron from outgoing deuteron remnants. The values are given in table 3.4.

3.3.2 Event Selection

When processing data events the first check to be implemented is to check that the event satisfies the trigger word of interest and therefore the event characteristics of interest. Although an event can satisfy multiple trigger word selections it is ensured that no events fall into more than one selection in this analysis.

For every event to be considered the first step is to identify events in which

Au+Au Minimum Bias (15007)	
ZDC East	>5
ZDC West	>5
ZDC vertex	$\|z\| < 30$cm
CTB sum	> 75
Au+Au Central (15105)	
ZDC West	> 5
ZDC East	> 5
ZDC sum	$<= 131$
CTB sum	> 3500
BBC vertex	$\|z\| < 15$cm

Table 3.3 — Au+Au trigger thresholds used for the various triggers selections used in the studies presented here. Trigger words used in data analysis in brackets.

d+Au Minimum Bias (2001)	
ZDC East	> 5
ZDC East *tac*	> 20 and < 225
B&&Y	TRUE
d+Au Minimum Bias (2003)	
ZDC East	> 5
ZDC East *tac*	> 20 and < 225

Table 3.4 — d+Au trigger thresholds used for the various triggers selections used in the studies presented here. Trigger words used in data analysis in brackets.

System	Range
d+Au	$\|z\| < 50$ cm
Au+Au	$\|z\| < 25$ cm

Table 3.5 — The system-dependent vertex cuts used for this analysis.

Track Cut	Values
DCA_{global}	$<= 1$ cm
$N_{fitpoints}$	$>= 20$
$\frac{N_{fitpoints}}{N_{possible fitpoints}}$	> 0.52
η	$-1 < \eta < 1$

Table 3.6 — Track quality cuts used in this analysis.

a proper vertex has been reconstructed and where that vertex lies within a prescribed range of the nominal vertex position. This reduces backgrounds, biases and reconstruction inefficiencies. Should an event satisfy the vertex criteria listed in table 3.5 then data analysis can begin.

3.3.3 Track Selection

Each event contains many global and primary tracks reconstructed by the tracking algorithm. Not all of these are good tracks or come from the vertex. To ensure that only "good" tracks are analysed certain quality control cuts are implemented in the offline analysis. The cuts discussed here are all implemented in this analysis with the values presented in table 3.6. Any good tracks accidentally excluded by these cuts will be compensated for because the same cuts will be imposed in the efficiency analysis.

Only primary tracks will be used in this analysis and to ensure that the tracks are good primary tracks a DCA cut is implemented based on the DCA of the global track from which the primary track in question was constructed.

To ensure that the track is a quality reconstruction a minimum number of hit points is required from which the track parameters have been determined. Furthermore, this minimum number of hit points must be the majority of the possible points (which is 45, the number of TPC pad rows) that could have been used for the track reconstruction. These methods are

standard in STAR and have been discussed in detail in [17, 134, 135].

An additional constraint that tracks fall with the pseudo-rapidity range of the outer TPC barrel is imposed to ensure that there is sufficient path length in the TPC for the possibility of good reconstruction of the track.

3.4 Tracking Efficiency

To accurately determine the particle production in a collision it is necessary to correct for detector inefficiencies and acceptance gaps. This involves a full characterisation of the detector efficiency and acceptance as a function of momentum, azimuth and pseudo-rapidity.

Tracks which do not pass through the active volume are lost completely from the reconstruction chain but must be corrected for to produce accurate physics results for any measurement. Those that penetrate an active detector volume may still not be correctly reconstructed and there are many reasons why inefficiencies in reconstruction may occur. These include, but are not restricted to, dead channels in the detector, space-charge distortions, merging of tracks, fake tracks and algorithm inefficiencies.

The best way to fully characterise all of these effects simultaneously is to use a known input signal in a real event environment. To do this we generate a known physics signal covering in the full kinematic range of interest and with sufficient statistics and embed it in a real event. Then the full analysis chain is implemented to see if it is possible to reconstruct the input signal. The efficiency and acceptance correction is defined as:

$$\epsilon = \frac{Signal_{Reco.}(p_T, \eta, \phi)}{Signal_{Input}(p_T, \eta, \phi)} \tag{3.4}$$

3.4.1 Monte-Carlo Tracks

The interactions of the pure signal tracks with the detector material is simulated using the software package GEANT [136]. GEANT is essentially a vast library of cross-sections for for various types of particles and their interactions in various materials. It also allows one to construct 3D models of different material configurations. By constructing a virtual detector in

GEANT where the detector is broken down into many small elements by material type and location in 3D space it is possible to model the trajectory and energy loss of any type of particle for any kinematics within STAR.

An input particle distribution is Monte-Carlo sampled and each particle simulated as it passes through the STAR environment taking into account all the material, multiple scatterings, energy loss, conversions and particle decay. The final output is the complete information of the particle's trajectory and interactions in the active detector volumes. The energy loss in the TPC volume is extracted from this information.

An additional software package exists which is used to simulate the TPC response to the passing of an ionising track. The TPC Response Simulator (for detailed descriptions see [135, 137]) (TRS) which simulated the propagation of the charge through the TPC gas as well as all the details of the deposition of the charge on the pad planes and their response up to the point of producing ADC output.

3.4.2 Embedding and Matching

These signals are then added to those from a real event and the modified event is processed using the standard analysis chain from STAR. Once the full analysis is done the reconstructed hits and tracks are associated with those from the Monte-Carlo particles.

For hits the distance between the reconstructed hits and the input hits is used as the metric to determine if the input hit was reconstructed. Once this is done the Monte-Carlo tracks can be associated with reconstructed global tracks by requiring that the MC track is associated with a minimum number of hits which are included in the reconstructed track fit. From this MC track to global association there is also the possible association of the MC track to the primary track associated with the global track.

This is simple in the case where the MC tracks are all tracks which should be associated with primary tracks i.e. primary tracks were simulated. In the case where a neutral particle is being studied and the charged decay daughters are what will be reconstructed in actual data these tracks will be matched to global tracks but the efficiency is contingent on finding both daughters with sufficiently correct kinematics to reconstruct the parent.

Once the association of MC tracks and real track is complete, all quality cuts are imposed on the real tracks to see which of them would be reconstructed in the analysis. Only those passing all analysis cuts and manipulations are valid reconstructed tracks which can be used for determining the efficiency.

3.5 Computing

All analysis of heavy-ion data has become very computation intensive. The process of analysing extremely large raw data-sets and performing corrections for numerous detailed detector effects and implementing iterative tracking algorithms requires large computational resources. These steps must precede even the simplest data analysis.

Analysis techniques have also progressed with time and many analyses, including the one presented here, now involve multiple particle correlations and mixed event techniques which, when implemented on the large data-sets now recorded in STAR, also require significant computing resources. These include both CPU hours as well as minimum machine specifications, most notably RAM requirements can become significant.

It is appropriate to mention the two computing facilities that were used to complete this analysis, the RHIC Computing Facility (RCF) at BNL and the Parallel Distributed Systems Facility (PDSF) at LBNL.

3.5.1 RHIC Computing Facility

RCF is accessible via 3 gateway computers from which access to one of the 10 interactive nodes can be obtained. The farm itself consists of over 800+ computing nodes but is dedicated to all of the RHIC experiments. The LSF batch system is implemented at RCF as well as newly commissioned Condor system.

3.5.2 Parallel Distributed Systems Facility

PDSF consists of 8 interactive nodes which are accessible from the outside the facility. These act as the gateway through which the facility can be used. There are 275 computing nodes in the cluster each of which is a dual CPU machine which are accessible through the Sun GRID engine as a batch system.

Chapter 4

Analysis Method

It does not do to leave a live dragon out of your calculations, if you live near him.

J. R. R. Tolkien

Here we describe the method used in this work for constructing di-hadron distributions from the available data. The same method is used for Au+Au and d+Au data-sets. The descriptions here presume certain features which will only be demonstrated in the results chapter 5.

The analysis consists of distinct parts, some of which are done before actual processing of the data and some after. In the following sections the various steps are presented in chronological order.

In the actual analysis distribution histograms are constructed for the signal and mixed event distributions. These histograms must be filled with the correct efficiency correction weighting requiring that we determine the efficiency before doing the analysis. Once the analysis of the raw data is complete the mixed event distributions are used to correct for two-particle acceptance effects. Finally the uncorrelated background can be subtracted from the distributions using known v_2 results.

4.1 Single Particle Efficiency and Acceptance

Any detector suffers from inefficiencies and gaps in coverage and this must be accounted for in the production of final results. The procedure for

determining the details of the efficiency and acceptance were described in section 3.4 and we only present results here. The efficiency is determined before analysing the data so that histograms can be filled with the correct weight during data analysis.

We determine the efficiency from charged pion embedding. The efficiency and acceptance depend on both p_T and η. We do not separate the geometrical acceptance and tracking efficiency. In figure 4.1 we show an example of the detection and reconstruction efficiency as a function of η and p_T for 0-5% central Au+Au collisions.

We see that the efficiency at low p_T is very low and rises to an approximate plateau at ~ 2.0 GeV/c. A number of factors contribute to this, including: strong bending in the magnetic field, crossing multiple sector boundaries, high hit densities close to the interaction point where soft tracks may merge with many other tracks due to their curvature and momenta too low to enter the TPC. To make use of these results when working with data we choose to parametrise the efficiency using

$$\begin{aligned}\epsilon(p_T,\eta) &= C_0 + C_1\eta^2 + C_2\eta^4 + C_3\eta^6 + C_4\eta^8 + C_5 e^{(C_6 p_T)} + C_7 p_T + C_8 p_T^2 \\ &\quad + C_9 e^{(-\frac{(|\eta|-C_{10})^2}{C_{11}} - \frac{(|p_T|-C_{12})^2}{C_{13}})}. \end{aligned} \tag{4.1}$$

This functional form is determined purely to reproduce the shape of the efficiency. The right panel of figure 4.1 shows the difference between the efficiency (left panel) and the parametrisation for this case. We see only small statistical deviations from the parametrisation.

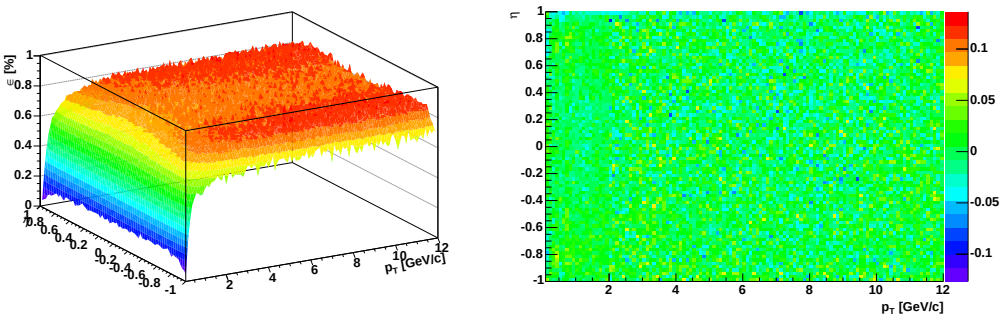

Figure 4.1 — (Left panel) An example plot of the efficiency as a function of η and p_T for 0-5% central collisions. (Right panel) The difference between the parametrisation and the measured efficiency.

In table 4.1 we present the constants obtained from fitting equation 4.1 to the various sets of results. This is done separately for the Au+Au results in centrality bins 0-5%, 5-10%, 10-20%, 20-30%, 30-40%, 40-60%, and 60-80% as well as for the d+Au minimum bias results. In cases where terms aren't required (~ 0) they have been neglected and this is shown by the dash (-) in the table.

When combining centrality bins the efficiency used for a particular event will be the one corresponding to the centrality class the event would be classified from those listed in table 4.1.

The track quality cuts that were used were chosen to select a very high quality track sample, as has been shown and discussed in detail in [134]. These are standard cuts for high-p_T focussed analyses in STAR. The cuts suppress splitting of a single track into multiple tracks and enforce a minimum number of hits to ensure good momentum resolution.

4.2 Algorithm for Constructing Raw Di-hadron Correlations

We use the same algorithm for processing all data.

After the initialisation The first step is to identify the following global characteristics of the event:

- centrality and
- vertex location.

If these satisfy the conditions for the situation being analysed then the tracks for the event are processed. The event is classified according to a vertex bin, 10 bins are defined, all of equal size from the minimum vertex accepted to the maximum. This ensures that events are never mixed with other events that have a significantly different vertex location.

The primary procedure involves two loops over the primary tracks of the event, the first step is to identify the trigger particles, this is done by looping over all the primary tracks and determining if a track has a $p_T > 2.5$

Constant	0-5%	5-10%	10-20%	20-30%
C_0	0.632	0.652	0.699	0.753
C_1	0.118	0.0761	0.0348	0.0386
C_2	-0.290	-0.0784	-0.00819	0.0746
C_3	0.523	0.0394	0.113	-0.159
C_4	-0.570	-0.247	-0.357	-0.175
C_5	-1.39	-2.05	-1.63	-1.31
C_6	-6.73	-8.96	-7.27	-5.75
C_7	0.0588	0.0603	0.0436	0.0223
C_8	-0.00687	-0.00697	-0.00453	-0.00168
C_9	0.111	-0.0435	0.250	0.00440
C_{10}	0.295	0.131	0.309	0.0647
C_{11}	0.145	0.000531	0.133	0.00756
C_{12}	0.296	0.744	0.295	0.476
C_{13}	0.00291	0.00577	0.00193	2.30
Constant	30-40%	40-60%	60-80%	d+Au
C_0	0.740	0.760	0.733	0.905
C_1	-0.00931	-0.0268	-0.107	0.122
C_2	0.124	0.0902	0.513	-0.772
C_3	-0.136	0.0233	-0.708	1.51
C_4	-0.183	-0.312	0.0630	-1.02
C_5	-1.91	-16.6	-15.3	-1.89
C_6	-7.97	-17.3	-22.0	-7.25
C_7	0.0422	0.0413	0.0711	-0.0394
C_8	-0.00459	-0.00442	-0.00934	0.00745
C_9	0.0922	2.95e+15	-	-
C_{10}	0.307	0.565	-	-
C_{11}	0.157	13.6	-	-
C_{12}	0.334	-0.577	-	-
C_{13}	0.0259	0.0147	-	-

Table 4.1 — Constants obtained from fitting equation 4.1 to the various sets of results, 0-5%, 5-10%, 10-20%, 20-30%, 30-40%, 40-60%, and 60-80% central Au+Au and d+Au minimum bias collisions. Terms that can be neglected are denoted by a dash (-).

GeV/c. Should it satisfy this criterion the following information for the track is stored in a buffer:

- ϕ^{trig},
- η^{trig},
- p_T^{trig},
- C^{trig}, and
- the unique ID (a number) of the track.

Once all the tracks have been processed all the trigger particles have been identified.

The second step in the process involves constructing the actual angular-difference distributions corresponding to the signal. To do this a second loop over all the primary tracks must take place. For each of these associated tracks, that satisfy the quality cuts mentioned in 3.3.3, the following histograms are filled, for each trigger whose unique ID does not match that of the track in question,

- $\Delta\phi = \phi^{trig} - \phi^{assoc}$ vs. $\Delta\eta = \eta^{trig} - \eta^{assoc}$ vs. p_T^{assoc},
- $\Delta\phi$ vs. $\Delta\eta$ vs. $z_T = p_T^{assoc}/p_T^{trig}$, and
- $v_2^{trig}(p_T^{trig}) \times v_2^{assoc}(p_T^{assoc})$ vs. z_T.

Each histogram is filled with a weight, w, corresponding to

$$w(p_T^{assoc}, \eta^{assoc}) = 1/\epsilon(p_T^{assoc}, \eta^{assoc}) \tag{4.2}$$

where $\epsilon(p_T^{assoc}, \eta^{assoc})$ is the single particle efficiency and acceptance determined as outlined in 4.1.

We use event mixing where the associated track is correlated with all the triggers in the mixed event triggers buffer that corresponds to the same centrality and vertex class. Histograms are filled containing

- $\Delta\phi^{ME} = \phi^{ME,trig} - \phi^{assoc}$ vs. $\Delta\eta^{ME} = \eta^{ME,trig} - \eta^{assoc}$ vs. p_T^{assoc},

- $\Delta\phi^{ME}$ vs. $\Delta\eta^{ME}$ vs. $z_T^{ME} = p_T^{assoc}/p_T^{ME,trig}$, and

These are filled with the same w as before and are the mixed event histograms which will be used to correct for two-particle acceptance effects as the signal correlations are broken by correlating particles from different events.

Once all tracks are processed the trigger particles from this event are added to the mixed event buffer corresponding to the correct centrality and vertex class. Once a buffer is full (arbitrarily chosen to be a maximum of 400 particles) the oldest trigger particles are dropped to make allow for the insertion of newer tracks.

This entire process is then repeated for every event with the only information being carried over from event-to-event being the background particle buffers and the histograms.

4.3 Two-particle Acceptance Corrections

Although the single particle acceptance and correction have been accounted for through the weighting factor there are further acceptance affects that are introduced by the probability of finding particles with a specific $\Delta\eta$ or $\Delta\phi$ value. We used the mixed event histograms to correct for these effects and the corrections are discussed in more detail the following sections.

4.3.1 $\Delta\phi$ Acceptance

The TPC has an azimuthal structure because of the radial sector gaps (as discussed in 3.2.3). The gaps between TPC sectors affect the $\Delta\phi$ correlations because the possible reconstructed $\Delta\phi$ values depends on the location of the trigger particle in ϕ and its relation to the sector gaps. For each possible trigger ϕi-value a slightly different $\Delta\phi$ distribution is possibly reconstructed. The final result will be the weighted sum of all the possible $\Delta\phi$ distributions, weighted by both trigger and associated particle numbers.

To demonstrate this effect consider figure 4.2. In the left hand panel we show a mock-up of the TPC acceptance in azimuth. If you assume that this represents the acceptance for trigger particles and associated particles (which is not the case as there is a p_T dependence to the acceptance) then by sampling from this distribution to obtain a trigger particle and then sampling it again for associated particles one can construct the distribution of azimuthal differences. The right hand panel shows what this distribution would look like for 1000 trigger particles each correlated with 10000 associated tracks, normalised to have a maximum per pair acceptance of 100%.

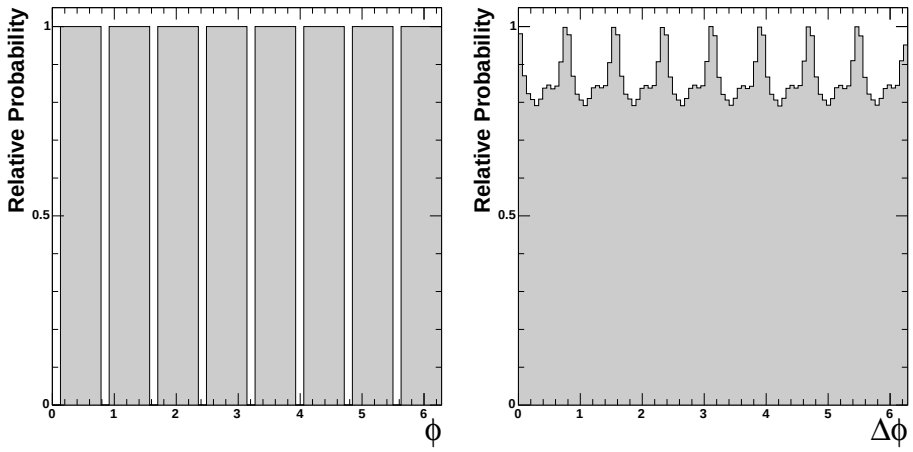

Figure 4.2 — (Left panel) Hypothetical TPC azimuthal acceptance. (Right panel) Resulting azimuthal difference distributing, normalised to have a peak acceptance of 100%.

In reality the acceptance is a function of the p_T of the tracks and for this reason we use data to determine the corrections. By mixing trigger particles from one event with associated particles from another event we can construct the di-hadron acceptance correction because we have sampled the single particle acceptance at each p_T and broken any correlations that would exist in a same event mixture.

4.3.2 $\Delta\eta$ Acceptance

The situation is similar in pseudo-rapidity. The possible location of a trigger particle in the TPC defines a specific range of possible $\Delta\eta$ values which can be measured. This is different for each η location of the trigger particle.

To illustrate this effect figure 4.3 demonstrates a simple approximation of the TPC acceptance in η, constant for $|\eta| < 1$ and 0 elsewhere. We also show the result of sampling 1000 trigger particles from it and correlating each of them with 10000 associated particles from the same distribution, plotting the $\Delta\eta$ values for each pair. This distribution is also normalised to have a peak acceptance of 100%.

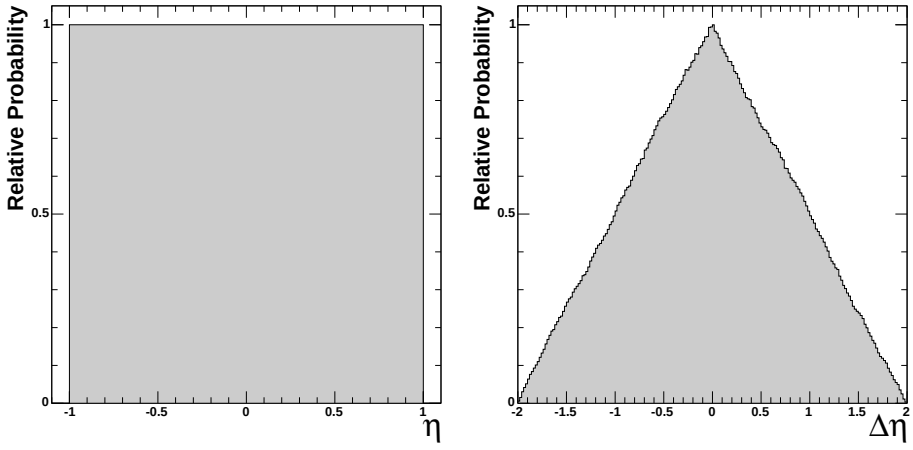

Figure 4.3 — (Left panel)Hypothetical TPC pseudo-rapidity acceptance. (Right panel) Resulting pseudo-rapidity difference distribution, normalised to have a peak acceptance of 100%.

In reality this too has some p_T dependence because the η-acceptance for particles at different p_T values is different (see section 3.4 for more information and figure 4.1).

4.4 Constructing Corrected Di-hadron Distributions

The single particle efficiency and acceptance is corrected during the processing of the data by filling the histograms with the correct weight, w. The two-particle acceptance corrections are implemented once all the data has been processed.

4.4.1 Case 1: Simultaneous $\Delta\eta$ and $\Delta\phi$ Acceptance Correction

This is the simplest case where we construct a correction histogram from the mixed event histogram. The individual entries in the correction histogram are given by projecting a particular p_T into η and ϕ. The projection is then normalised so that the maximum acceptance is 100% and can be represented as

$$\tilde{Y}_{ij}^{ME}(p_T) = \frac{1}{max(Y^{ME}(p_T))} Y_{ij}^{ME}(p_T) \tag{4.3}$$

where $Y_{ij}^{ME}(p_T)$ is an entry with i and j corresponding to the index in η and ϕ respectively and for a given p_T. In the analysis, 20 bins in the η-direction were used while in the ϕ-direction 49 bins were used. The p_T binning was such that there were 40 bins of 25 MeV starting from 0 MeV, followed by 20 bins of 50 MeV and then another 20 bins of 100 MeV. The resulting corrections, and its projection in the $\Delta\eta$ and $\Delta\phi$ planes is shown in figure 4.4, for the case where $2.5 < p_T^{trig.} < 3.0$ GeV/c and $2.0 < p_T^{assoc.} < 2.1$ GeV/c from 0-12% central Au+Au collisions.

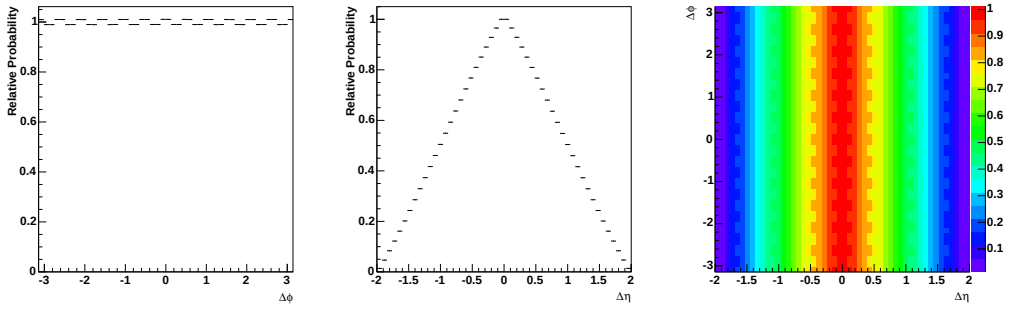

Figure 4.4 — Acceptance corrections for $2.5 < p_T^{trig.} < 3.0$ GeV/c and $2.0 < p_T^{assoc.} < 2.1$ GeV/c from 0-12% central Au+Au collisions. From left to right: $\Delta\phi$ projection, $\Delta\eta$ projection and full 2D correction.

The acceptance corrected histogram is then given by

$$\tilde{Y}_{ij}(p_T) = \frac{1}{\tilde{Y}_{ij}^{ME}(p_T))} Y_{ij}^{Raw}(p_T), \tag{4.4}$$

where $Y_{ij}^{Raw}(p_T)$ is an entry in the signal histogram with i and j corresponding to the index in η and ϕ respectively and for a given p_T.

From the corrected $\tilde{Y}_{ij}(p_T)$ we can construct the projections on either $\Delta\eta$ (i) or $\Delta\phi$ (j) for a p_T range of interest. The corrected distribution function, as discussed in section 2.5, consists of a number of components which we treat individually. The various components that can be analysed for a complete correction are shown in figure 4.5. The full distribution (top left) consists of a large v_2 modulated background which is flat in $\Delta\eta$ as shown in the top right panel. On this large background the near-side consists of a small angle peak jet-like peak (bottom left) which is on a flat ridge in $\Delta\eta$ which is only located on the near-side.

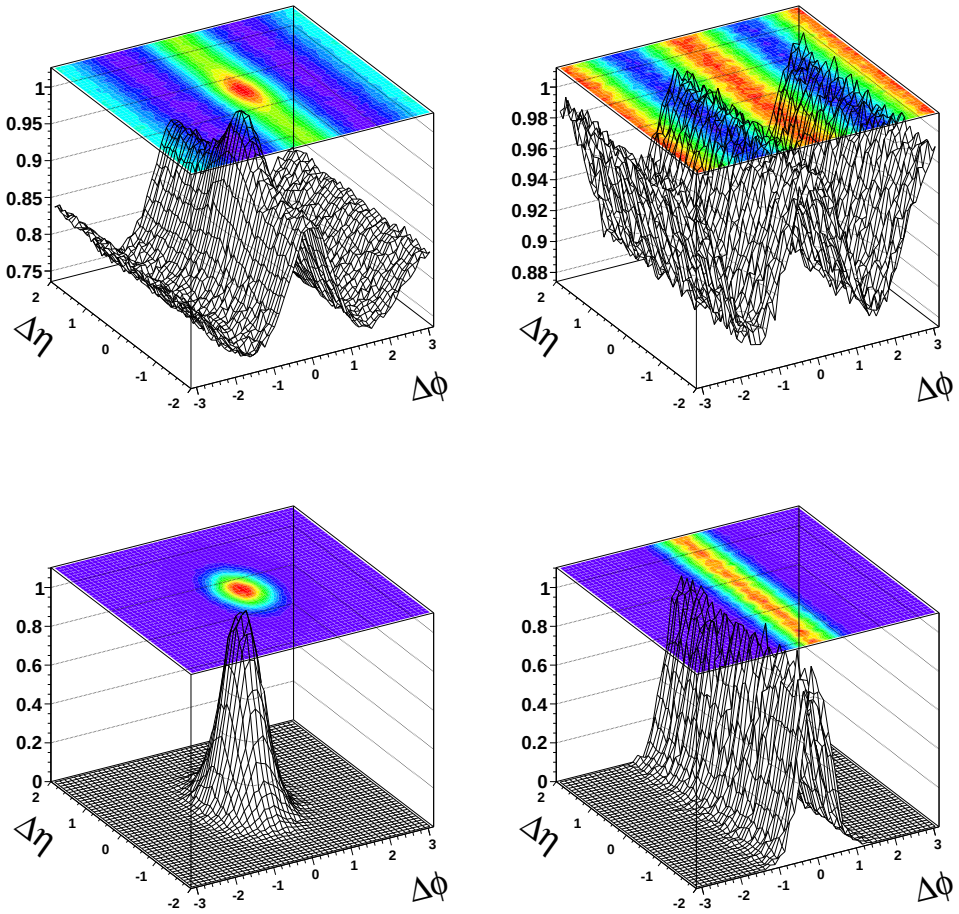

Figure 4.5 — An idealised and simplified multi-component picture of angular di-hadron distributions. (Top left) The complete distribution. (Top right) v_2-modulated background. (Bottom left) Jet peak from parton fragmentation. (Bottom right) $\Delta\eta$-ridge component.

When the v_2 modulated background is subtracted in practice there is a

residual structure one the away-side, in addition to the ridge and peak on the near-side, whose shape is $p_T^{assoc.}$ and $p_T^{trig.}$ dependent and will be discussed further in section 5.

4.4.2 Case 2: $\Delta\phi$ Acceptance Correction

In the case where we do not correct for the $\Delta\eta$ acceptance, the $\Delta\phi$-correction is implemented in a different manner. The mixed event histogram should now be normalised differently in each $\Delta\eta$ range (i) before applying the mixed event correction to the signal histogram ($Y_{ij}^{ME}(p_T)$). To do this we scale normalise the mixed event yield to the maximum value in a specific range in $\Delta\eta$ ($max(Y_i^{ME}(p_T))$) thus ignoring the correction for the $\Delta\eta$ acceptance:

$$\tilde{Y}_{ij}^{ME}(p_T) = \frac{1}{max(Y_i^{ME}(p_T))} Y_{ij}^{ME}(p_T). \tag{4.5}$$

The resulting corrections, and it's projection in the $\Delta\eta$ and $\Delta\phi$ planes is shown in figure 4.6, for the case where $2.5 < p_T^{trig.} < 3.0$ GeV/c and $2.0 < p_T^{assoc.} < 2.1$ GeV/c from 0-12% central Au+Au collisions.

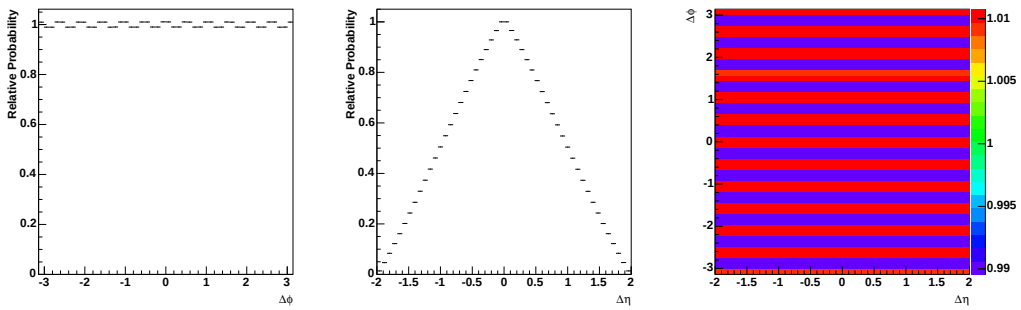

Figure 4.6 — Acceptance corrections for $2.5 < p_T^{trig.} < 3.0$ GeV/c and $2.0 < p_T^{assoc.} < 2.1$ GeV/c from 0-12% central Au+Au collisions. From left to right: $\Delta\phi$ projection, $\Delta\eta$ projection and full 2D correction for the case where only the $\Delta\phi$-acceptance is being corrected for.

In the case where there is no $\Delta\eta$ correction the idealised $(\Delta\eta, \Delta\phi)$ distribution shown in figure 4.5 is distorted and no structures are flat in $\Delta\eta$ any longer. The triangular $\Delta\eta$-acceptance dominates the shapes and the effect of this acceptance on the idealised case is shown in figure 4.7.

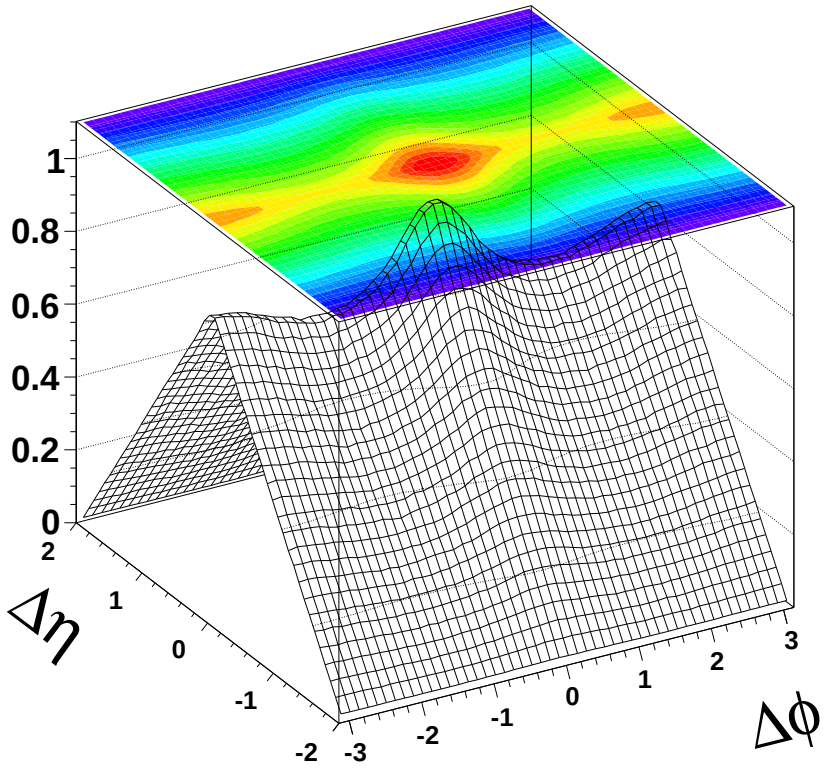

Figure 4.7 — The idealised distribution as measured by the STAR detector with no $\Delta\eta$-acceptance correction.

4.5 Correlations as Independent Components

4.5.1 Underlying Uncorrelated Background

If jet-like correlations are the only correlations in the event then the background would be flat and could easily be removed from the final distributions. In reality all particles are correlated with the reaction plane as determined by v_2 measurements as discussed in 2.2.5. This gives rise to a $cos(2\Delta\phi)$ modulation of the background.

The functional form of the background to be subtracted is

$$B(\Delta\phi, p_T) = P\left(1 + 2v_2(p_T^{trig})v_2(p_T^{assoc})\cos(2\Delta\phi)\right). \tag{4.6}$$

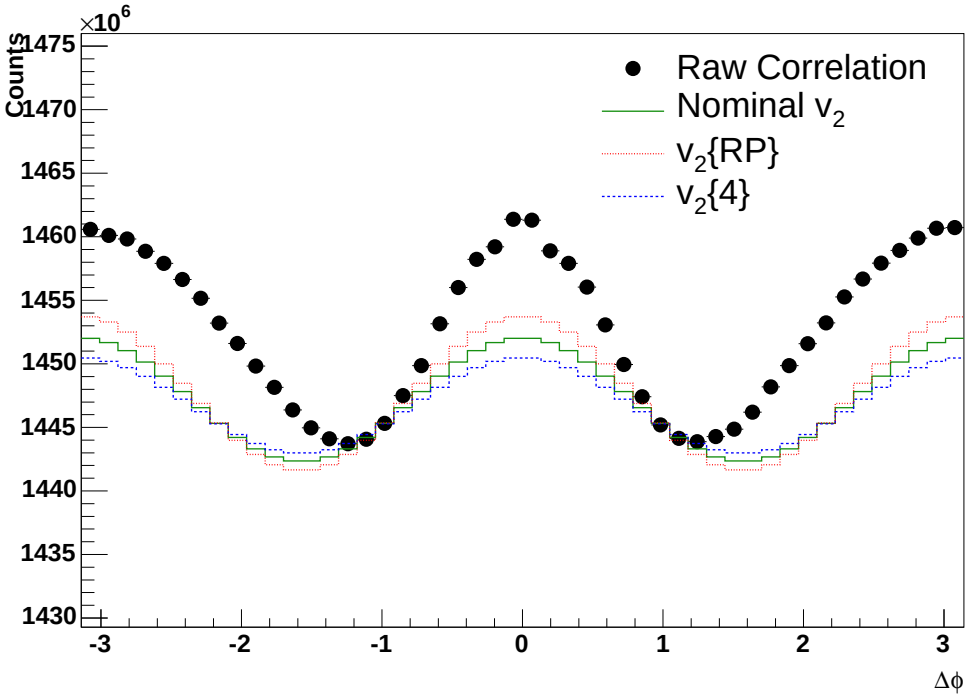

Figure 4.8 — A sample raw distribution and the different v_2 curves that are used to subtract the uncorrelated background.

P is determined by normalising to the region $0.8 < |\Delta\phi| < 1.2$, where the jet signal is expected to be minimal [138] and the v_2 values are taken from [30]. For the case where multiple p_T bins are combined a weighted $v_2(p_T^{assoc})$ needs to be used. This is determined by weighting the v_2 value in a specific p_T bin by the total corrected yield in that bin,

$$v_2^{weighted} = \frac{\sum_j^{N_b} \tilde{Y}(j) v_2(j)}{\sum_j^{N_b} \tilde{Y}(j)}, \tag{4.7}$$

where N_b is the number of p_T bins to combine and $\tilde{Y}(j)$ is $\tilde{Y}(i,j)$ integrated over i.

For the case where multiple centralities are combined a further sum over the relevant centrality bins is required as follows

$$v_2^{weighted} = \frac{\sum_i^{N_c} \sum_j^{N_b} \tilde{Y}(i,j) v_2(i,j)}{\sum_i^{N_c} \sum_j^{N_b} \tilde{Y}(i,j)} \tag{4.8}$$

where N_c is the number of centrality bins to combine.

The weighted pedestal value is determined from

$$P^{weighted} = \frac{\sum_i^{N_c} \sum_j^{N_b} \tilde{Y}(i,j) P(i,j)}{\sum_i^{N_c} \sum_j^{N_b} \tilde{Y}(i,j)}. \tag{4.9}$$

Systematic Uncertainty from v_2

The question of determining the true v_2 in an event is difficult. There are other correlations in the event which could mimic or distort a v_2 signal, so called "non-flow" contributions [30]. We assume that the v_2 for events of a certain centrality are the same whether or not the event contains a trigger particle even though a strong jet signal could affect the v_2 of the collision.

In addition there are event-by-event fluctuations which bias the v_2 measurement [139]. To encapsulate this uncertainty in the true v_2, we allow a generous spread in the range of v_2 values we consider. The extreme cases we use are the values determined using the "modified reaction plane" method ($v_2\{RP\}$) and the four particle cumulant method ($v_2\{4\}$). As a nominal value we take the mean of these two measurements.

In figure 4.8 we show a sample raw distribution from central Au+Au data with the 3 different v_2 curves superimposed. The nominal v_2 is shown in green, the $v_2\{RP\}$ is shown in red, and the $v_2\{4\}$ is shown in blue.

4.5.2 Near-side Long-Range $\Delta\eta$ Correlation ("Ridge")

As discussed in 2.5.1 there is a long range near-side correlation which contributes to the near-side yield. Current understanding is that the ridge is flat in $\Delta\eta$ up to $\Delta\eta \sim 1.5$. The ridge complicates the measurement on the near-side. Vacuum fragmentation does not create a ridge-like structure.

To conduct detailed studies of the jet peak on the near-side it is insightful to subtract the ridge contribution. The procedure depends on whether or not the distributions have been corrected for $\Delta\eta$ acceptance. The underlying assumption is that the true ridge is flat in the range $|\Delta\eta| < 1.5$.

$\Delta\eta$- and $\Delta\phi$-Corrected Distributions

In the case where both $\Delta\eta$- and $\Delta\phi$ acceptance corrections have been applied we project two different $\Delta\eta$ ranges,

- $|\Delta\eta| < 0.72$, and
- $0.72 < |\Delta\eta| < 1.44$,

onto $\Delta\phi$. The first range contains both the near-side peak and a ridge contribution while the second range, from larger $\Delta\eta$, contains only the ridge contribution with negligible peak contributions. With the working assumption that the ridge is flat in $\Delta\eta$ subtracting the second range from the first will remove the ridge contribution leaving only the near-side peak yield. The ranges are demonstrated in figure 4.9.

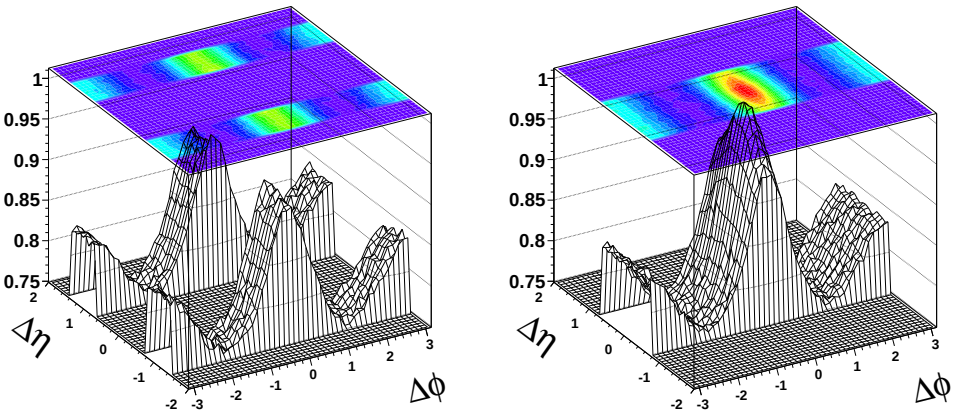

Figure 4.9 — Two projections, from the idealised case, used for subtracting the ridge. The left panel is for the range $0.72 < |\Delta\eta| < 1.44$ and the right panel for $|\Delta\eta| < 0.72$.

In implementing a $\Delta\eta$-acceptance correction one assumes that the correlation strengths are the same for triggers at $\eta = \pm 1$ and $\eta = 0$, however, this would mean that the away-side correlation is the same over 4 units of pseudo-rapidity ($\eta^{trig} = \pm 1$ and $\eta^{assoc} = \mp 1$) which is not known and cannot be verified within the STAR acceptance. For this reason, this correction is applied with care and primarily to two-dimensional $\Delta\eta$, $\Delta\phi$ distributions to for clarity. To avoid making this assumption and allow us

to compare to previous azimuthal di-hadron distribution analyses we will restrict ourselves to only implementing the $\Delta\phi$-acceptance correction as discussed in the next section.

$\Delta\phi$ Corrected Correlations

For the case where only the $\Delta\phi$ acceptance corrections have been applied we still project into the same $\Delta\eta$ ranges but now the ridge contribution is not the same in both ranges because of the triangular acceptance as demonstrated in figure 4.10. The shape of the away-side and ridge is still the same in both $\Delta\eta$ ranges and to correctly scale the shape of the large $\Delta\eta$ range projection so that the ridge contribution is the same in both cases we scale the distribution so that both ranges match on the away-side. The away-side is also flat in $\Delta\eta$ giving the appropriate scaling factor for the ridge as well. The scaled distribution is then subtracted from the first pro-

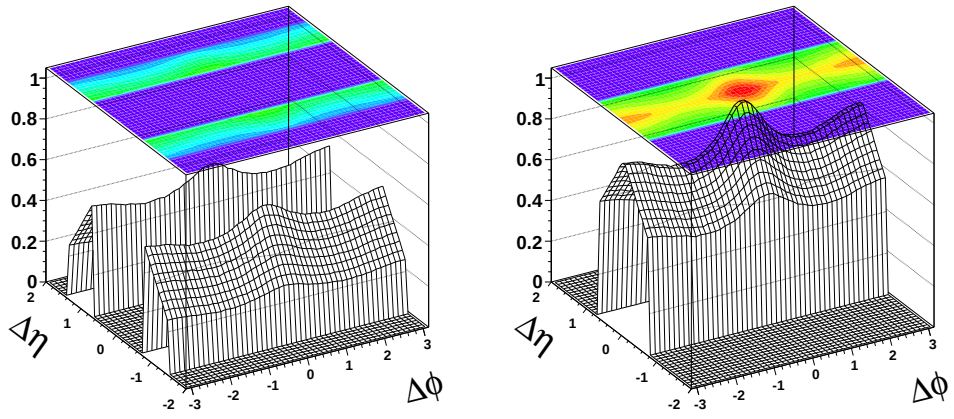

Figure 4.10 — Two projections, from the idealised case, used for subtracting the ridge when no $\Delta\eta$-correction has been applied. The left panel is for the range $0.72 < |\Delta\eta| < 1.44$ and the right panel for $|\Delta\eta| < 0.72$.

jection to remove the ridge. It is convenient to conduct studies both with and without the $\Delta\eta$ acceptance corrected for because both cases exist in the literature and so a full set of consistency checks requires both cases to be evaluated.

4.6 z_T Distributions

As discussed in 2.7, hadron triggered fragmentation functions are also of interest. These can be constructed following almost the exact same procedure as described above with the only change being that we replace p_T with z_T. The same single- and two-particle corrections apply and another set of mixed events is created as described in section 4.2.

The only additional challenge is the fact that information is lost regarding the p_T of the trigger and associated particle complicating the selection of the v_2 that needs be subtracted in any particular z_T bin. To resolve this we added additional histograms to store $v_2(p_T^{trig}) \cdot v_2(p_T^{assoc})$ vs. z_T as the v_2 values are known. From these we can project the distributions of $v_2(p_T^{trig}) \cdot v_2(p_T^{assoc})$ over the z_T range of interest. The mean of the projection is the yield-weighted $v_2(p_T^{trig}) \cdot v_2(p_T^{assoc})$ that needs to be subtracted.

The 2-dimensional $v_2(p_T^{trig}) \cdot v_2(p_T^{assoc})$ vs. z_T histograms from Au+Au collisions are shown in figure 4.11 for 2.5$< p_T^{trig.} <$3.0 GeV/c (top left), 3.0$< p_T^{trig.} <$4.0 GeV/c (top right), 4.0$< p_T^{trig.} <$6.0 GeV/c (bottom left), and 6.0$< p_T^{trig.} <$10.0 GeV/c (bottom right).

The curves bounding the distributions for different centralities can be determined by taking the extreme values of $p_T^{trig.}$ for the case in question and plotting $v_2(p_T^{assoc})/v_2(p_T^{Max/Min\ trig})$ vs. $v_2(p_T^{assoc}) \cdot v_2(p_T^{Max/Min\ trig})$ where $v_2(p_T^{Max/Min\ trig})$ is the v_2 of the trigger using the limiting cases of v_2RP and v_24.

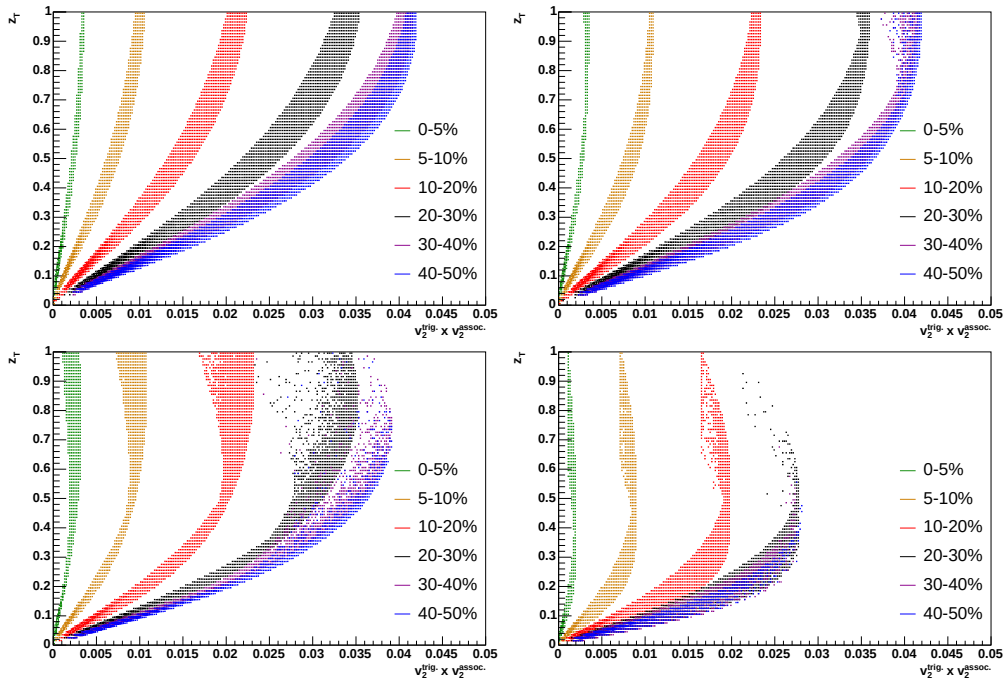

Figure 4.11 — Distributions of z_T vs. $v_2(p_T^{trig})v_2(p_T^{assoc})$ which are used to determine the mean $v_2(p_T^{trig})v_2(p_T^{assoc})$ to subtract from a correlation function for a given z_T bin. The 4 panels show the change in shape for different $p_T^{trig.}$ selections: 2.5< $p_T^{trig.}$ <3.0 GeV/c (top left), 3.0< $p_T^{trig.}$ <4.0 GeV/c (top right), 4.0< $p_T^{trig.}$ <6.0 GeV/c (bottom left), and 6.0< $p_T^{trig.}$ <10.0 GeV/c (bottom right).

Chapter 5

Results and Discussion

There is nothing like looking, if you want to find something. You certainly usually find something, if you look, but it is not always quite the something you were after.

J. R. R. Tolkien

5.1 d+Au Reference Results

d+Au measurements form the reference to compare to Au+Au results and the analysis of the d+Au data is the first step in our analysis. The procedure for the analysis has been described in chapter 4 and here we present the results from the minimum bias d+Au data-set.

In figure 5.1 we present signal di-hadron distributions for different choices of $p_T^{trig.}$ and $p_T^{assoc.}$. The $p_T^{assoc.}$ selections, 0.3< $p_T^{assoc.}$ <0.8 GeV/c, 0.8< $p_T^{assoc.}$ <1.3 GeV/c, 1.3< $p_T^{assoc.}$ <1.8 GeV/c, and 2.0< $p_T^{assoc.}$ <4.0 GeV/c, span the p_T-range of study and have some overlap with the range of $p_T^{trig.}$studied. The different selections of $p_T^{trig.}$are 2.5< $p_T^{trig.}$ <3.0 GeV/c, 3.0< $p_T^{trig.}$ <4.0 GeV/c, 4.0< $p_T^{trig.}$ <6.0 GeV/c, and 6.0< $p_T^{trig.}$ <10.0 GeV/c. Each row in figure 5.1 corresponds to a fixed choice of $p_T^{assoc.}$ and each column to a fixed choice of $p_T^{trig.}$, this is the same format that will be used in the next section to simplify comparison. The vertical lines show the statistical uncertainty in the data.

The general feature common to all panels is that of two peaks, one centred

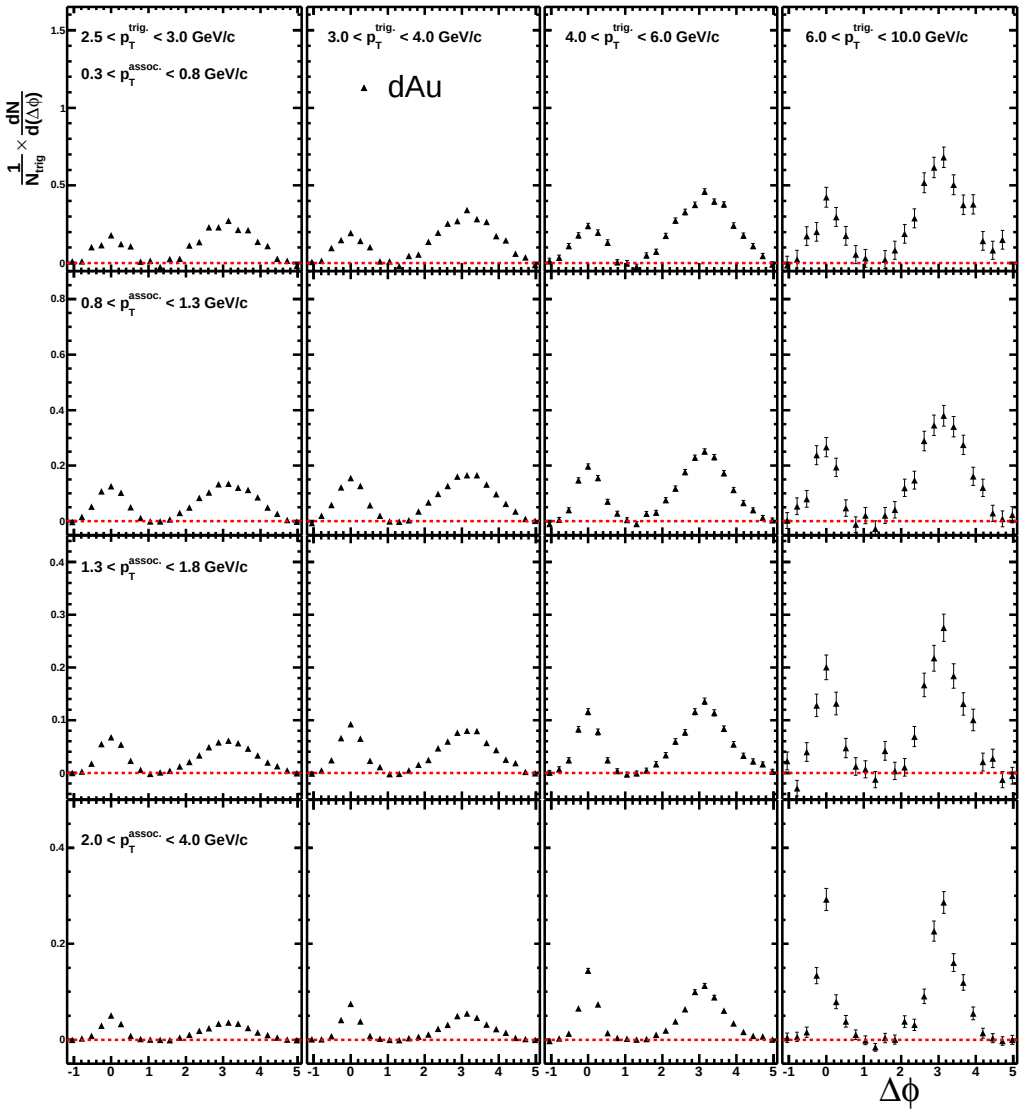

Figure 5.1 — Di-hadron distributions for minimum bias d+Au collisions. Results are shown for different $p_T^{assoc.}$ (from top to bottom), 0.3< $p_T^{assoc.}$ <0.8 GeV/c, 0.8< $p_T^{assoc.}$ <1.3 GeV/c, 1.3< $p_T^{assoc.}$ <1.8 GeV/c, and 2.0< $p_T^{assoc.}$ <4.0 GeV/c as well as for different $p_T^{trig.}$ (from left to right), 2.5< $p_T^{trig.}$ <3.0 GeV/c, 3.0< $p_T^{trig.}$ <4.0 GeV/c, 4.0< $p_T^{trig.}$ <6.0 GeV/c, and 6.0< $p_T^{trig.}$ <10.0 GeV/c. The bars show the statistical uncertainty in the data and the band around zero shows the statistical uncertainty in the pedestal normalisation.

at $\Delta\phi = 0$, called the near-side, and the other centred at $\Delta\phi = \pi$, called the away-side. This is from the fragmentation of back-to-back scattered partons. The away-side peak is always broader than the near-side peak and can be attributed to intrinsic transverse momentum, nuclear-k_T, which in-

troduces acoplanarity and thus broadening.

For a fixed $p_T^{assoc.}$ the yield in both the near-side and away-side peaks increases with increasing $p_T^{trig.}$. This is because larger $p_T^{trig.}$ selects jets with larger energy and thus larger multiplicity.

For a fixed $p_T^{trig.}$, the yield decreases with increasing $p_T^{assoc.}$ (note different vertical scale) as expected from the steeply falling p_T-spectrum from fragmentation and the peaks become narrower on both the near- and away-sides. This is because harder fragmentation products are more collimated with the jet axis and is a well-known effect.

The d+Au reference shows the expected shapes and dependencies on $p_T^{trig.}$ and $p_T^{assoc.}$ from fragmentation of partons from hard scattering and will be used as a reference for the Au+Au analysis.

5.2 Au+Au Results

The set of minimum bias and central triggered Au+Au collisions includes a wide range of centralities as already discussed in 3.3.1 and the centrality affects the control parameters significantly, the medium size (path-length), the number of binary collisions, the v_2 and the multiplicity of the background.

5.2.1 60-80% Central Collisions

In these collisions (60-80%), the most peripheral we study, we expect the results to look the most similar to d+Au as the system is very small and the partons will have the smallest path-length in the collision volume (medium).

In figure 5.2 we present signal di-hadron distributions from 60-80% central collisions for 0.3< $p_T^{assoc.}$ <0.8 GeV/c, 0.8< $p_T^{assoc.}$ <1.3 GeV/c, 1.3< $p_T^{assoc.}$ <1.8 GeV/c, and 2.0< $p_T^{assoc.}$ <4.0 GeV/c as well as for different $p_T^{trig.}$, 2.5< $p_T^{trig.}$ <3.0 GeV/c, 3.0< $p_T^{trig.}$ <4.0 GeV/c, 4.0< $p_T^{trig.}$ <6.0 GeV/c, and 6.0< $p_T^{trig.}$ <10.0 GeV/c. The vertical bars show the statistical uncertainty in the data and the band around zero shows the statistical uncertainty in

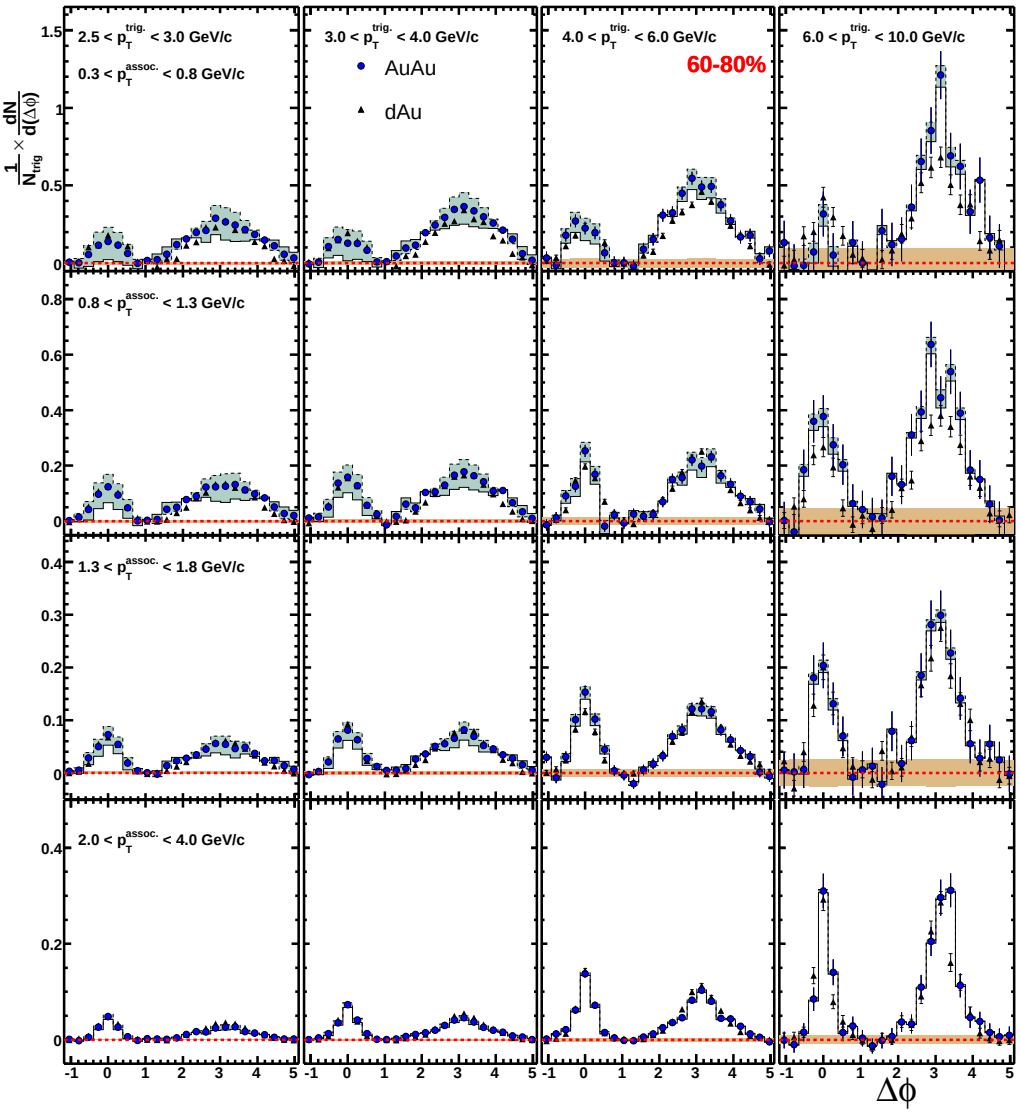

Figure 5.2 — Di-hadron distributions for 60-80% central collisions from the minimum bias Au+Au collisions. Results are shown for different $p_T^{assoc.}$ (from top to bottom), 0.3< $p_T^{assoc.}$ <0.8 GeV/c, 0.8< $p_T^{assoc.}$ <1.3 GeV/c, 1.3< $p_T^{assoc.}$ <1.8 GeV/c, and 2.0< $p_T^{assoc.}$ <4.0 GeV/c as well as for different $p_T^{trig.}$ (from left to right), 2.5< $p_T^{trig.}$ <3.0 GeV/c, 3.0< $p_T^{trig.}$ <4.0 GeV/c, 4.0< $p_T^{trig.}$ <6.0 GeV/c, and 6.0< $p_T^{trig.}$ <10.0 GeV/c. d+Au results are included for reference. The vertical bars show the statistical uncertainty in the data and the band around zero shows the statistical uncertainty in the background normalisation. The band surrounding the data show the systematic uncertainty from v_2.

the background normalisation. The band surrounding the data show the systematic uncertainty from v_2. The d+Au data (from figure 5.1) are in-

cluded for reference.

The parameters for the background subtraction are given in table 5.1 and include the $\langle v_2^{assoc.} \rangle \cdot \langle v_2^{trig.} \rangle$ as well as the pedestal value used in the background normalisation, P, as discussed in section 4.5.1.

$p_T^{assoc.}$ [GeV/c]	$\langle v_2^{assoc.} \rangle \cdot \langle v_2^{trigger} \rangle$ [%]	$P_{\lvert\Delta\eta\rvert<2.0}$
$2.5 < p_T^{trig.} < 3.0$ GeV/c		
$0.3 < p_T^{assoc.} < 0.8$	$2.27^{+1.3}_{-1.0}$	6.30 ± 0.0062
$0.8 < p_T^{assoc.} < 1.3$	$4.32^{+2.5}_{-2.0}$	1.62 ± 0.0030
$1.3 < p_T^{assoc.} < 1.8$	$5.70^{+3.2}_{-2.6}$	0.418 ± 0.0015
$2.0 < p_T^{assoc.} < 4.0$	$6.69^{+3.8}_{-3.0}$	0.106 ± 0.00075
$3.0 < p_T^{trig.} < 4.0$ GeV/c		
$0.3 < p_T^{assoc.} < 0.8$	$2.21^{+1.3}_{-1.0}$	6.25 ± 0.0090
$0.8 < p_T^{assoc.} < 1.3$	$4.21^{+2.4}_{-1.9}$	1.61 ± 0.0044
$1.3 < p_T^{assoc.} < 1.8$	$5.56^{+3.2}_{-2.5}$	0.416 ± 0.0022
$2.0 < p_T^{assoc.} < 4.0$	$6.52^{+3.7}_{-3.3}$	0.105 ± 0.0011
$4.0 < p_T^{trig.} < 6.0$ GeV/c		
$0.3 < p_T^{assoc.} < 0.8$	$1.57^{+0.93}_{-0.72}$	6.14 ± 0.020
$0.8 < p_T^{assoc.} < 1.3$	$2.99^{+1.8}_{-1.4}$	1.59 ± 0.0099
$1.3 < p_T^{assoc.} < 1.8$	$3.94^{+2.3}_{-1.8}$	0.406 ± 0.0049
$2.0 < p_T^{assoc.} < 4.0$	$4.48^{+2.8}_{-2.1}$	0.101 ± 0.0024
$6.0 < p_T^{trig.} < 10.0$ GeV/c		
$0.3 < p_T^{assoc.} < 0.8$	$1.57^{+0.92}_{-0.72}$	6.00 ± 0.070
$0.8 < p_T^{assoc.} < 1.3$	$2.99^{+1.8}_{-1.4}$	1.46 ± 0.034
$1.3 < p_T^{assoc.} < 1.8$	$3.94^{+2.3}_{-1.8}$	0.392 ± 0.017
$2.0 < p_T^{assoc.} < 4.0$	$4.48^{+2.8}_{-2.1}$	0.0995 ± 0.0085

Table 5.1 — The v_2 values and the normalisation corresponding to the panels in figure 5.2.

Similar to the d+Au results, figure 5.2 shows a near- and away-side peak in all panels which is of similar magnitude and width to the corresponding peak from the d+Au data and thus exhibits the same trends indicative of fragmentation; a narrowing peak width with increasing $p_T^{assoc.}$, increasing yield with increasing $p_T^{trig.}$ and an away-side peak which is broader than the near-side.

The peripheral Au+Au results indicate that we are indeed measuring the products of back-to-back parton fragmentation.

5.2.2 40-60% Central Collisions

As the centrality increases so does the medium size and density, implying greater in-medium path-lengths and more scattering centres for partons to interact with. We expect to see medium effects become more prominent for more central collisions because of this.

The next most peripheral centrality bin is 40-60% and the results for this bin are presented in figure 5.3 for the same selections of $p_T^{trig.}$ and $p_T^{assoc.}$ as shown in figures 5.1 and 5.2. The d+Au data (from figure 5.1) are included for reference. The vertical bars denote the statistical uncertainty and the bands around the data the systematic uncertainty from v_2. The band around zero shows the uncertainty in the pedestal normalisation.

The parameters for the background subtraction are given in table 5.2 and include the $\langle v_2^{assoc.} \rangle \cdot \langle v_2^{trig.} \rangle$ as well as the pedestal value used in the background normalisation, P. Note that the $\langle v_2^{assoc.} \rangle \cdot \langle v_2^{trig.} \rangle$ values have increased relative to the 60-80% case as v_2 increases towards mid-central collisions.

In all panels there is still a near- and away-side peak but we now show significant deviations, in the form of increased yield and broadening, from the d+Au reference data in a number of panels. The most significant differences are in the top left panel (softest $p_T^{assoc.}$ and $p_T^{trig.}$) and the relative differences decrease smoothly with increasing $p_T^{trig.}$ and/or $p_T^{assoc.}$ to the extent that the hardest $p_T^{trig.}$ and/or $p_T^{assoc.}$ agree with the d+Au reference data. In all cases where there is increased yield, both the near- and away-side yields are increased.

Di-hadron distributions are affected by the increase in the size of the collision overlap region with an increased yield for both the near- and away-side. The influence of the system size is first apparent at lower p_Ts.

5.2.3 20-40% Central Collisions

In mid-central collisions (20-40%) the overlap region is larger than in 40-60% central collisions and any difference to the d+Au reference that are dependent on the system size should be more evident in this centrality selection than in the 40-60% data.

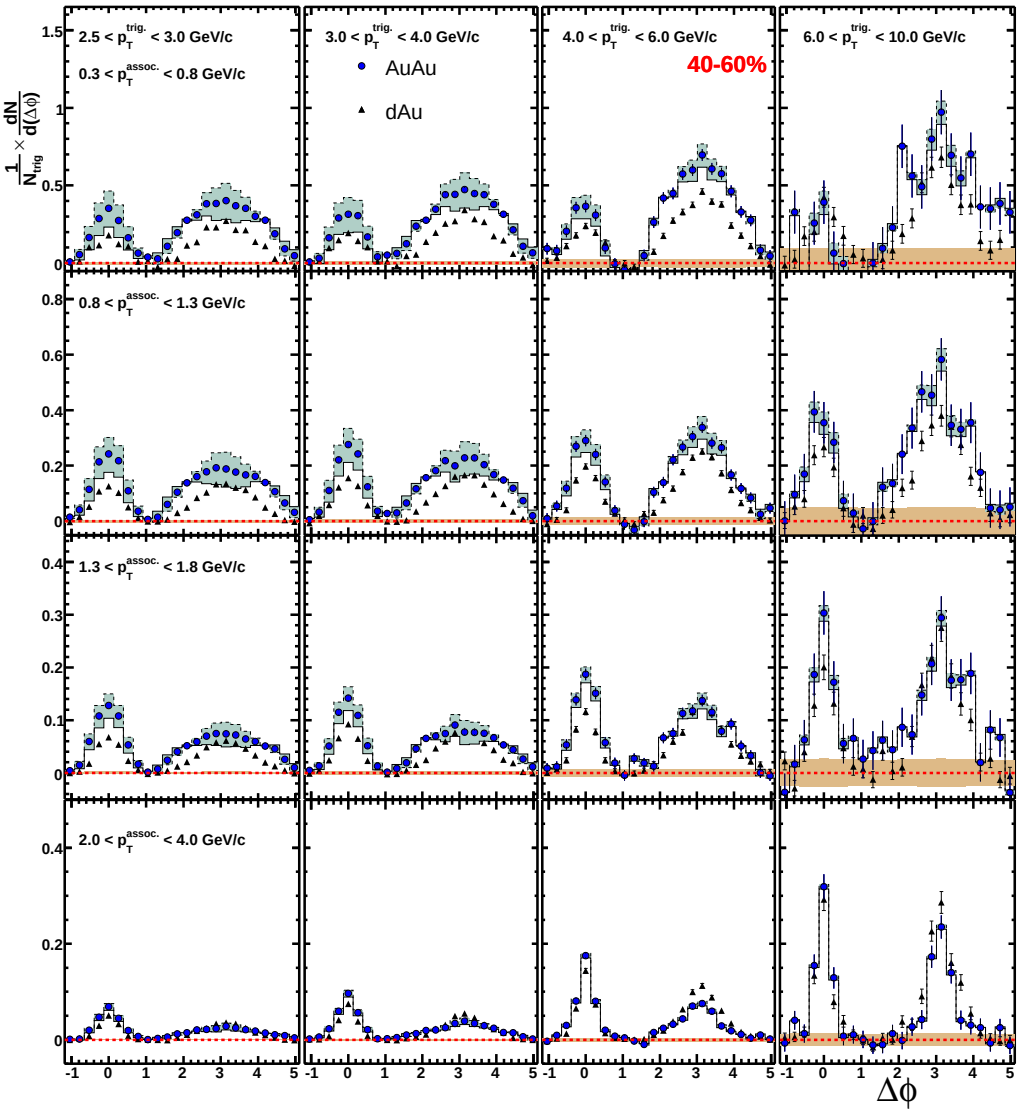

Figure 5.3 — Di-hadron distributions for 40-60% central collisions from the minimum bias Au+Au collisions. Results are shown for different $p_T^{assoc.}$ (from top to bottom), 0.3< $p_T^{assoc.}$ <0.8 GeV/c, 0.8< $p_T^{assoc.}$ <1.3 GeV/c, 1.3< $p_T^{assoc.}$ <1.8 GeV/c, and 2.0< $p_T^{assoc.}$ <4.0 GeV/c as well as for different $p_T^{trig.}$ (from left to right), 2.5< $p_T^{trig.}$ <3.0 GeV/c, 3.0< $p_T^{trig.}$ <4.0 GeV/c, 4.0< $p_T^{trig.}$ <6.0 GeV/c, and 6.0< $p_T^{trig.}$ <10.0 GeV/c. The bars show the statistical uncertainty in the data and the band around zero shows the statistical uncertainty in the background normalisation. The band surrounding the data show the systematic uncertainty from v_2.

The results for 20-40% centrality are presented in figure 5.4 for the same selections of $p_T^{trig.}$ and $p_T^{assoc.}$ as in figures 5.1, 5.2 and 5.3. The d+Au data

$p_T^{assoc.}$ [GeV/c]	$\langle v_2^{assoc.} \rangle \cdot \langle v_2^{trigger} \rangle$ [%]	$P_{\lvert\Delta\eta\rvert<2.0}$
$2.5 < p_T^{trig.} < 3.0$ GeV/c		
$0.3 < p_T^{assoc.} < 0.8$	$2.62^{+0.48}_{-0.44}$	17.6 ± 0.0055
$0.8 < p_T^{assoc.} < 1.3$	$5.01^{+0.92}_{-0.85}$	4.94 ± 0.0028
$1.3 < p_T^{assoc.} < 1.8$	$6.71^{+1.2}_{-1.1}$	1.36 ± 0.0014
$2.0 < p_T^{assoc.} < 4.0$	$8.09^{+1.5}_{-1.4}$	0.340 ± 0.00071
$3.0 < p_T^{trig.} < 4.0$ GeV/c		
$0.3 < p_T^{assoc.} < 0.8$	$2.56^{+0.47}_{-0.43}$	17.5 ± 0.0081
$0.8 < p_T^{assoc.} < 1.3$	$4.91^{+0.90}_{-0.83}$	4.91 ± 0.0041
$1.3 < p_T^{assoc.} < 1.8$	$6.57^{+1.2}_{-1.1}$	1.35 ± 0.0021
$2.0 < p_T^{assoc.} < 4.0$	$7.92^{+1.5}_{-1.3}$	0.337 ± 0.0011
$4.0 < p_T^{trig.} < 6.0$ GeV/c		
$0.3 < p_T^{assoc.} < 0.8$	$1.74^{+0.32}_{-0.29}$	17.3 ± 0.019
$0.8 < p_T^{assoc.} < 1.3$	$3.33^{+0.61}_{-0.56}$	4.87 ± 0.0096
$1.3 < p_T^{assoc.} < 1.8$	$4.45^{+0.82}_{-0.76}$	1.34 ± 0.0050
$2.0 < p_T^{assoc.} < 4.0$	$5.37^{+0.99}_{-0.91}$	0.337 ± 0.0025
$6.0 < p_T^{trig.} < 10.0$ GeV/c		
$0.3 < p_T^{assoc.} < 0.8$	$1.74^{+0.32}_{-0.29}$	17.2 ± 0.068
$0.8 < p_T^{assoc.} < 1.3$	$3.33^{+0.62}_{-0.56}$	4.80 ± 0.035
$1.3 < p_T^{assoc.} < 1.8$	$4.45^{+0.82}_{-0.76}$	1.31 ± 0.018
$2.0 < p_T^{assoc.} < 4.0$	$5.38^{+0.99}_{-0.91}$	0.341 ± 0.0091

Table 5.2 — The v_2 values and the normalisation corresponding to the panels in figure 5.3.

(from figure 5.1) are included for reference. The vertical bars indicate the statistical error and the bands around the data points show the systematic uncertainty from v_2.

The parameters for the background subtraction are given in table 5.3 and includes the $\langle v_2^{assoc.} \rangle \cdot \langle v_2^{trig.} \rangle$ as well as the pedestal value used in the background normalisation, P. The systematic uncertainty from v_2 is larger in this centrality than the others as these collisions have the largest elliptic flow.

In figure 5.4 a number of interesting features are present and we begin our discussion with the near-side peaks. The observation we made from figure 5.3 regarding the increase in yield at lower-p_T is again evident but more pronounced with much larger increases in yield relative to the d+Au results. The increase in yield is larger and extends to higher $p_T^{assoc.}$ for the 3 lower $p_T^{trig.}$ selections, $2.5 < p_T^{trig.} < 3.0$ GeV/c, $3.0 < p_T^{trig.} < 4.0$ GeV/c, and $4.0 < p_T^{trig.} < 6.0$ GeV/c. The hardest $p_T^{trig.}$, $6.0 < p_T^{trig.} < 10.0$ GeV/c, may also

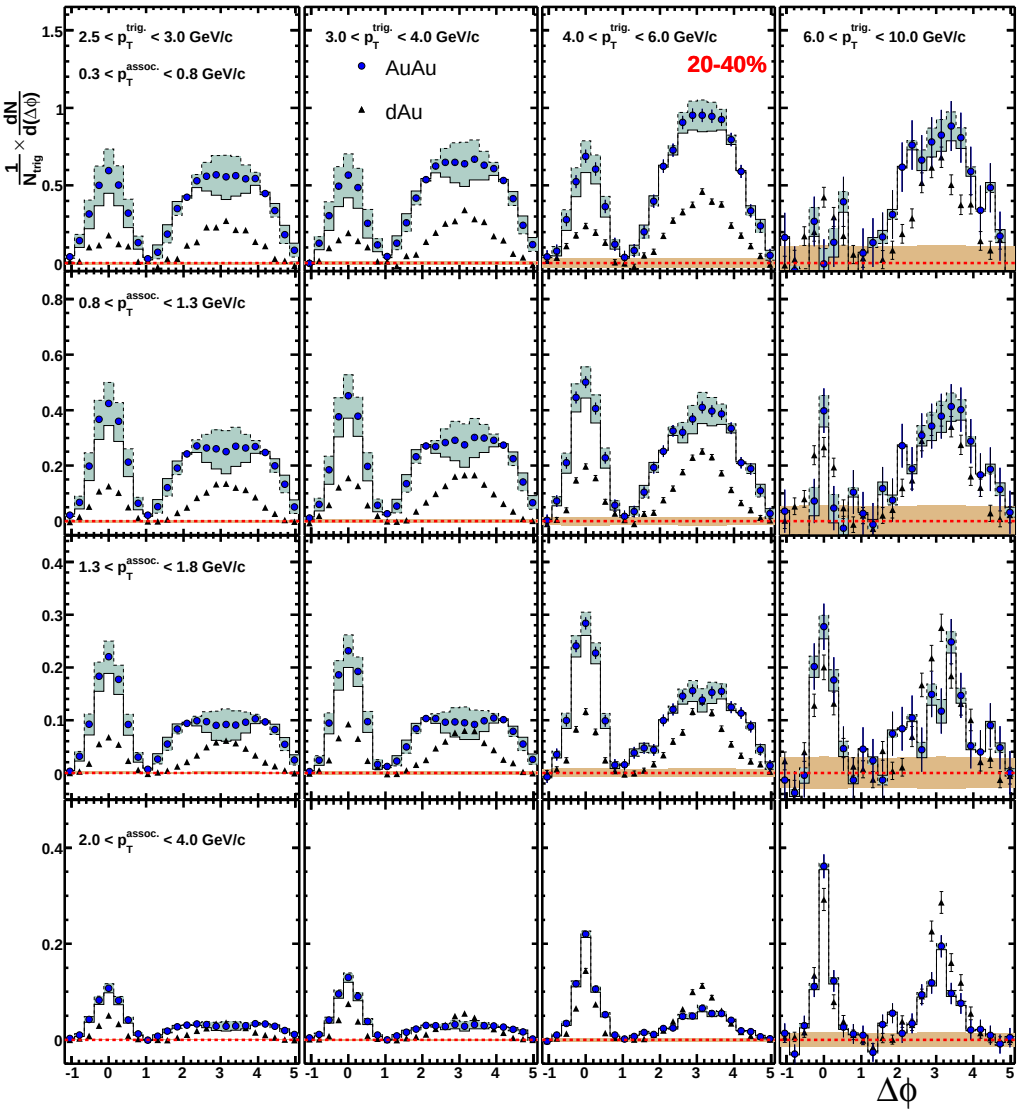

Figure 5.4 — Di-hadron distributions for 20-40% central collisions from the minimum bias Au+Au collisions. Results are shown for different $p_T^{assoc.}$ (from top to bottom), 0.3< $p_T^{assoc.}$ <0.8 GeV/c, 0.8< $p_T^{assoc.}$ <1.3 GeV/c, 1.3< $p_T^{assoc.}$ <1.8 GeV/c, and 2.0< $p_T^{assoc.}$ <4.0 GeV/c as well as for different $p_T^{trig.}$ (from left to right), 2.5< $p_T^{trig.}$ <3.0 GeV/c, 3.0< $p_T^{trig.}$ <4.0 GeV/c, 4.0< $p_T^{trig.}$ <6.0 GeV/c, and 6.0< $p_T^{trig.}$ <10.0 GeV/c. The bars show the statistical uncertainty in the data and the band around zero shows the statistical uncertainty in the background normalisation. The band surrounding the data show the systematic uncertainty from v_2.

follow this trend, but the statistics at low $p_T^{assoc.}$ are not large enough to be conclusive.The near-side yields increase for a fixed $p_T^{assoc.}$ increases with

increasing $p_T^{trig.}$. This is more pronounced for harder $p_T^{assoc.}$.

On the away-side there is a general trend towards an increase in the yield relative to the results shown in figure 5.3 but, in addition, there is a modification to the shape in some panels. The away-side shape becomes broader and flatter for increasing $p_T^{assoc.}$. This is more pronounced for the lowest $p_T^{trig.}$ and becomes less evident with increasing $p_T^{trig.}$. For the intermediate $p_T^{assoc.}$ range the away-side appears to become slightly depleted or suppressed at $\Delta\phi = \pi$, see for example 1.3< $p_T^{assoc.}$ <1.8 GeV/c for 2.5< $p_T^{trig.}$ <3.0 GeV/c. This feature disappears at higher or lower $p_T^{assoc.}$ and for higher $p_T^{trig.}$. The dipped structure is more localised in $p_T^{assoc.}$ for higher $p_T^{trig.}$, being evident over the widest $p_T^{assoc.}$ range for the lowest $p_T^{trig.}$, 2.5< $p_T^{trig.}$ <3.0 GeV/c. The dipped away-side shape is always within the systematic uncertainty from v_2.

$p_T^{assoc.}$ [GeV/c]	$\langle v_2^{assoc.} \rangle \cdot \langle v_2^{trigger} \rangle$ [%]	$P_{\lvert\Delta\eta\rvert<2.0}$
$2.5 < p_T^{trig.} < 3.0$ GeV/c		
0.3< $p_T^{assoc.}$ <0.8	$2.05^{+0.24}_{-0.23}$	42.7 ± 0.0057
0.8< $p_T^{assoc.}$ <1.3	$4.01^{+0.47}_{-0.44}$	11.8 ± 0.0028
1.3< $p_T^{assoc.}$ <1.8	$5.49^{+0.64}_{-0.61}$	3.38 ± 0.0015
2.0< $p_T^{assoc.}$ <4.0	$6.93^{+0.80}_{-0.77}$	0.832 ± 0.00071
$3.0 < p_T^{trig.} < 4.0$ GeV/c		
0.3< $p_T^{assoc.}$ <0.8	$2.07^{+0.24}_{-0.23}$	42.4 ± 0.0087
0.8< $p_T^{assoc.}$ <1.3	$4.05^{+0.48}_{-0.45}$	11.8 ± 0.0042
1.3< $p_T^{assoc.}$ <1.8	$5.54^{+0.65}_{-0.61}$	3.37 ± 0.0022
2.0< $p_T^{assoc.}$ <4.0	$6.99^{+0.81}_{-0.78}$	0.834 ± 0.0011
$4.0 < p_T^{trig.} < 6.0$ GeV/c		
0.3< $p_T^{assoc.}$ <0.8	$1.51^{+0.18}_{-0.17}$	42.0 ± 0.021
0.8< $p_T^{assoc.}$ <1.3	$2.95^{+0.35}_{-0.33}$	11.7 ± 0.010
1.3< $p_T^{assoc.}$ <1.8	$4.04^{+0.48}_{-0.45}$	3.33 ± 0.0054
2.0< $p_T^{assoc.}$ <4.0	$5.10^{+0.59}_{-0.57}$	0.826 ± 0.0027
$6.0 < p_T^{trig.} < 10.0$ GeV/c		
0.3< $p_T^{assoc.}$ <0.8	$1.51^{+0.18}_{-0.17}$	42.0 ± 0.079
0.8< $p_T^{assoc.}$ <1.3	$2.96^{+0.35}_{-0.33}$	11.7 ± 0.039
1.3< $p_T^{assoc.}$ <1.8	$4.04^{+0.48}_{-0.45}$	3.37 ± 0.021
2.0< $p_T^{assoc.}$ <4.0	$5.11^{+0.60}_{-0.57}$	0.835 ± 0.010

Table 5.3 — The v_2 values and the normalisation corresponding to the panels in figure 5.4.

The increase in yield with increasing system size persists from 40-60% to the 20-40% data. On the away-side we see the first hints of a novel struc-

ture but conclusive statements cannot be made based on this due to the systematic uncertainty from v_2.

5.2.4 0-12% Central Collisions

We analysed data with a central trigger as described in section 3.3.1. The triggered data allows us to probe the most central collisions, in which we see the most dramatic effects, more differentially as the data-set has significantly better statistics. The central triggered data are 0-12% central. The most central data from the minimum bias trigger (0-20%) can be found in appendix C.

The results for 0-12% central events are presented in figure 5.5 for the same selections of $p_T^{trig.}$ and $p_T^{assoc.}$ as in figures 5.1, 5.2, 5.3 and 5.4. The d+Au data (from figure 5.1) are included for reference. The vertical bars indicate the statistical error and the bands around the data points show the systematic uncertainty from v_2. The band around zero shows the uncertainty in the background normalisation.

The near-side yield increase is again visible and consistent with the 0-20% central results from the minimum bias data presented in figure C.1. The yield decreases with increasing $p_T^{assoc.}$. The yield, for fixed $p_T^{assoc.}$, also increases with $p_T^{trig.}$ for the case of 2.0< $p_T^{assoc.}$ <4.0 GeV/c. This also appears in the 1.3< $p_T^{assoc.}$ <1.8 GeV/c and becomes insignificant for lower $p_T^{assoc.}$.

On the away-side, we again have results consistent with those in figure C.1, much broader and flatter distributions with larger yield than in the more peripheral collisions. The significance of the broadening and flattening decreases with increasing $p_T^{trig.}$ for a fixed $p_T^{assoc.}$.

For 1.3< $p_T^{assoc.}$ <1.8 GeV/c and 2.5< $p_T^{trig.}$ <3.0 GeV/c we see an away-side shape which is dipped even when considering the systematic uncertainty from v_2. The significance of the dip decreases at higher and lower $p_T^{assoc.}$ as well as for increasing $p_T^{trig.}$.

The width of the away-side distribution is independent of $p_T^{trig.}$, but the significance of any dip in the shape does depend on $p_T^{trig.}$, consistent with an increase in yield which is restricted to small angles around $\Delta\phi = \pi$.

For 2.0< $p_T^{assoc.}$ <4.0 GeV/c and 6.0< $p_T^{trig.}$ <10.0 GeV/c we see the a hint

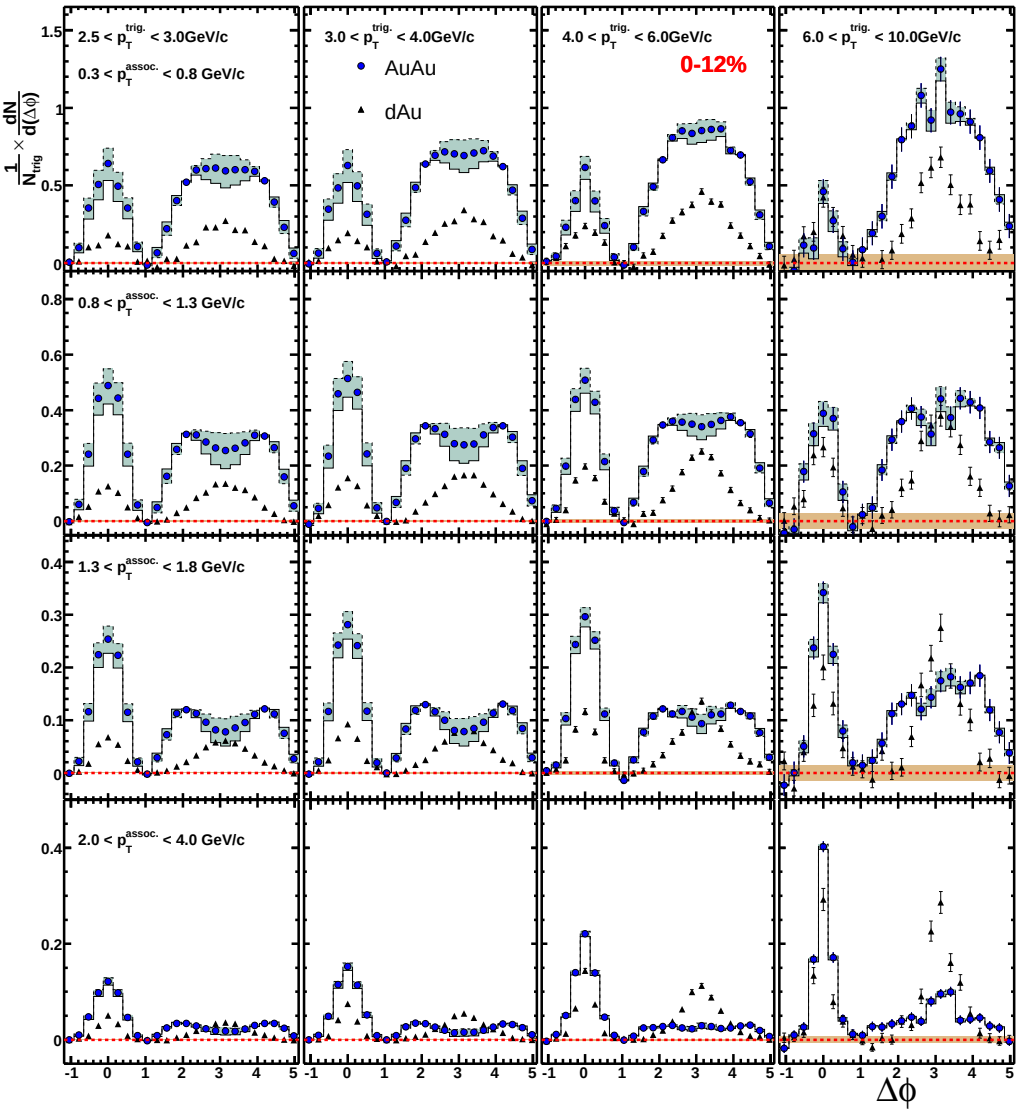

Figure 5.5 — Di-hadron distributions for 0-12% central collisions from central triggered Au+Au collisions. Results are shown for different $p_T^{assoc.}$ (from top to bottom), 0.3< $p_T^{assoc.}$ <0.8 GeV/c, 0.8< $p_T^{assoc.}$ <1.3 GeV/c, 1.3< $p_T^{assoc.}$ <1.8 GeV/c, and 2.0< $p_T^{assoc.}$ <4.0 GeV/c as well as for different $p_T^{trig.}$ (from left to right), 2.5< $p_T^{trig.}$ <4.0 GeV/c, 3.0< $p_T^{trig.}$ <4.0 GeV/c, 4.0< $p_T^{trig.}$ <6.0 GeV/c, and 6.0< $p_T^{trig.}$ <10.0 GeV/c. The bars show the statistical uncertainty in the data and the band around zero shows the statistical uncertainty in the background normalisation. The band surrounding the data show the systematic uncertainty from v_2.

of an away-side peak which is narrow, similar to the d+Au reference. The observation of a clear di-jet structure in Au+Au collisions has been demon-

$p_T^{assoc.}$ [GeV/c]	$\langle v_2^{assoc.} \rangle \cdot \langle v_2^{trigger} \rangle$ [%]	$P_{\lvert\Delta\eta\rvert<2.0}$
$2.5 < p_T^{trig.} < 3.0$ GeV/c		
$0.3 < p_T^{assoc.} < 0.8$	$0.332^{+0.079}_{-0.073}$	96.9 ± 0.0024
$0.8 < p_T^{assoc.} < 1.3$	$0.684^{+0.16}_{-0.15}$	28.6 ± 0.0012
$1.3 < p_T^{assoc.} < 1.8$	$0.969^{+0.23}_{-0.21}$	8.18 ± 0.00064
$2.0 < p_T^{assoc.} < 4.0$	$1.25^{+0.30}_{-0.28}$	1.88 ± 0.00030
$3.0 < p_T^{trig.} < 4.0$ GeV/c		
$0.3 < p_T^{assoc.} < 0.8$	$0.344^{+0.081}_{-0.074}$	96.6 ± 0.0038
$0.8 < p_T^{assoc.} < 1.3$	$0.707^{+0.17}_{-0.15}$	28.5 ± 0.0019
$1.3 < p_T^{assoc.} < 1.8$	$1.00^{+0.24}_{-0.22}$	8.16 ± 0.0010
$2.0 < p_T^{assoc.} < 4.0$	$1.30^{+0.31}_{-0.28}$	1.88 ± 0.00048
$4.0 < p_T^{trig.} < 6.0$ GeV/c		
$0.3 < p_T^{assoc.} < 0.8$	$0.264^{+0.057}_{-0.052}$	96.2 ± 0.0100
$0.8 < p_T^{assoc.} < 1.3$	$0.543^{+0.12}_{-0.11}$	28.3 ± 0.0050
$1.3 < p_T^{assoc.} < 1.8$	$0.770^{+0.17}_{-0.15}$	8.13 ± 0.0026
$2.0 < p_T^{assoc.} < 4.0$	$0.996^{+0.21}_{-0.20}$	1.88 ± 0.0012
$6.0 < p_T^{trig.} < 10.0$ GeV/c		
$0.3 < p_T^{assoc.} < 0.8$	$0.268^{+0.057}_{-0.053}$	95.9 ± 0.039
$0.8 < p_T^{assoc.} < 1.3$	$0.550^{+0.12}_{-0.11}$	28.3 ± 0.020
$1.3 < p_T^{assoc.} < 1.8$	$0.780^{+0.17}_{-0.15}$	8.10 ± 0.010
$2.0 < p_T^{assoc.} < 4.0$	$1.01^{+0.22}_{-0.20}$	1.87 ± 0.0049

Table 5.4 — The v_2 values and the normalisation corresponding to the panels in figure 5.5.

strated previously in [117] but at much higher $p_T^{assoc.}$ and $p_T^{trig.}$ than shown here.

In summary we have three features to understand, the increase in the yield on both the near- and away-side and the evolution of the away-side shape.

5.2.5 Near-side Yield Increase

It has been shown that at relatively high p_T there is a significant contribution from correlated yield at $\Delta\eta > 0.7$ (as discussed in section 2.5.1). We investigate this as the cause of the increased yield at small $\Delta\phi$.

In figure 5.6 we present the per-trigger di-hadron distributions for $1.0 < p_T^{assoc.} < 2.5$ GeV/c and $2.5 < p_T^{trig.} < 4.0$ GeV/c for the full acceptance of the TPC (blue circles) and for a case where the associated particle is restricted to a range in pseudo-rapidity of $0.72 < |\Delta\eta| < 1.44$ (orange circles) relative to the trigger particle. Full acceptance d+Au results (triangles) are

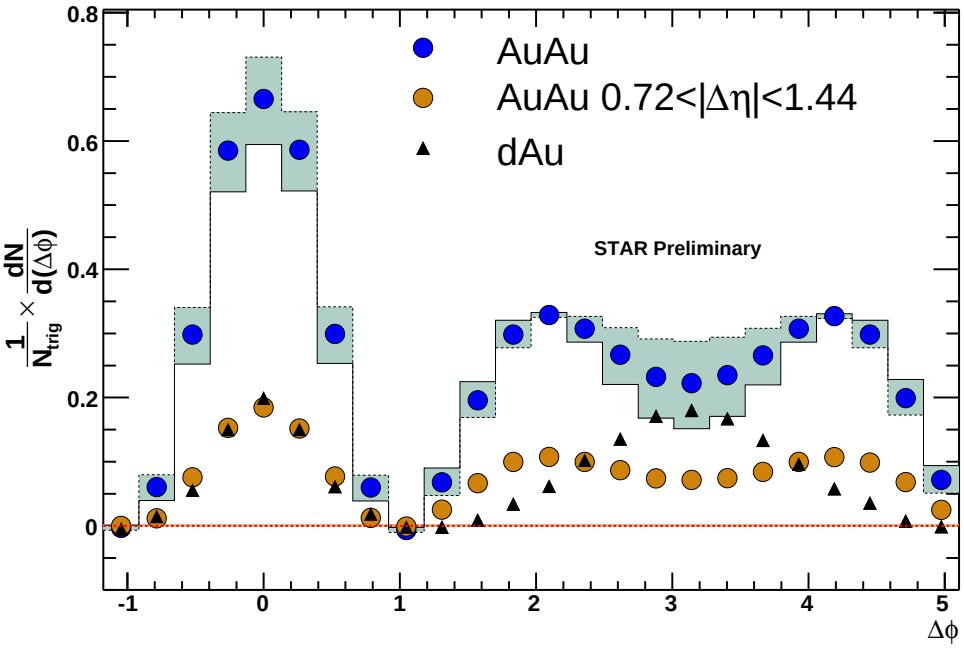

Figure 5.6 — Di-hadron distributions for 1.0< $p_T^{assoc.}$ <2.5 GeV/c and 2.5< $p_T^{trig.}$ <4.0 GeV/c, for the full $\Delta\eta$ acceptance (blue circles) and for $0.72 < |\Delta\eta| < 1.44$ (orange circles) relative to the trigger particle. d+Au results (black triangles) are shown for reference. The bands around the data points show the systematic uncertainty from v_2 determination.

included for reference. On the near-side there is a significant enhancement in yield relative to the d+Au reference. A large fraction of this yield comes from a contribution at $\Delta\eta > 0.7$. See [89] for a more detailed study.

On the away-side there is a significant broadening of the shape and increase in the yield relative to d+Au. The away-side shape does not depend on $\Delta\eta$. The yield at large $\Delta\eta$ is due to the pair-acceptance effect, and after correcting for this effect the yield is independent of $\Delta\eta$ as well. This is expected because the away-side parton is not correlated in pseudo-rapidity with the near-side parton due to the fact that the incoming partons have a momentum distribution within the incoming nucleons. This is signficant in pseudo-rapidity because of the large boost each nucleon has in the beam direction and less significant in the transverse direction as the internal momenta are small.

5.2.6 $p_T^{trig.}$-Dependence of Away-side Shape

In figure 5.5 we observe an approximately constant width on the away-side at intermediate p_T, despite increasing $p_T^{trig.}$. To further illustrate this idea we plot 1.3< $p_T^{assoc.}$ <1.8 GeV/c for 3 different choices of $p_T^{trig.}$, 3.0< $p_T^{trig.}$ <4.0 GeV/c, 4.0< $p_T^{trig.}$ <6.0 GeV/c and 6.0< $p_T^{trig.}$ <10.0 GeV/c in the three left panels, in the fourth panel (right-most) we superimpose the data for 3.0< $p_T^{trig.}$ <4.0 GeV/c and 6.0< $p_T^{trig.}$ <10.0 GeV/c. The d+Au results are included for reference.

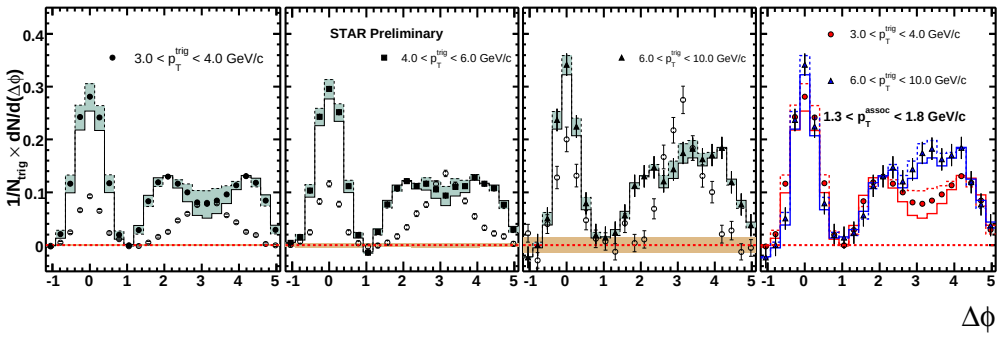

Figure 5.7 — Di-hadron distributions, from 0-12% central Au+Au collisions, for 1.3< $p_T^{assoc.}$ <1.8 GeV/c for 3 different choices of $p_T^{trig.}$, 3.0< $p_T^{trig.}$ <4.0 GeV/c (solid circles), 4.0< $p_T^{trig.}$ <6.0 GeV/c (solid squares) and 6.0< $p_T^{trig.}$ <10.0 GeV/c (solid triangles). d+Au results (open circles) are shown in the panels for reference. The bands around the data points show the systematic uncertainty from v_2 determination while the band around zero shows the systematic uncertainty in the background pedestal determination. The right panel shows the superposition of the Au+Au results for 3.0< $p_T^{trig.}$ <4.0 GeV/c and 6.0< $p_T^{trig.}$ <10.0 GeV/c.

With increasing $p_T^{trig.}$ the away-side shape evolves to a flatter structure. The width of the away-side structure is approximately independent of $p_T^{trig.}$, as can be seen from the right-most panel. This could mean that there are two contributions to the signal: a broad structure with little or no dependence on $p_T^{trig.}$, most likely from the medium response to the jet (as suggested in [140]), and a narrower jet-contribution that increases with $p_T^{trig.}$. This is qualitatively supported by considering the d+Au results in the various panels. The significance of the away-side peak in d+Au increases with $p_T^{trig.}$ implying that any residual jet contribution at $\Delta\phi = \pi$ should be more significant with increasing $p_T^{trig.}$.

5.3 Multi-Component Decomposition of Away-side Shape

In the previous section we have shown that the away-side yield may be a superposition of bulk response with a central contribution. To investigate the feasibility of this picture we test to see how well this phenomenological model for the away-side shape fits the 0-12% central triggered Au+Au data. As the shapes evolve with both $p_T^{trig.}$ and $p_T^{assoc.}$ we expect the significance of the various components to vary with these parameters, thus we conduct these studies differentially with respect to these two parameters to the extent allowed by statistics.

The various fit functions we use are:

Symmetric Gaussians: two Gaussian distributions symmetric about $\Delta\phi = \pi$ and of equal magnitude and width:

$$\frac{1}{N_{trig}} \cdot \frac{dN}{d(\Delta\phi)} = A(e^{-\frac{(\Delta\phi-\pi+m)^2}{\sigma^2}} + e^{-\frac{(\Delta\phi-\pi-m)^2}{\sigma^2}}) \tag{5.1}$$

Gaussians + Cosine: two Gaussian distributions symmetric about $\Delta\phi = \pi$ and of equal magnitude and width superimposed on a cosine distribution centred at $\Delta\phi = \pi$:

$$\frac{1}{N_{trig}} \cdot \frac{dN}{d(\Delta\phi)} = A(e^{-\frac{(\Delta\phi-\pi+m)^2}{\sigma^2}} + e^{-\frac{(\Delta\phi-\pi-m)^2}{\sigma^2}}) + B\cos(\Delta\phi - \pi) \tag{5.2}$$

Gaussians + Gaussian: two Gaussian distributions symmetric about $\Delta\phi = \pi$ and of equal magnitude and width superimposed on a Gaussian distribution centred at $\Delta\phi = \pi$:

$$\frac{1}{N_{trig}} \cdot \frac{dN}{d(\Delta\phi)} = A(e^{-\frac{(\Delta\phi-\pi+m)^2}{\sigma^2}} + e^{-\frac{(\Delta\phi-\pi-m)^2}{\sigma^2}}) + Be^{-\frac{(\Delta\phi-\pi)^2}{\sigma'^2}} \tag{5.3}$$

Figure 5.8 demonstrates the different fit distributions that we use, for arbitrary parameters. The left-most panel shows the Symmetric Gaussians which represent the peaks away from $\Delta\phi = \pi$ and represent the bulk contribution to the away-side, i.e. the signal in this study. The central panel includes a cosine distribution which is included as a simple momentum

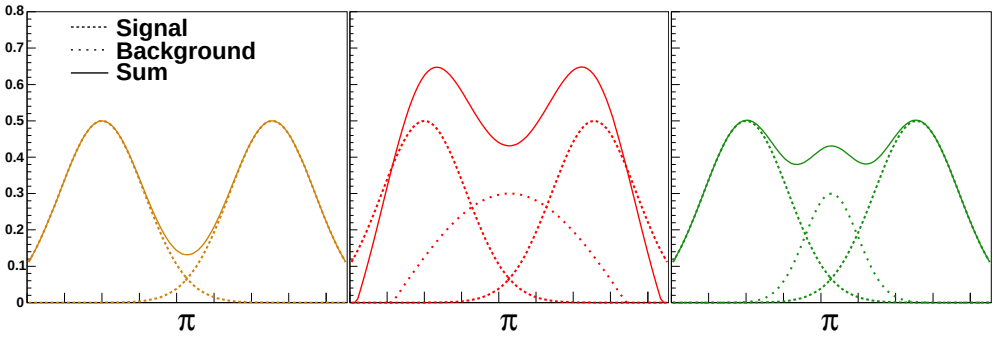

Figure 5.8 — Examples of the different fitting assumptions for the away-side shape: two equal Gaussians symmetric about $\Delta\phi = \pi$ (orange, left-most panel), two equal Gaussians symmetric about $\Delta\phi = \pi$ with a central $\cos\Delta\phi$ contribution (red, middle panel), and two equal Gaussians symmetric about $\Delta\phi = \pi$ with a central Gaussian contribution (green, right-most panel). The symmetric Gaussians are the dashed lines in each panel, the central contributions are the dotted lines and the solid line is the sum of all contributions.

conservation term, based on the idea that the bulk may just be recoiling. The right-most panel has a central Gaussian distribution added which represents the possibility that a parton, of some reduced energy or reduced probability, escapes at $\Delta\phi = \pi$ and fragments giving a jet-like peak.

In figure 5.9 we present results of the distance of the mean of the symmetric Gaussians away from $\Delta\phi = \pi$ as a function of $p_T^{assoc.}$ for two $p_T^{trig.}$, 3.0< $p_T^{trig.}$ <4.0 GeV/c and 4.0< $p_T^{trig.}$ <6.0 GeV/c. The vertical bars denote the statistical uncertainty in the fit results and the dotted bands denote the systematic uncertainty from v_2.

For the case where no central contribution is explicitly included the separation between the peaks increases with increasing $p_T^{trig.}$ and remain smaller than the other two cases. Both cases where a central contribution is included are approximately constant with $p_T^{assoc.}$, deviations at the lowest $p_T^{assoc.}$ are seen where the away-side shape is large and broad with no significant dip.

The location of the symmetric Gaussians may be constant but the fraction of the away-side yield that they contribute may vary significantly. In figure 5.10 we display the fraction of the total away-side yield that is attributed to the symmetric Gaussian components of the away-side. Results are shown as a function of $p_T^{assoc.}$ for 3.0< $p_T^{trig.}$ <4.0 GeV/c (left panel) and

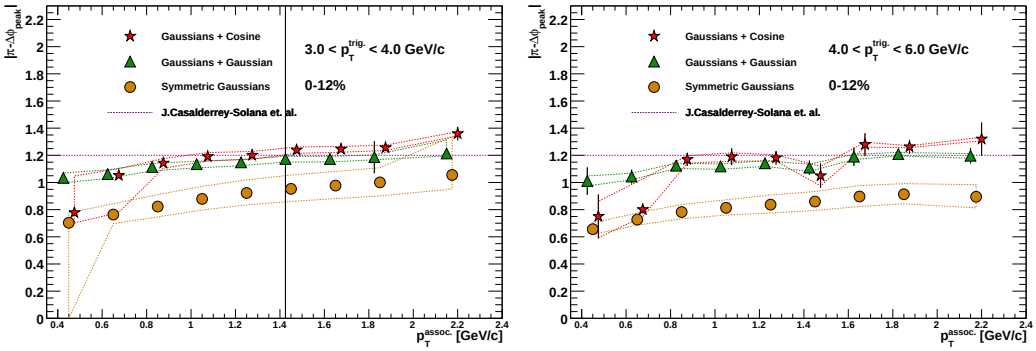

Figure 5.9 — The angle of the mean of the symmetric Gaussians away from $\Delta\phi = \pi$ for the different fit assumptions as a function of $p_T^{assoc.}$for 3.0< $p_T^{trig.}$ <4.0 GeV/c (left) and 4.0< $p_T^{trig.}$ <6.0 GeV/c (right) for 0-12% central Au+Au data. The fit assumptions are symmetric Gaussians (orange circles), central Gaussian contribution (green triangles), and central cosine contribution (red stars).The purple line is inspired by [91]. The vertical lines indicate the error from the fit and the dashed bands indicate the systematic uncertainty in v_2.

4.0< $p_T^{trig.}$ <6.0 GeV/c (right panel) from 0-12% central Au+Au collisions. The results for Symmetric Gaussians, Gaussians + Cosine, and Gaussians + Gaussian are shown as the black circles, red stars, and green triangles respectively.

For the case where no central contribution is included (black circles) the distributions account for all the yield as can be seen by the constant results at 1.

For the two cases where a central distribution is included we see different behaviour at low $p_T^{assoc.}$. For the case where the central contribution is a cosine (red stars) the symmetric Gaussians account for a very small fraction of the yield at low $p_T^{assoc.}$. This is to be expected at low $p_T^{assoc.}$ because the distributions to be fitted are large and very broad with no central dip or even significant flattening. The broadly peaked away-side is then reasonably well represented by a cosine distribution alone. As the yield decreases with increasing $p_T^{assoc.}$, and even becomes dipped, it cannot be as well represented by just the central distribution as is supported by the increasing fraction of the away-side yield which is attributed to the symmetric Gaussians.

The case where the central distribution is a Gaussian (green triangles) ex-